



OSI SAF Visiting Scientist Activity Report

OSI_VS19_06

Final Report

**Sea ice concentration noise reduction using
brightness temperature correction**

Prepared by Marko Mäkynen

Revised by Rasmus T. Tonboe

May 2020



**ILMATIETEEN LAITOS
METEOROLOGISKA INSTITUTET
FINNISH METEOROLOGICAL INSTITUTE**

Table of Contents

1	Proposal Summary.....	4
1.1	Document History.....	4
1.2	Acronyms.....	5
2	Introduction.....	6
3	Datasets	7
3.1	AMSR2 TB data	7
3.2	ERA-Interim data	8
3.3	MODIS ice thickness charts	8
3.4	Combined MODIS – AMSR2 thin ice data.....	9
4	OSI SAF SIC Simulation.....	10
4.1	OSI-408 SIC Simulation	10
4.2	OSI-450 SIC Simulation	13
4.3	Atmospheric Correction of TB Data	16
4.4	Improved SIC Derivation.....	18
5	Thin Ice Detection with the AMSR2 Data	19
5.1	AMSR2 thin ice detection with PR36 and GR8936H	20
5.2	AMSR2 thin ice detection in the 10.65 to 36.5 GHz frequency range.....	22
6	New Sea Ice Emissivities and Effective Temperatures for the TB Atmospheric Correction ...	24
6.1	Sea ice effective temperature from air temperature.....	25
6.2	Sea ice effective temperature from radiometer data	26
6.3	FYI and MYI emissivities with T_{eff} from T_a	27
6.4	FYI and MYI emissivities with T_{eff} from the AMSR2 data	31
7	Effect of New Sea Ice Emissivities and Effective Temperatures in the TB Atmospheric Correction	34
7.1	FYI and MYI emissivities with T_{eff} from T_a	36
7.2	FYI and MYI emissivities with T_{eff} from the AMSR2 data	37
8	Dynamic Tuning of SIC Algorithms	39
8.1	SIC algorithms at 25 km grid.....	40
8.2	SIC algorithms at 50 km grid.....	45
8.3	Further tuning experiments	45
9	Comparison between Different SIC Datasets	52
9.1	Comparison between pixel SIC values.....	52
9.2	Comparison between mean SICs as a function of time.....	55

10	Conclusions and Recommendations.....	59
11	References	61
A	Appendix – Matlab Programs	64

1 Proposal Summary

VSA Title	Sea ice concentration noise reduction using brightness temperature correction		
VSA Id	OSI_VS19_06	Objective category	Improving existing products
VSA host institute	Danish Meteorological Institute	Related OSI SAF product(s)	OSI-401, OSI-403-c, OSI-408, OSI-430, OSI-450
VSA supervisor	Danish Meteorological Institute	Related OSI SAF WP(s)	WP22110, WP22210
Expected start date	4 Nov 2019	Related OSI SAF review(s)	NA
Expected end date	29 Nov 2019	VSA costs	7000 €
VS candidate	Marko Mäkynen	VS/AS	Visiting Scientist
VS home institute administrative contact	Marko Mäkynen Finnish Meteorological Institute		

1.1 Document History

Version	Date	Comments & Status	Authors
V1.0	15/05/2020	First version	Marko Mäkynen
V1.1	20/05/2020	minor edit in Section 10	Marko Mäkynen

1.2 Acronyms

Acronym	Definition
AMSR2	Advanced Microwave Scanning Radiometer 2
AVHRR	Advanced Very High Resolution Radiometer
BFM	Bootstrap frequency mode SIC algorithm
BKS	Barents and Kara Seas
BRI	Bristol SIC algorithm
ECMWF	European Centre for Medium range Weather Forecast
EUMETSAT	European Organisation for the Exploitation of Meteorological Satellites
FYI	first-year ice
GR	gradient ratio
H	horizontal polarization
JAXA	Japan Aerospace Exploration Agency
LDA	linear discriminant analysis
MIZ	marginal ice zone
MODIS	Moderate Resolution Imaging Spectroradiometer
MYI	multiyear ice
NASA	National Aeronautics and Space Administration
NT	NASA Team SIC algorithm
OSI-401b	SSMIS Sea Ice Concentration Maps on 10 km Polar Stereographic Grid
OSI-408	AMSR-2 Sea Ice Concentration Maps on 10 km Polar Stereographic Grid
OSI-450	Global Sea Ice Concentration Climate Data Record v2
OSI SAF	Ocean and Sea Ice SAF
PCA	principal component analysis
PR	polarization ratio
PS	polar stereographic
RTM	radiative transfer model
SAF	Satellite Application Facility
SIC	sea ice concentration
SIT	sea ice thickness
SSM/I	Special Sensor Microwave Imager
SSMIS	Special Sensor Microwave Imager / Sounder
STD	stand deviation
V	vertical polarization

2 Introduction

The OSI SAF SIC products, .e.g. OSI-450 (Global Sea Ice Concentration Climate Data Record v2) (Lavergne et al., 2019b) and OSI-408 (AMSR-2 Sea Ice Concentration Maps on 10 km Polar Stereographic Grid) (Tian et al., 2015), have SIC noise, SIC under and over estimations, over high SIC areas, like multiyear ice (MYI) in the north of the Greenland (Kern et al., 2019). These are currently reduced in the OSI-450 product with an empirical ‘curved’ 100% ice line in the SIC algorithm (not applied in the OSI-408 product). This statistical correction is correcting the hemispherical SIC bias but it does not reduce the near 100% SIC noise, i.e. the spread around the ice line. Therefore, to reduce the noise at near 100% SIC we are looking for a correction based on physical relationships between sea ice properties and measured brightness temperatures (T_B), enhanced atmospheric correction of T_B data, or enhanced derivation of the 100% ice line that would work on local to regional scale. The ‘curved’ ice line and the physical corrections are not excluding one another, and can be applied together reducing both bias and local noise. The physical corrections could even help in “straightening” the ice line and reducing regional bias. The SIC noise could also come partly from fixed sea ice emissivities used in the T_B atmospheric correction (Andersen et al., 2006; Lavergne et al., 2019b), and simple estimation of sea ice effective temperature (T_{eff}) (no ice type dependence) based on the air temperature (T_a). In an ideal case the SIC noise is reduced to the noise level of a radiometer sensor.

We investigate here first possible improvements to the SIC retrieval by using dynamic sea ice emissivities (e_{si}) and T_{eff} ’s, and their winter season reference values in the T_B atmospheric correction. T_{eff} is estimated with (a) frequency and ice type dependent (FYI and MYI) T_{eff} vs. T_a relationships by Mathew et al. (2009), or (b) directly from the radiometer data (no ice type dependence) (Kilic et al., 2019). The T_{eff} estimation by Kilic et al. (2019) uses radiometer V-polarization channels from 6.9 to 36.5 GHz, and results in T_{eff} data at the same spatial resolution as SIC is estimated. However, this method is valid only for sea ice with 100% SIC. Nevertheless, it is tested over the Arctic pack ice, and further, a possible correlation between Kilic’s T_{eff} and T_a is investigated for the T_{eff} estimation over sea ice with SIC<100%. We develop a method for thin ice detection using radiometer data following previous work (Mäkynen and Similä, 2019) in order to exclude thin ice signatures in determination of daily sea ice tie points in the OSI SAF SIC algorithms. SIC data accuracy with and without the curved ice line correction in the OSI-450 algorithm is compared. Both the OSI-408 and OSI-450 SIC products are based on the V- and H-polarization 36 GHz and V-pol 18 GHz T_B ’s, and we investigate here if other three channel combinations of 18 and 36 GHz T_B ’s and sums and differences of T_B ’s can yield better quality (less noise and smaller bias) SIC data.

The dynamic e_{si} ’s can be monthly mean FYI and MYI emissivities over the Arctic derived by Mathew et al. (2009), or they can be empirically estimated from the original, uncorrected T_B data. The method for the empirical e_{si} estimation was developed here. It could be also possible through MEMLS simulations data to find relationships between e_{si} ’s at different radiometer channels and some polarization and gradient ratios (PR and GR), as was done by Tonboe et al. (2013) for near 50 GHz emissivity.

For these different studies on the SIC improvements AMSR2 L1R T_B data for one winter season, from Oct 2017 to May 2018, are used. The L1R T_B data were projected to 25 and 50 km grids over the Arctic. In addition, the ERA-Interim data is used for the T_B atmospheric correction, and a combined MODIS-AMSR2 thin ice dataset by Mäkynen and Similä (2019) for investigating thin ice rejection in the daily tuning of the SIC algorithms.

Sea ice concentrations are calculated with OSI SAF SIC data simulators (default and improved) programmed in Matlab. These simulators are somewhat simplified versions of the OSI SAF SIC Level 2 processing chains; e.g. land spill-over of T_B data is not conducted. SIC can be derived following the OSI-408 AMSR2 SIC algorithm as a combination of the Bristol SIC algorithm (Smith, 1996; Smith and Barrett, 1993) and Bootstrap frequency mode (BMF) (Comiso, 1986a), or the OSI-450 SIC algorithm where optimal planes in the 3-D T_B space are determined daily for the SIC estimation in low and high SIC conditions (Lavergne et al., 2019a, 2019b). In the OSI-408 AMSR2 product SIC comes from the Bristol algorithm only when the BMF SIC (Comiso, 1986b) is larger than 40% (Tian et al., 2015). The OSI-450 is a climate data record SIC product and the OSI-408 is an operational daily SIC product. The default SIC simulator which follows the OSI-450 or OSI-408 algorithm includes following processing steps: collection 100% SIC and open water samples for the daily tie points (open water point and the 100% SIC ice line), atmospheric correction of the T_B swath data using fixed e_{si} 's and T_{eff} 's, and determination of the tie points and/or optimal SIC algorithms (OSI-450 only). It was decided to use only the OSI-450 SIC algorithm in here as it is more advanced than the OSI-408 one. Nevertheless, also the OSI-408 algorithm and simulator are presented in this report. The improved SIC simulator developed in here is somewhat different than the OSI-450 one (details in Section 4.4) and it includes the enhancements described above.

It is assumed that SIC estimates with these Matlab OSI SAF SIC product simulators give accurate enough information on temporal and spatial SIC anomalies/changes over the Arctic pack ice, and allow determination of possible SIC data improvements due to new definitions of the emissivities, T_{eff} , and other parameters.

3 Datasets

3.1 AMSR2 T_B data

AMSR2 level L1R T_B data (Maeda et al., 2016) were downloaded from a ftp-service of Japan Aerospace Exploration Agency (JAXA). In this study, we use (a) 10.65, 18.7, 36.5 and 89 GHz T_B data resampled to the footprint size (i.e. field of view) of the 10.65 GHz T_B data (24 x 42 km), and (b) all channels resampled to the footprint of the 6.9 GHz T_B data (35 by 62 km). The datasets cover one Arctic winter season, from Oct 2017 to May 2018. The dataset (a) was gridded to a polar stereographic (PS) coordinate system with the reference longitude of -45 E, the true scale latitude of 70 N and pixel size of 25 km. The dataset (b) were gridded to the same PS grid, but with 50 km pixel size. These two grids are positioned so that a 50 km pixel covers a 2 by 2 block of 25 km pixels. The resampling of the L1R data to the PS grids were conducted with the Matlab griddatool using linear interpolation.

For investigating thin ice detection with combined MODIS and AMSR2 data (MODIS thin ice charts as training data, see Section 3.3) AMSR2 L1R data were also retrieved for the Barents and Kara Seas (BKS) for Jan – Apr 2014 and Oct 2014 – Apr 2015. In this study only 10.65, 18.7, 36.5 and 89 GHz T_B data resampled to the footprint size of the 10.65 GHz T_B data are used. This T_B data were gridded a PS coordinate system with mid-longitude of 55E and true-scale latitude of 70N and pixel size of 20 km. Various polarization (PR) and gradient (GR) ratios are calculated from the gridded T_B data as:

$$PR(f) = \frac{T_{BV}(f) - T_{BH}(f)}{T_{BV}(f) + T_{BH}(f)} \quad (1)$$

$$GR(f_1, f_2, p) = \frac{T_B(p, f_1) - T_B(p, f_2)}{T_B(p, f_1) + T_B(p, f_2)} \quad (2)$$

where f is frequency, and p is either V- or H-polarization.

Landmask for the AMSR2 25 km grid was derived from the OSI SAF 408 product (25 km EASE2 grid), see Figure 1. The OSI SAF landmask was resampled to the PS grid with the nearest neighbour interpolation and then ocean areas smaller than three pixels were removed. The landmask for the 50 km grid was derived by marking a 2x2 block in the 25 km mask as land if even one pixel was land.

3.2 ERA-Interim data

Atmospheric forcing data for the atmospheric correction of the AMSR2 T_B data were extracted from the ECMWF's ERA-Interim reanalysis data (Dee et al., 2011). The data over the Arctic has 3-hourly time step and 0.25x0.25 deg spatial grid, and following parameters: 2-m air temperature, 10-m wind speed, total column water vapour, total column liquid water, and skin temperature. The ERA-Interim data were sampled to the AMSR2 PS grids with cubic interpolation, and further linearly interpolated to the acquisition times of the AMSR2 swath T_B data sets.

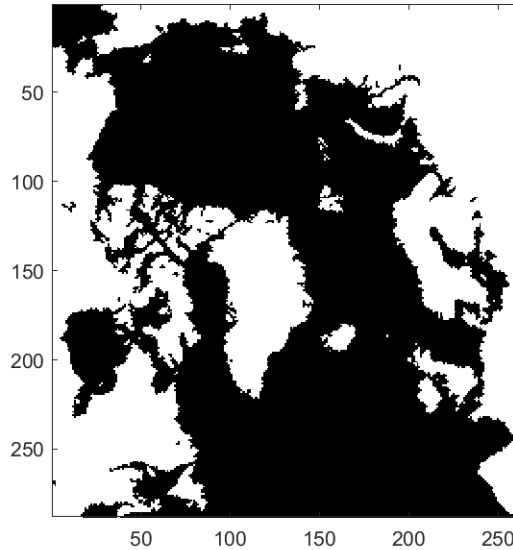


Figure 1. Arctic landmask for the AMSR2 data processed to a 25 km PS grid.

3.3 MODIS ice thickness charts

MODIS ice thickness (h_{iM}) charts based on Terra MODIS sea ice surface temperature (T_{ssi}) swath data and ERA-Interim atmospheric forcing data were processed over the Barents and Kara Seas (BKS) (see Figure 2) for Jan – Apr 2014 and Oct 2014 – Apr 2015. The processing of the h_{iM} chart is described in detail in (Mäkynen et al., 2013) and summarized in (Mäkynen and Similä, 2019). The total number of the charts is 173.

The charts have pixel size of 1 km, cover an area of 1850 (northing) by 2200 km (easting) and are in a PS coordinate system with mid-longitude of 55E and true-scale latitude of 70N. The charts have a cloud mask with 10 km pixel size which is based on automatic and manual methods (Mäkynen et al., 2013).

Only night-time MODIS T_{ssi} data were employed in the calculation of the h_{iM} swaths charts, and thus, the uncertainties related to the effects of solar shortwave radiation and surface albedo were excluded. In the h_{iM} retrieval following piecewise linear relationship was used between snow (h_s) and ice (h_i) thickness (Mäkynen and Similä, 2019):

$$\begin{aligned}
h_s &= 0 \text{ for } h_i \leq 5 \text{ cm} \\
h_s &= 0.05 \cdot h_i \text{ for } 5 \text{ cm} < h_i \leq 10 \text{ cm} \\
h_s &= 0.13 \cdot h_i - 0.8 \text{ cm for } 10 \text{ cm} < h_i \leq 20 \text{ cm.} \\
h_s &= 0.09 \cdot h_i \text{ for } h_i > 20 \text{ cm}
\end{aligned} \tag{3}$$

The swath h_{iM} chart shows ice thickness in the 0-1 m range with 1 cm resolution, see Figure 2. Retrieved h_{iM} values over 1 m are flagged as 1 m. For thick ice, the h_{iM} retrieval often fails ($h_{iM} < 0$). These pixels have a flag value of -0.1 m. Under warm conditions ($T_a > -20$ °C), the h_{iM} retrieval may also fail for thin ice (< 0.5 m). As the uncertainty of the retrieved h_{iM} increases with increasing T_a , the h_{iM} retrieval was not conducted when $T_a > -5$ °C. The typical maximum reliable h_{iM} (max 50% uncertainty) is 0.35-0.50 m (Mäkynen et al., 2013). The accuracy is the best for the 0.15-0.30 m thickness range, around 38% uncertainty.

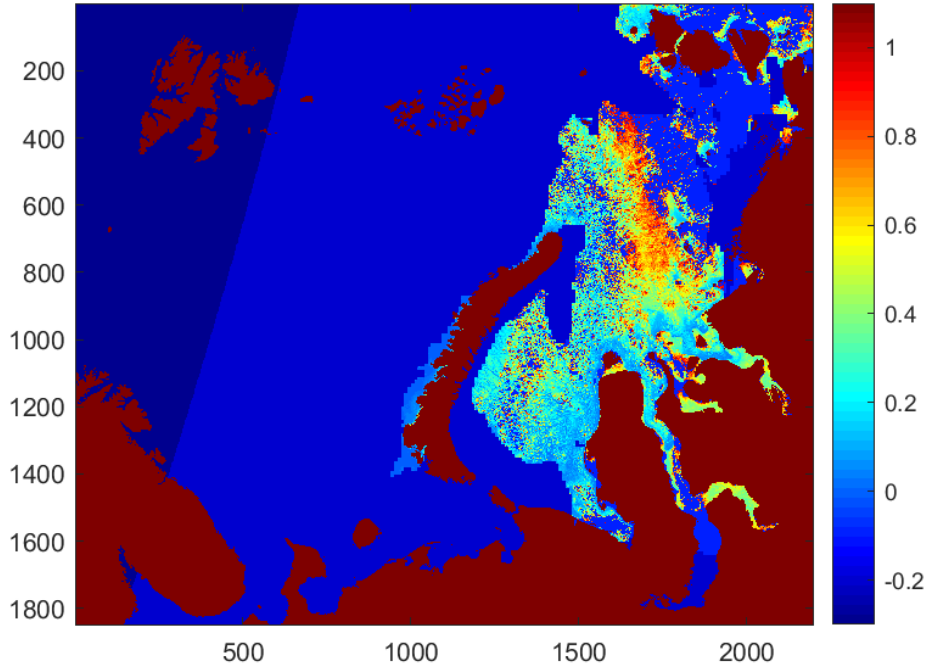


Figure 2. Ice thickness chart derived from the MODIS ice surface temperature data acquired on 26 Nov 2014, 07:35 UTC. Dark blue is either cloud mask (thickness -0.2 m), no data mask (-0.3 m) or scan angle mask (-0.2 m) and light blue (-0.1 m) indicates areas where ice thickness retrieval was unsuccessful or resulted thickness values over 1 m.

3.4 Combined MODIS – AMSR2 thin ice data

For investigating thin ice detection with the AMSR2 T_B data (10.65, 18.7, 36.5 and 89 GHz) a dataset of co-incident MODIS h_{iM} , various AMSR2 PR 's and GR 's, and T_a at the 20 km BKS grid was constructed. This dataset was prepared exactly the same way as in (Mäkynen and Similä, 2019), but the pixel size is now 20 km, see details in Section II-F of (Mäkynen and Similä, 2019). In general, combined T_B and pixel-wise mean h_{iM} (\bar{h}_{iM}) data were only selected over sea ice areas having rather uniform ice thickness and $SIC \geq 70\%$, which reduces signature mixing from various ice types and open water. The SIC data here was from the AMSR2 L2 SIC product based on the

Bootstrap algorithm (Comiso and Cho, 2013). The OSI SAF AMSR2 atmospheric correction with winter time FYI e_{si} 's and T_{eff} 's by Mathew et al. (2009) was applied to the T_B data.

The total number samples in the combined dataset is 27808. For 94% of the data, SIC is over 90%. For thin ice ($\bar{h}_{iM} \leq 0.2$ m), there is 6622 samples, and for thick ice classes of $0.2 < \bar{h}_{iM} < 1.0$ m and $\bar{h}_{iM} \geq 1$ m, there are 9759 and 11427 samples, respectively. Roughly 90% of the thick ice $0.2 < \bar{h}_{iM} < 1.0$ m class samples are for $T_a < -20$ °C. For thin ice this fraction is 58%.

4 OSI SAF SIC Simulation

For studying possible improvements in the OSI SAF SIC retrieval over the Arctic pack ice (SIC close to 100%) three different SIC calculation programs (or simulators) have been programmed in Matlab. The first two are called the default SIC programs and they calculate SIC following the OSI SAF 450 and 408 Level 2 SIC algorithms/processing chains, but have some simplifications, e.g. there is no land-spill over correction. The third one is the improved SIC processing chain based on the OSI-450 algorithm. It was decided to use only the OSI-450 SIC algorithm/simulator in various SIC data accuracy and quality studies as it is more advanced than the OSI-408 one.

The OSI-408 is an operational SIC product based on the AMSR2 T_B data where SIC is a combination of the Bristol algorithm (input is T_{B18V} , T_{B36V} and T_{B36H} data) (Smith, 1996; Smith and Barrett, 1993) and the Bootstrap frequency mode (BMF) (Comiso, 1986a) (input is T_{B18V} and T_{B36V} data) SICs (Tian et al., 2015). The OSI-408 SIC comes from the Bristol algorithm only when the BMF SIC is larger than 40% (Tian et al., 2015).

In the OSI-450 algorithm two optimal planes in the 3-D T_B space are determined for the SIC estimation in low and high SIC conditions (named B_{OW} for best open water, B_{CI} for best closed ice) (Laverne et al., 2019a, 2019b). When $70 \leq B_{OW} \leq 90\%$ a linear combination of B_{OW} and B_{CI} is used for the final SIC.

In the following the OSI-408 and OSI-450 SIC algorithms are described in more detail (but not all details are given, they can be found in various OSI SAF publications). The procedure of the atmospheric correction of the T_B data which is common for the both SIC algorithms is presented in Section 4.3. Finally, the improved SIC algorithm/simulator is presented in Section 4.4.

It is assumed that SIC estimates with these simulators give accurate enough information on temporal and spatial SIC anomalies over the Arctic pack ice, and allow determination of possible SIC data improvements due to new definitions of the emissivities, T_{eff} 's, and other parameters.

4.1 OSI-408 SIC Simulation

The processing chain of the OSI-408 level 2 SIC product is shown in Figure 3 (Tian et al., 2015). In the first step, the atmospheric correction of the T_B data is conducted. Next, the daily dynamic tie points are generated. In the third step, SIC is calculated for each T_B swath dataset. The OSI-408 SIC L2 processing chain does not include any weather/open water filters.

The atmospheric correction of the T_B data is described in Section 4.3. The tie points for closed sea ice (CI) and open water (OW) are the set of T_B values that correspond to SICs of 100% and 0%, respectively. They are used in the SIC algorithms as a reference. In the OSI SAF SIC algorithms daily dynamic tie points are used, a method that minimizes the effects of the radiometer sensor drift, inter sensor calibration differences, and interseasonal and interannual variations of sea ice and open water emissivities, and trends potentially arising from the use of NWP reanalysed data to correct the T_B data (Laverne et al., 2019b).

In the OSI SAF SIC algorithms the CI training sample is based on the results of the NASA Team (NT) SIC algorithm (Cavalieri et al., 1984): locations for which the NT SIC value is greater than 95% are used as a representation of 100% sea ice (Lavergne et al., 2019b). Recent investigations, e.g. during the ESA CCI Sea Ice projects, confirmed that NT was an acceptable choice for selecting the CI samples (Lavergne et al., 2019b). It is noted that the pixels having $SIC > 95\%$ are determined with NT having input the original uncorrected T_B data, but the T_B data with the atmospheric correction enter the CI tie point sample data.

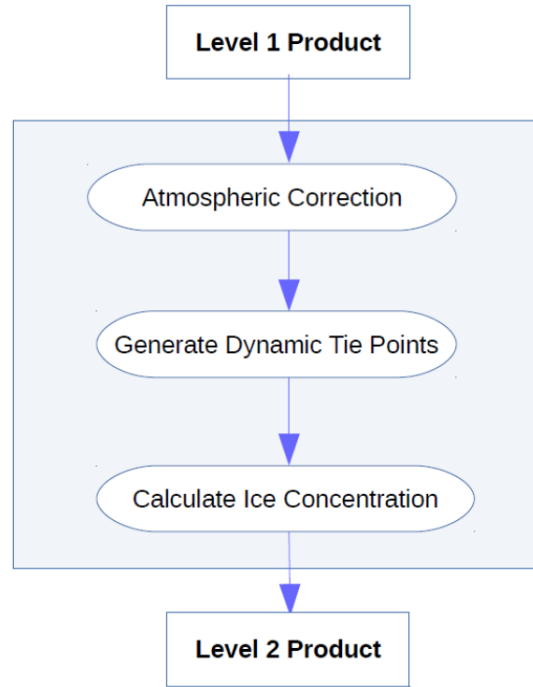


Figure 3. The OSI-408 level 2 SIC processing chain (Tian et al., 2015).

The T_B tie points used here for the NT SIC algorithm are from the SICCI Phase II report D2.1 (Tonboe and Pedersen, 2017), Tables 5-X ‘Tie-points for Northern Hemisphere used with non-atmospheric corrected TBs’. These Tables have AMSR-E and AMSR2 tie points which are somewhat different. The AMSR-E tie points are the same as those in Appendix A of (Ivanova et al., 2015). In the ESA SICCI climate data records (SICCI-25 km and SICCI-50 km) based on the AMSR-E and AMSR2 data the AMSR-E tie points are also used for the AMSR2 data (Lavergne et al., 2019b). However, we use here the AMSR2 tie points as they seem fit better to MYI data in the NT SIC algorithm triangle. In the OSI-408 processing chain static tie points by Comiso et al. (Comiso et al., 1997) are used (Tian et al., 2015).

The selection of the OW tie point samples follow here that in the OSI-450 processing chain (Lavergne et al., 2019b). The OW samples are collected over a belt just outside the monthly varying maximum ice extent climatology which is available in the OSI-450 product. The maximum width of this belt is around 300 km, and here the belt is located only in the Greenland and Barents Seas. The CI samples are not collected close to the coast (one or two pixels excluded) as land-spill over correction is not conducted. Figure 4 shows the mask for the collection of the CI and OW samples.

The OSI-408 processing chain produces two SIC products: OSI SAF Hybrid Dynamic (OSHD) SIC and Technical University of Denmark (TUD) Dynamic SIC (Tian et al., 2015). The latter is not simulated here; it includes the use of the 89 GHz data and combination of two SIC estimates at different resolutions. The OSHD SIC is a combination of the Bristol algorithm (input is T_{B18V} ,

T_{B36V} and T_{B36H} data) (Smith, 1996; Smith and Barrett, 1993) and the Bootstrap frequency mode (BMF) (Comiso, 1986a) (input is T_{B18V} and T_{B36V} data) SICs (Tian et al., 2015; Tonboe et al., 2016). The analysis of atmospheric sensitivity by Andersen et al. (2006) showed that the BFM algorithm had the lowest sensitivity to atmospheric noise over open water (Tonboe et al., 2016). Furthermore, the comparison to high resolution SAR imagery in (Andersen et al., 2007) revealed that among the SIC algorithms using the low frequency channels (19 and 37 GHz), the Bristol algorithm had the lowest sensitivity to ice surface emissivity variability. In addition, this algorithm had a low sensitivity to atmospheric emission in particular at high SICs. Consequently, the OSHD algorithm has been established as a linear combination of these two SIC algorithms. The BFM algorithm is used over open water and the Bristol (BRI) algorithm over sea ice. At intermediate SICs up to 40% (from the BFM SIC estimate) SIC is an average weighted linearly between the two algorithms (Tian et al., 2015; Tonboe et al., 2016):

$$SIC_{408} = (1 - wc)SIC_{BRI} + wc \cdot SIC_{BFM}, \quad (4)$$

$$wc = (|t - SIC_{BFM}| + (t - SIC_{BFM}))/ (2t),$$

where t is the SIC threshold of 40 %.

SIC with the BFM and BRI algorithms is calculated with the OW tie point, observed point and coordinates at the intersection of the ice line and the line from the OW tie point to the observed point (Tonboe and Pedersen, 2017). In the BRI algorithm the 3-D T_B data is first converted to a 2-D transformed coordinate system (i.e. to a plane) (Smith, 1996; Smith and Barrett, 1993):

$$B_x = T_{B36V} + 1.045 \cdot T_{B36H} + 0.525 \cdot T_{B18V}, \quad (5a)$$

$$B_y = 0.9164 \cdot T_{B18V} - T_{B36V} + 0.4965 \cdot T_{B36H} \quad (5b)$$

The BRI plane was chosen to contain both the ice line and the OW point in (Smith, 1996).

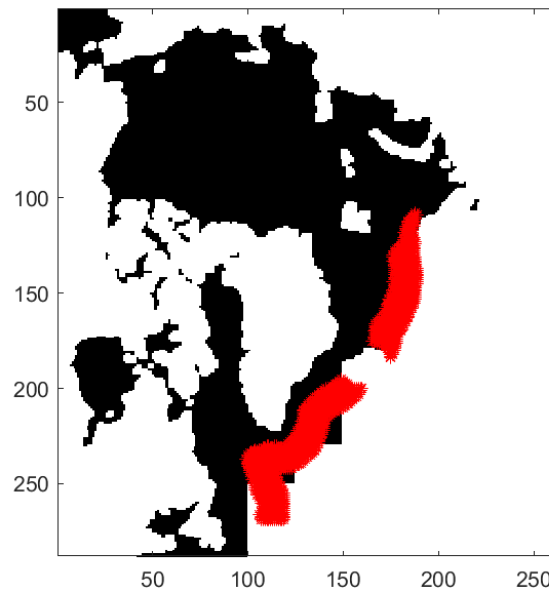


Figure 4. Mask for the collection of the CI and OW (red stars) samples.

The dynamical tie points; the coordinates of the ice line and the OW point, are computed using the CI and OW samples selected from the swath data for one day. They are computed separately for the BRI and BFM algorithms. The OW tie point is just mean values of T_B 's (BFM) or the Bristol coordinates in the daily OW sample. The ice line is determined with the principal component

analysis (PCA) and it is in the direction of the first component axis (highest variance) (Lavelle et al., 2016; Lavergne et al., 2019a). For the BFM we use T_{B18V} as X-coordinate and T_{B36V} as Y-coordinate in the PCA calculation. Here the ice line X-coordinates have the following constant values (*these were not specified in any OSI SAF publication, they can be freely chosen*):

$$T_{B18V}^A = 220 \text{ K}, T_{B18V}^D = 260 \text{ K}, B_x^A = 500 \text{ K}, B_x^D = 650 \text{ K} \quad (6)$$

The A-values are close to typical ones for MYI and the B-values those for FYI. The ice line Y-coordinates are then calculated from the X-coordinates and the line slope (2nd PCA score is zero).

In the operational OSI-408 SIC processing the final daily tie points are weighted means over the last 30 days (from day -29 to current day) of daily tie points (Lavelle et al., 2016). This weighting is not given in any OSI SAF publication. Here it is assumed to be arithmetic: from 1 for day -29 to 30 for current day.

The OSI-408 SIC simulator is summarized as:

AMSR2 L1R gridded T_B data \Rightarrow total SIC with the NT SIC algorithm using fixed tie points \Rightarrow T_B atmospheric correction \Rightarrow daily dynamical tie points for the Bristol and BFM algorithms (sea ice and open water samples as input) \Rightarrow final SIC as combination of the Bristol and BFM SICs

In the OSI SAF SIC uncertainty estimation one component is the inherent uncertainty of the SIC algorithm (σ_{algo}^2) which includes sensor noise and residual geophysical noise (atmospheric noise and surface emissivity variability) (Tonboe et al., 2016; Lavergne et al., 2019b). In the OSI SAF SIC products σ_{algo}^2 is estimated for every pixel based on the estimated SIC and standard deviations (STD) of the SIC values retrieved by the SIC algorithm for the OW and CI training samples (σ_{OW} and σ_{CI}). These sSTDs are used here as accuracy measures for the BRI and BFM algorithms.

4.2 OSI-450 SIC Simulation

The OSI-450 is also a hybrid SIC algorithm as it combines two SIC algorithms: one that is tuned to perform better over open-water and low SIC conditions (named B_{OW} for best open water), and one that is tuned to perform better over closed-ice and high SIC conditions (named B_{CI} for best closed ice) (Lavergne et al., 2019b). The combined SIC is a linear weighted average of B_{OW} and B_{CI} results (Lavergne et al., 2019a, 2019b):

$$SIC_{450} = w_{OW} B_{OW} + (1 - w_{OW}) B_{CI}, \quad (7)$$

$$w_{OW} = 1 \text{ for } B_{OW} < 0.7,$$

$$w_{OW} = 0 \text{ for } B_{OW} > 0.9,$$

$$w_{OW} = 1 - (B_{OW} - 0.7)/2 \text{ for } B_{OW} \in [0.7, 0.9].$$

The input data to B_{OW} and B_{CI} are T_{B18V} , T_{B36V} and T_{B36H} , same as for the Bristol (BRI) algorithm. B_{OW} and B_{CI} are generalizations of the BRI algorithm (Lavergne et al., 2019b). Like in BRI an optimal “data plane” is sought with the OW and CI samples on which to project the 3-D T_B data. This plane holds the closed-ice line (supported by unit vector u). The vector u is computed by PCA and is in the direction with highest variance in the CI samples (1st principal component axis). Conversely to BRI the OW tie point (mean of OW samples) is not imposed to be in the projection plane. Instead the plane is rotated around u and an optimal rotation angle (θ) is sought which yields the best SIC accuracy with B_{OW} or B_{CI} , i.e. the smallest STD of SIC with B_{OW} (OW samples) or B_{CI} (CI samples). By varying θ the optimization process samples several planes and eventually returns the optimal angles θ_{OW} and θ_{CI} that respectively define the B_{OW} and B_{CI} algorithms. This optimization step allows to cope with the anisotropy of the OW and CI samples in the 3-D T_B space (Lavergne et al., 2019b). The optimal θ for CI cases is generally not the same as that for the BRI

plane which is typically close to $+30^\circ$ (Lavergne et al., 2019b). The values of θ_{OW} and θ_{CI} will vary with the OW and CI signatures that exhibit regional, seasonal, and interannual variations. In general, B_{OW} and B_{CI} the algorithms are tuned to minimise STD of the retrieved SIC, while simultaneously achieving zero SIC bias on the average.

The B_{OW} and B_{CI} algorithms calculate SIC as a linear combination of T_B 's at three channels (Lavergne et al., 2019a):

$$B_{OW/CI} = a \cdot T_{B18V} + b \cdot T_{B36V} + c \cdot T_{B36H} + d. \quad (8)$$

This SIC equation can be described as a coordinate transform, that map a point in the 3-D T_B space into the 1-D axis of SIC. Such a coordinate transform is the composition of four steps: 1) a projection of a 3-D point onto a 2-D plane, 2) in that plane, a projection of the 2-D point onto a 1-D axis, 3) a scaling of the 1-D axis, and 4) a shift of its origin (Lavergne et al., 2019a):

$$B_{OW/CI} = \alpha(v_x \cdot T_{B18V} + v_y \cdot T_{B36V} + v_z \cdot T_{B36H}) + \beta. \quad (9)$$

The vector v is a unit vector perpendicular to u at rotation angle θ . Thus, u and v determine the optimal plane discussed above. The constant α is computed so that the difference between $B_{OW/CI}(CI)$ (the transformed mean CI point) and $B_{OW/CI}(OW)$ (the transformed mean OW point) is one, and the constant β such that $B_{OW/CI}(OW)$ is zero.

The processing chain of the OSI-450 level 2 SIC product is shown in Figure 5 (Lavergne et al., 2019a, 2019b). The OSI-450 product is calculated using SMMR, SSM/I and SSMIS data. Here we use AMSR2 data which is also used in the SICCI-25 km SIC product (Lavergne et al., 2019b). The processing chain can be summarized as:

AMSR2 L1R T_B data \Rightarrow open water samples outside SIE climatology and sea ice samples with NT total SIC > 95% \Rightarrow determine dynamic B_{OW} and B_{CI} (tie points and plane rotation angles) \Rightarrow SIC as combination of B_{OW} and B_{CI} \Rightarrow T_B atmospheric correction \Rightarrow open water and sea ice samples with corrected T_B 's (same pixels as previously) \Rightarrow determine dynamic B_{OW} and B_{CI} ; correction scheme over high SIC \Rightarrow final SIC as combination of B_{OW} and B_{CI} .

OW and CI samples are selected as in the OSI-408 simulator. In the OSI SAF level 2 processing the CI samples over the Arctic are selected only if their latitude is less than 84° which is the limit of the SMMR polar observation hole. This limitation was not used in here.

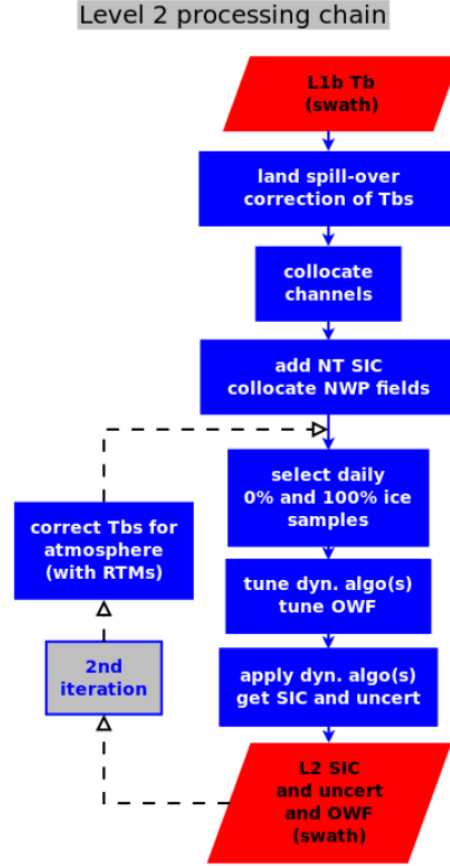


Figure 5. The OSI-450 level 2 SIC processing chain (Lavergne et al., 2019a, 2019b).

The dynamic tuning of the B_{OW} and B_{CI} algorithms for each day is conducted using CI and OW samples from ± 7 days sliding window (Lavergne et al., 2019b). This time interval should allow the tie points to react rapidly to seasonal cycles, e.g. onset of melting. The tuning of B_{OW} and B_{CI} is conducted here as follows:

1. The ice line, i.e. the u vector, in the $(T_{B18V}, T_{B36V}, T_{B36H})$ space is determined with the CI samples from ± 7 days using PCA. The u vector is expressed with spherical coordinates as:

$$u = [x \ y \ z] = [\cos\varphi_s \sin\theta_s \ \sin\varphi_s \sin\theta_s \ \cos\theta_s] \quad (10)$$

where $\theta_s = \text{atan}(u(2)/u(1))$ and $\varphi_s = \text{acos}(u(3)/\|u\|)$

2. Two unit vectors perpendicular to u are formed as:

$$v_1 = \frac{du}{d\varphi_s} = [-\sin\varphi_s \sin\theta_s \ \cos\varphi_s \sin\theta_s \ 0], \quad (11)$$

$$v_2 = \frac{du}{d\theta_s} = [\cos\varphi_s \cos\theta_s \ \sin\varphi_s \cos\theta_s \ -\sin\theta_s]$$

v_2 is unit vector, but v_1 is normalized to an unit vector by $v_1 = v_1/\|v_1\|$.

3. Vector v perpendicular to u at rotation angle θ is formed as:

$$v = \cos(\theta) v_1 + \sin(\theta) v_2, \quad (12)$$

The 0° reference for θ is the $T_{B18V} - T_{B36V}$ plane where v_1 lies.

4. The rotation angle θ is varied from -90° to $+90^\circ$ with 1° step. At each θ v is calcuted and B_{OW} and B_{CI} equations in (9) are determined.

5. STD of B_{CI} with CI samples and STD of B_{OW} with OW samples are calculated at each θ , and minimums are sought. These represent optimal B_{OW} and B_{CI} equations.

The tuning B_{OW} and B_{CI} is conducted two times, with the original and corrected T_B data. The STD of SICs with B_{OW} and B_{CI} are used as their uncertainty measures.

The OSI-450 includes in the 2nd iteration (see Figure 5) also correction for systematic SIC errors observed in wintertime over high SIC areas in the Arctic (Lavergne et al., 2019b). Analysis on the spread of the CI samples along the ice line showed systematic deviations which are stable with time. These systematic deviations form a CI curve, see Figure 3 in (Lavergne et al., 2019b). They are best shown in a coordinate system of $u \cdot T_{B3}$ vs. $B_{CI}(T_{B3})$ where the first is a dot product between u and T_B triplet (T_{B3}) in (8) and (9). The dot product is the distance along the ice line (DAL) which is small for MYI and large for FYI. In winter Arctic conditions, it was typically observed that $B_{CI}(T_{B3})$ values are consistently lower than 100% (down to 85-90 %) for MYI and higher than 100% (up to 105-110%) for new ice and FYI. The correction scheme by Lavergne et al. (2019b) moves the concept of an ice line to an ice curve that more closely follows the $B_{CI}(T_{B3})$ samples along the u axis. A new ice curve is tabulated for each day by binning the $B_{CI}(T_{B3})$ values by their DAL values. This SIC bias correction is applied only in the 2nd iteration after the B_{CI} calculation. Unfortunately, more details are not given in (Lavergne et al., 2019b), e.g. what DAL bin width(s) are used, and what polynomial is fitted to the binned means/modes? This correction scheme is not described in the OSI-450 ATDB document (Lavergne et al., 2019a). Therefore, it is somewhat difficult to apply it here. Following procedure is used:

- The range of the daily DAL values is split into 10 K wide bins.
- Mean of $B_{CI}(T_{B3})$ in each DAL bin is calculated if there is more than 1000 samples.
- To the resulting DAL vs. mean $B_{CI}(T_{B3})$ curve a 4th degree polynomial is fitted; Matlab's polyfit-command. Other option would be to use interpolation of the curve to wanted DAL resolution (e.g. Matlab's interp1 with 'spline' option), but here the interpolated curve needs to be saved, whereas with the polyfitting only polynomial coefficients, and the DAL resolution is not fixed.
- Each $B_{CI}(T_{B3})$ value is corrected by $1 - B_{CI}(T_{B3})$.

Finally, the OSI-450 processing chain has an open water filter (OWF) based on dynamic thresholding of $GR3618V$. Also SIC_{450} values below 0.1 are flagged as zero. Here OWF with a fixed threshold by (Cavalieri et al., 1995) is used:

$$\text{OWF: } GR3618V > 0.05 \text{ or } SIC_{450} \leq 0.1 \quad (13)$$

4.3 Atmospheric Correction of T_B Data

The T_B atmospheric correction scheme implemented in the OSI-450 product (from SSM/I and SSMIS data) is based on a double-difference scheme (Lavergne et al., 2019b), similar (but not identical) to that described in (Andersen et al., 2006) or (Tonboe et al., 2016). The T_B correction equations are from (Wentz, 1997). In the OSI-SAF 408 (from AMSR2 data) the T_B correction follows Wentz and Meissner (2000), and it is described in detail in (Tian et al., 2015). The OSI SAF T_B correction scheme evaluates a correction offset ΔT_{Bc} , as the difference between two runs of the T_B simulations with a parametrized RTM (Lavergne et al., 2019b): T_{Bnwp} uses atmospheric data (2-m T_a , 10-m wind speed (W), and total column water vapour (WV)) from the ERA-Interim fields and estimated SIC with the original T_B data, while T_{Bref} uses a reference atmospheric state with the same T_a as in T_{Bnwp} , and thus, also the same T_{eff} , but zero W and zero WV . SIC is the same as in

$T_{Bnwp} \cdot \Delta T_{BC}$ is thus an estimate of the atmospheric contribution (water vapour) at the time and location of the T_B measurement. The T_B data are not corrected for the influence of the total column liquid water (clouds) (LW) as it has been found out that NWP model representation of LW is not adequate to be used in the atmospheric correction (Andersen et al., 2006; Ivanova et al., 2015; Tonboe et al., 2016). The spatial and temporal variability of clouds is typically higher than the NWP model grid cell size and model time step size. The typical values of ΔT_{BC} range from about 10 K over open water to few tenths of a kelvin over consolidated sea ice (Lavergne et al., 2019b). The corrected T_B is calculated as (Andersen et al., 2006; Ivanova et al., 2015; Lavergne et al., 2019b):

$$T_{BC} = T_B - (T_{Bnwp} - T_{Bref}), \quad (14)$$

$$T_{Bnwp} = T_B(f, p, \theta_0, e, WV, W, T_s, SIC), \quad (15)$$

$$T_{Bref} = T_B(f, p, \theta_0, e, 0, 0, T_s, SIC), \quad (16)$$

where θ_0 is the radiometer viewing angle (55° for AMSR2), and T_s is the surface or effective temperature. For the OSI-450 product following simplified radiative transfer equation for T_B from a mixed surface with two different emissivities (ocean and sea ice) is used (Wentz, 1997; Andersen et al., 2006):

$$T_B = T_{BU} + SIC \left(e_{si} T_{eff} + (1 - e_{si})(T_{BD} + \tau T_{BC}) \right) \tau + \\ (1 - SIC) \left((1 - R_s) T_{ss} + R_s (\Omega T_{BD} + \tau T_{BC}) \right) \tau, \quad (17)$$

where T_{BU} and T_{BD} are the upwelling and downwelling atmospheric brightness temperatures, τ is the transmittance through the atmosphere, R_s is the sea surface reflectivity, T_{ss} is the sea surface temperature, T_{BC} is the cosmic background radiation temperature (2.7 K), and Ω is the sea surface reflection reduction factor due to wind induced surface roughness. The reflection from the sea ice surface is always assumed to be specular. For the OSI-408 AMSR2 SIC product the T_B radiative transfer equation follows (Wentz and Meissner, 2000) and is somewhat different for the ocean part:

$$T_B = T_{BU} + SIC \left(e_{si} T_{eff} + (1 - e_{si})(T_{BD} + \tau T_{BC}) \right) \tau + \\ (1 - SIC) \left((1 - R_s) T_{ss} + ((1 + \Omega)(1 - \tau)(T_D - T_{BC}) + T_{BC}) R_s \right) \tau, \quad (18)$$

where $T_D = T_{BD}/(1 - \tau)$ is the downwelling effective air temperature. In (18) Ω for smooth surface is zero, but in (17) it is one. Also in (18) T_{BC} is scattered from ocean surface, but in (17) it is reflected. With specular ocean surface (17) and (18) are equal. Here T_{Bnwp} and T_{Bref} are calculated using (18) in both the OSI-408 and OSI-450 SIC simulators (i.e. using the RTM model by (Wentz and Meissner, 2000)).

In the OSI SAF atmospheric correction fixed sea ice emissivities in Table 1 are used for all ice seasons and ice types, and sea ice T_{eff} is calculated a linear mixture between sea ice surface temperature (T_{ssi}) and freezing temperature of 272 K (Ivanova et al., 2013; Tian et al., 2015):

$$T_{eff} = T_{mix} \cdot T_{ssi} + (1 - T_{mix}) \cdot 272 \quad (19)$$

The mixing coefficient T_{mix} is shown in Table 1. The T_{mix} value of 0.4 is a default one originating from (Svendsen et al., 1983). T_{ssi} is taken to be same as ERA-Interim 2-m T_a . The ERA-Interim skin temperature data has been found to have erroneous spatial jumps over sea ice (*by OSI SAF team*), and thus, has not been used so far. Previously, Ivanova et al. (2015) used fixed reference T_{eff} of 265 K for T_{Bref} . A fixed reference T_{eff} was also in (Mäkynen and Similä, 2019).

It is noted that the same T_{eff} is used in the calculation of T_{Bref} and T_{Bnwp} . This means that spatial and temporal variation of T_{eff} is not compensated in the T_B correction.

Table 1. OSI SAF sea ice emissivities and coefficients for calculating sea ice effective temperature from (19) at different AMSR-E/AMSR2 channels.

	6.9V	6.9H	10.65V	10.65H	18.7V	18.7H	36.5V	36.5H	89V	89H
emissivity	0.96	0.88	0.9	0.9	0.95	0.90	0.93	0.88	0.90	0.83
T_{mix}	0.45	0.40	0.4	0.4	0.75	0.47	0.95	0.70	0.97	0.97

4.4 Improved SIC Derivation

The simulator for improved SIC data follows the OSI-450 simulator, but it has dynamic sea ice emissivities and T_{eff} 's, and their winter season reference values in the T_B atmospheric correction. The simulator for improved SIC data has the following components:

- 1) Calculation of the NT total, FYI and MYI SICs using the fixed AMSR2 tie points in (Ivanova et al., 2015) and the original gridded L1R T_B data.
- 2) Collection FYI and MYI samples from the L1R swath datasets, and calculation of T_{eff} 's and apparent emissivities ($e_a = T_B/T_{eff}$) for the FYI and MYI samples. T_{eff} can be calculated either from T_a (Mathew et al., 2009) or from the T_B data (Kilic et al., 2019). Collection of sea ice (total SIC>95%) and open water (outside monthly SIE climatology) samples as in the OSI-450 simulator.
- 3) Calculation of dynamic daily T_{eff} ' and e_a 's for FYI and MYI, and their winter season reference values, see Section 6. These parameters are used in the T_B atmospheric correction.
- 4) Atmospheric correction of the T_B data following Section 4.3 using T_{eff} and e_a parameters from 3) and total SIC from the daily optimal B_{OW} and B_{CI} as in the OSI-450 simulator. The FYI and MYI T_{eff} 's and e_a 's are combined to pixel-wise parameters based on FYI and MYI SICs, see Section 7.
- 5) Collection open water and sea ice samples with corrected T_B 's (same pixels as previously).
- 6) Determination of the daily optimal B_{OW} and B_{CI} as in the OSI-450 simulator, including the curved ice line correction in B_{CI} (two versions of B_{CI}).
- 7) SIC calculation for each swath dataset (L2 data), with and without the curved ice line correction.

The T_{eff} estimation by Kilic et al. (2019) uses radiometer V-polarization channels from 6.9 to 36.5 GHz, and results in T_{eff} data at the same spatial resolution as SIC is estimated. However, this method is valid only for sea ice with 100% SIC. Nevertheless, it is tested over the Arctic pack ice, and further, a possible correlation between Kilic's T_{eff} and T_a is investigated for the T_{eff} estimation over sea ice with SIC<100%.

5 Thin Ice Detection with the AMSR2 Data

In the following a recently developed algorithm for the thin ice detection in BKS with the AMSR2 36.5 and 89 GHz data is first introduced (Mäkynen and Similä, 2019). This algorithm is not used here due to reasons explained below; in general, the algorithm needs further developments before its usage over the whole Arctic. Next, we investigate if thin ice detection with reasonable accuracy can be conducted using a single *PR* or *GR* or their combination in the 10.65 to 36.5 GHz frequency range following previous studies by Mäkynen and Similä (2015) and Cavalieri (1994). The detected thin ice pixels would be excluded from the determination of the tie points in the improved SIC simulator.

Previously, a simple thin ice detection algorithm using the AMSR2 18.7 GHz T_B 's has been developed in (Cho et al., 2016, 2019). The algorithm is based on the T_{B18V} and the difference $T_{B18V} - T_{B18H}$. Thin ice is detected with a linear threshold in the 2-D T_{B18V} vs. $T_{B18V} - T_{B18H}$ space. The detection is only applied when SIC is larger than 80%. This minimum SIC is detected with a T_{B18V} threshold which is adjusted to different seas, e.g. Sea of Okhotsk and Bering Sea (Cho et al., 2016). The 89 GHz T_B difference $T_{B89V} - T_{B89H}$ can be used to reduce erroneous thin ice detection over consolidated ice. The maximum h_i of the detected thin ice is around 30 cm. The algorithm was developed with help of the MODIS optical imagery at bands 1 and 2 (250 m resolution). It seems that detailed validation studies of this algorithm have not yet been conducted, and therefore, it is not applied here. The AMSR2 thin ice detection algorithm by Cho et al. (2019, 2016) is used to produce JAXA AMSR2 Research Product 'Detection of thin sea ice' (see https://suzaku.eorc.jaxa.jp/GCOM_W/data/data_w_product-3.html). The grid size of this product is 15 km, and its accuracy goal is 80%.

The NT SIC algorithm (Cavalieri et al., 1984, 1991) was modified by Cavalieri (1994) for mapping the distribution of new ice (thickness < 10 cm), young ice (10-30 cm) and FYI in seasonal ice zones and to reduce the low SIC bias due to thin ice types. First, the improved SIC estimate is derived with *PR19* and *GR3719V* and tie point signatures for open water, FYI and new ice, and then the ice type classification is conducted based on typical *PR19* ranges for each ice type. A comparison with ice type classifications from the AVHRR (Advanced Very High Resolution Radiometer) imagery over the Bering Sea showed on the average 80% correspondence. The algorithm has been applied to the Sea of Okhotsk after adjustment of the new ice tie point (Kimura and Wakatsuchi, 1999). The ice type classification was conducted only when SIC was larger than 30%. The type ice classification is subject to ice type mixture ambiguities (Cavalieri, 1994). It seems that neither further validation studies nor algorithm developments have been conducted.

There are two inherent problem in thin ice detection and its h_i estimation with the radiometer data. The first one is T_B signature mixing from various surface types (open water, thin ice, FYI, landfast ice) due to coarse resolution of the radiometer data, e.g., thin ice with SIC close to 100% may have similar signatures as thick ice with low SIC. This error can be somewhat mitigated by setting a high SIC threshold (like 70% or 80%) for the thin ice detection, but unfortunately various radiometer SIC algorithms underestimate SIC for thin ice areas, e.g. (Cavalieri, 1994; Shokr and Kaleschke, 2012; Ivanova et al., 2015). Secondly, thin ice signatures can be equal to those of thick ice due to rough ice surface, ice surface properties, and dry snow layer or frost flowers on thin ice (Hwang et al., 2007; Nihashi et al., 2009; Shokr et al., 2009). Nevertheless, many studies have demonstrated that useful data on thin ice properties can be retrieved from the radiometer data (Cavalieri, 1994; Iwamoto et al., 2014; Ohshima et al., 2016; Nakata et al., 2019; Mäkynen and Similä, 2015, 2019).

5.1 AMSR2 thin ice detection with *PR36* and *GR8936H*

Previously, Mäkynen and Similä (2019) have developed AMSR2 thin ice detection algorithm (ATIDA) for the Barents and Kara Seas based on *PR36* and *GR8936H* calculated from the AMSR2 L1R data. ATIDA was developed using MODIS h_{iM} swath charts for 2014-2015 (two winters) as reference data. It is based on classification of *PR36* and *GR8936H* signatures with a linear discriminant analysis (LDA) classifier (Hastie et al., 2009). For the thin ice detection the LDA discriminant, or score, function is calculated as (Mäkynen and Similä, 2019):

$$LDA_s = 45.6 \cdot PR36 + 29.6 \cdot GR8936H - 0.7, \quad (20)$$

and thin ice is detected if:

$$LDA_s > 0.6. \quad (21)$$

The maximum h_i of detected thin ice was estimated to be 20 cm. In many polynya monitoring studies using radiometer data, the same maximum h_i for thin ice has been used, e.g. (Iwamoto et al., 2014; Ohshima et al., 2016; Nakata et al., 2019). The thin ice detection is conducted only when $SIC \geq 70\%$ and $T_a \leq -5$ °C. The chosen SIC threshold is the lower limit for ‘close ice’ in the WMO sea ice nomenclature (JCOMM Expert Team on Sea Ice, 2014). This SIC limitation reduces errors due to the mixture of open water and thick ice which may have similar signature as thin ice. We assume thin ice detection to be too unreliable in conditions warmer than -5 °C, occurring mostly at the beginning of freeze-up and early melt conditions. Snow cover on sea ice can be already slightly moist when snow temperature is below freezing. Both *PR36* and *GR8936H* for FYI increase from winter to melting conditions (based on emissivities in (Mathew et al., 2009)), and therefore, thin ice and FYI *PR36* and *GR8936H* signatures could be too similar when $T_a > -5$ °C.

Before calculation of *PR36* and *GR8936H* atmospheric correction is applied to the AMSR2 L1R T_B data following (Andersen et al., 2006; Ivanova et al., 2015; Lavergne et al., 2019b), but only the sea ice part of the correction is applied, i.e. SIC is assumed to be always 100%. The effect of the atmospheric correction is significant only for *GR8936H*. The correction decreases misclassification of thick ice as thin ice, as the atmospheric influence increases *GR8936H*.

ATIDA was developed for $T_a < -20$ °C due to lack of thick ice samples in the combined MODIS-AMSR2 training dataset in warmer temperatures. Unfortunately, this is an inherent property of the MODIS h_{iM} data as T_s vs. h_i has the largest dynamic range in very cold conditions ($T_a < -25$ °C) (Yu and Rothrock, 1996; Mäkynen et al., 2013). It was found out that *PR36* and *GR8936H* signatures (after the atmospheric correction) increase on average slightly as a function of T_a , and therefore, following empirical relationships between the average signatures and T_a are used to normalize them to fixed T_a of -25 °C (see details in Section III.B of (Mäkynen and Similä, 2019)):

$$PR36_m = 0.0007T_a + 0.050, \quad (22a)$$

$$GR8936H_m = 0.0014T_a - 0.002. \quad (22b)$$

The rate of change is very small for $PR36_m$, only 0.007 per 10 °C, and for $GR8936H_m$ it is two times larger (0.014/10 °C). Likely it would be better to use temporally (e.g. monthly, bi-weekly) varying LDA classifier parameters and thin ice detection threshold, but this was not possible with the training dataset available.

The thin ice swath charts (L2 products) are combined to a more reliable daily thin ice chart (L3 product), see details in (Mäkynen and Similä, 2019) and an example in Figure 6. For assigning a pixel as thin ice in the daily chart the fraction of daily thin ice detections must be over 50%. Pixels which had only unknown ice type assignments ($T_a > -5$ °C) during a day are flagged as such in the chart. The daily charts shows five WMO SIC classes (JCOMM Expert Team on Sea Ice, 2014):

SIC \leq 10%, 10<SIC \leq 40%, 40<SIC<70%, 70 \leq SIC \leq 90%, and SIC>90%, and detected thin ice on the last two classes.

The daily thin ice chart was validated using an independent set of MODIS daily h_{iM} charts for Oct 2015 – May 2016 (Mäkynen and Karvonen, 2017; Mäkynen and Similä, 2019). The average error for detecting thick ice as thin ice (type I error) was 10%, and 32% for the vice versa case (type II error). ATIDA was tuned to give small type I error which is important when applying the thin ice chart for ship navigation or for enhancing visual or automatic SAR imagery interpretation. In the daily thin ice charts for BKS in 2015-2016, the daily SIC was from 70% to 90% for roughly 60% of the thin ice pixels. This demonstrates that the detected thin ice is not always just FYI with low SIC. ATIDA was developed for the Barents and Kara Seas, but it should also be applicable for other Arctic marginal ice zones (MIZs).

The daily thin ice chart was found to have on average rather good day to day consistency in the thin vs. thick ice classification. There are sometimes cases where a large area of thick ice is detected as thin ice on the following day (see Fig. 12 in (Mäkynen and Similä, 2019)). This could be induced by a significant decrease in SIC for thick ice (diverging sea ice motion), but more likely it is due a change in snow or sea ice properties induced by T_a increasing close to 0 °C, which makes thin and thick ice PR_{36} and GR_{8936H} signatures resemble each other. On average no correlation was found between the type I and II errors and the daily mean T_a which shows that the approximate T_a scaling of PR_{36} and GR_{8936H} by (22) works properly.

Currently, ATIDA is under further development at FMI, e.g. how the AMSR2 lower frequency channels, 10.65 and 18.7 GHz, could be used improve the thin ice detection, and what possible modifications are needed to apply ATIDA over the whole Arctic. Therefore, ATIDA is not applied in this study.

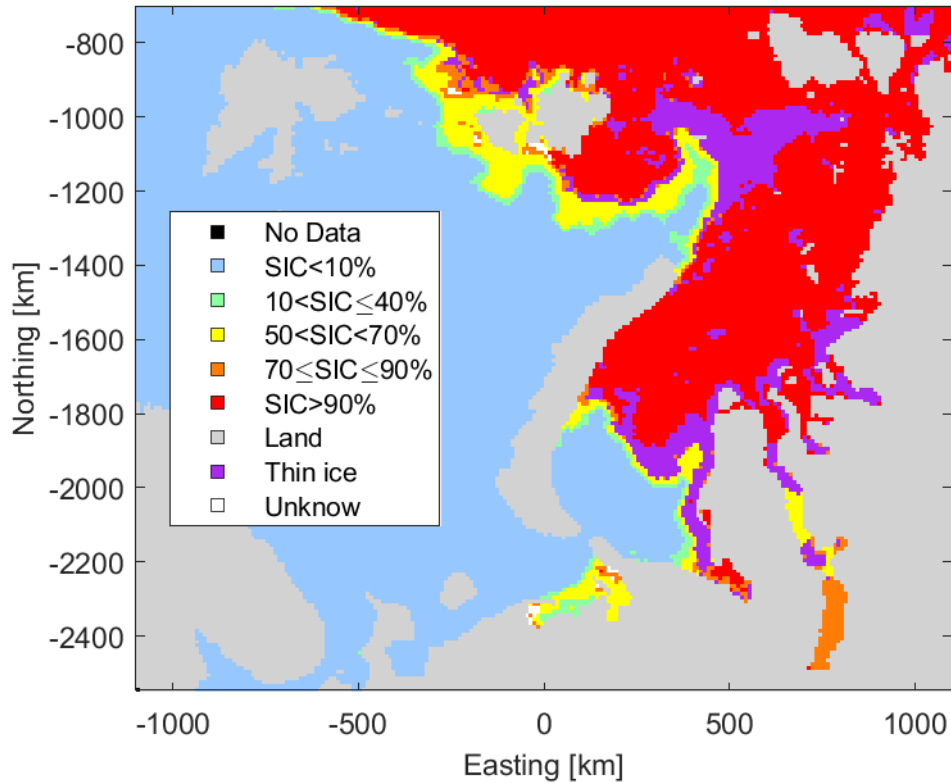


Figure 6. AMSR2 daily thin ice chart over the Barents and Kara seas on 2 December 2015.

5.2 AMSR2 thin ice detection in the 10.65 to 36.5 GHz frequency range

We study here thin ice (thickness up to 20 cm) detection over the Barents and Kara Seas (see Figure 6) using the combined MODIS – AMSR2 thin dataset described in Section 3.4. This dataset has 20 km pixel size. The detection of thin ice is studied using different PR 's and GR 's in the 10.65 to 36.5 GHz frequency range, and the goal is to find the best single parameter or a $PR - GR$ combination for the detection. This study is conducted following (Mäkynen and Similä, 2015) where thresholds, maximum thicknesses, and accuracies in thin ice detection with different AMSR-E and SSMIS PR 's and GR 's from 36/37 and 89/91 GHz T_B daily gridded data were determined. The best single parameter was AMSR-E $GR8936H$ and the best two parameter combination was $PR36$ and $GR8936H$ which were used to form a LDA classifier for the thin ice detection; similar as in (20) and (21), but with different LDA coefficients and threshold. With $GR8936H$ the maximum thickness of detected thin ice was 25 cm and the probability for misclassification of thicker ice as thin ice (type I error) was 16% and that for misclassification of thin ice as thicker ice (type II) was 27%. Here PR 's and GR 's involving the 89 GHz T_B data are not used due to large atmospheric influence at 89 GHz and lack of cloud liquid water compensation in the T_B atmospheric correction.

The AMSR2 data is divided into thin ($\bar{h}_{iM} \leq 0.2$ m) ice class and into two thick ice classes; $0.2 < \bar{h}_{iM} < 1.0$ m (thick1 class) and $\bar{h}_{iM} \geq 1$ m (thick2; \bar{h}_{iM} set to 1 m). The number of samples for these three classes are 6622, 9759 and 11427, respectively. Roughly 90% of thick1 class samples are for $T_a < -20$ °C. For thin ice this fraction is 58%. For the thick2 class $T_a < -25$ °C always. The samples were not divided into different T_a regimes as most of the thick ice samples are for the cold conditions.

It was concluded that the estimation of thin ice thickness was not possible with reasonable accuracy due to the large scatter between the MODIS h_{iM} and $PR36$ and $GR8936H$ data (Mäkynen and Similä, 2015, 2019). This contrary result compared to many other studies, e.g. (Iwamoto et al., 2014; Ohshima et al., 2016; Nakata et al., 2019), was likely mainly due to very large training datasets which included besides thin ice in polynyas also thin ice at the ice edge and large thin ice areas from the freeze-up period. The confidence of any equation fitted to the data in a least squares sense would have been poor. The large scatter present also in the data here is illustrated with $PR18$ vs. h_{iM} in Figure 7.

Figure 8 shows these three ice type classes in the NT algorithm triangle. Only thin ice samples having high $PR18$ are distinct from the two thick ice classes. In general, thin ice samples cover rather similar $PR18$ vs. $GR3618V$ space as in (Cavalieri, 1994).

Next, all thin ice and thick1 samples are used to determine optimal thin ice detection thresholds for various PR 's and GR 's. The thresholds together with the type Ia error, (thick1 as thin ice), type Ib (thick2 as thin ice), and type II error rates are shown in Table 2. The threshold was determined as an intersection (with 0.005 resolution) between pdf's for the thin ice and thick1 classes. These pdf's were calculated with the kernel density estimation using a normal kernel with bandwidth (i.e. STD) of 0.005 which is assumed PR and GR sensitivity. The type I and II errors were calculated from the empirical PR/GR and h_{iM} data because this approach provides more accurate error rate estimates than the probabilities based on the modelled pdf's. The best PR for the thin ice detection is $PR10$ (type Ia error is 16% and type II is 31%), but $PR18$, which can be calculated with the SSM/I and SSMIS data, has only slightly worse (3%) type II error. The best GR is $GR3618H$ with type Ia and II errors of 18% and 32%, respectively. The type Ib error is very small with all parameters. Together $PR18$ and $GR3618H$ give somewhat better type II error, 25%, than either one of them alone, but the type Ia error is 6 or 7% worse, being 24%. The rather high type Ia error, i.e. thick ice detected as thin ice, is not a problem here as thick ice signatures resembling those of thin ice are excluded from the determination sea ice tie points in the improved SIC algorithm.

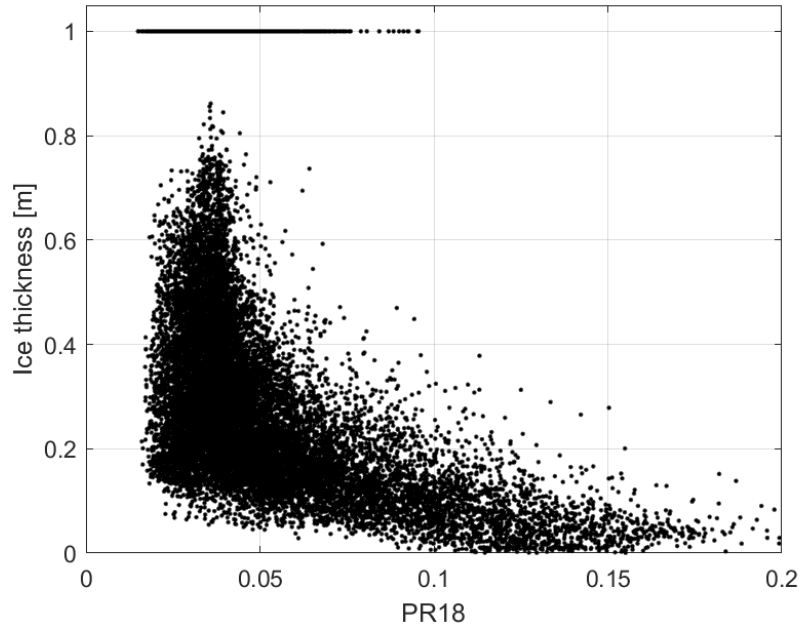


Figure 7. Scatterplot between the MODIS ice thickness and AMSR2 *PR18*. The pixel size of the dataset is 20 km. Samples along the 1 m thickness line represent thick2 class.

In summary, thin ice detection over FYI is conducted with:

$$PR18 > 0.05 \text{ or } GR3618H > 0.01 \quad (23)$$

It is noted that the thin ice detection is only for the determination of the tie points (sea ice emissivities and T_{eff} 's) in the T_B atmospheric correction and the 100% ice line in the SIC algorithms. It will be not used for any adjustment of retrieved SIC values. Equation (23) will be applied to both the original and corrected T_B data.

Table 2. Thin ice (<20 cm) detection with various AMSR2 various *PR*'s and *GR*'s in the 10.65 to 36.5 GHz range. Pixel size of the data is 20 km. Same thin ice and thick1 data were used in the determination of the threshold and the error rates.

Parameter	Threshold	Type Ia ¹⁾ error [%]	Type II error [%]	Type Ib ²⁾ error [%]
<i>PR10</i>	0.055	16	31	2.7
<i>PR18</i>	0.05	15	34	7.7
<i>PR36</i>	0.04	9	44	7.4
<i>GR3610V</i>	0.0	10	46	0.0
<i>GR3610H</i>	0.02	17	37	0.2
<i>GR3618V</i>	-0.005	27	27	0.1
<i>GR3618H</i>	0.01	18	32	0.2
<i>GR1810V</i>	0.005	5	70	0.0
<i>GR1810H</i>	0.01	20	44	2.0

1) Misclassification of thick1 class as thin ice.

2) Misclassification of thick2 class as thin ice.

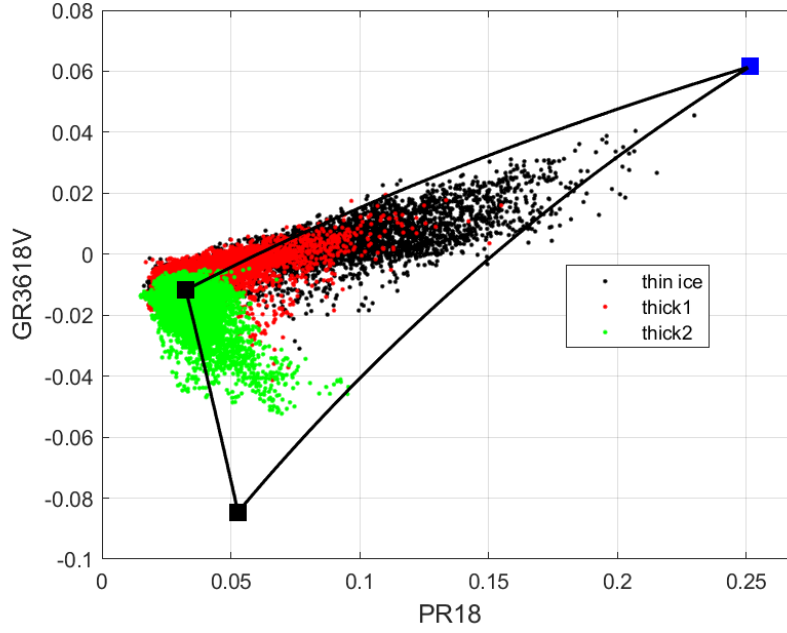


Figure 8. AMSR2 PR_{18} and GR_{3618V} signatures for thin ice (MODIS $\bar{h}_{iM} \leq 0.2$ m) and two thick ice classes, $0.2 < \bar{h}_{iM} < 1.0$ m (thick1 class) and $\bar{h}_{iM} \geq 1$ m (thick2), in the NASA Team algorithm triangle calculated with the AMSR2 tie points (Tonboe and Pedersen, 2017).

6 New Sea Ice Emissivities and Effective Temperatures for the T_B Atmospheric Correction

In the OSI SAF SIC products fixed sea ice emissivities (e_{si}) in Table 1 are used in the T_B atmospheric correction (see Section 4.3). These are also used here for the default SIC simulator (Section 4.4). Mathew et al. (2009) derived monthly mean (and STD) FYI and MYI e_{si} 's using AMSR-E data over the Kara Sea (FYI) and north of Greenland (MYI) for the year 2005. The e_{si} derivation required simulation of T_B 's with $e_{si} = 0$ and $e_{si} = 1$. This was conducted with the MWMOD RTM model. Mäkynen and Similä (2019) used averages of wintertime (Nov to Apr) monthly FYI e_{si} 's in the T_B atmospheric correction. At 18 and 36 GHz these are:

$$e_{18V} = 0.966, e_{18H} = 0.888, e_{36V} = 0.940, e_{36H} = 0.864 \quad (24)$$

These FYI e_{si} 's are very close to the OSI SAF ones, and their use instead would not improve the SIC data quality. However, for MYI the mean e_{si} 's are clearly smaller than the OSI SAF ones:

$$e_{18V} = 0.886, e_{18H} = 0.811, e_{36V} = 0.756, e_{36H} = 0.697 \quad (25)$$

Use of separate FYI and MYI e_{si} 's requires identification of these two ice types in the T_B data correction. This can be conducted with the NT SIC algorithm which gives FYI and MYI concentrations (SIC_{FYI} and SIC_{MYI}) in addition to the total SIC (Cavalieri et al., 1984, 1991). In the OSI-408/450 T_B correction the same T_a , and thus same T_{eff} by (19), is used for T_{Bref} and T_{Bnwp} . Previously, Ivanova et al. (2015) used a fixed reference T_{eff} (T_{effref}) for T_{Bref} and Mäkynen and Similä (2019) used reference T_a (T_{aref}) which was used to obtain T_{effref} 's. Mäkynen and Similä (2019) determined T_{aref} for the Barents and Kara Seas in winter conditions as modal T_a in three winters of the ERA-Interim T_a data.

We investigate here empirical determination of FYI and MYI e_{si} 's as a function of time. Using the available data true e_{si} 's cannot be estimated. Instead, an 'apparent' e_{si} which includes a contribution of the atmospheric state (e.g. water vapour and cloud liquid water) is calculated as:

$$e_a = T_B/T_{eff}. \quad (26)$$

T_{eff} can be calculated as in the OSI SAF 450 and 408 products, see (19) and Table 1, or by Mathew et al. (2009) T_{eff} vs. T_a relationships separately for FYI and MYI. It can be also estimated from the radiometer data (Kilic et al., 2019). The effect of the atmosphere can be reduced by collecting e_a data over a time period, e.g. ± 7 days sliding time window used in the OSI-450 product for the determination of the dynamical tie points, and taking some statistical parameter (mean, mode, 10% percentile, etc.) of e_a to approximate true typical e_{si} during that time period. It is noted that the resulting statistical e_a will be used only in the T_B atmospheric correction. Similar e_a estimation method was used by Andersen (1998) to calculate monthly time scale e_{si} tie points over the Arctic.

The sea ice emissivities can be estimated in two different ways:

1) The NT SIC algorithm is used to find FYI and MYI pixels with high ice type SICs. All FYI and MYI e_a estimates at each channel are grouped together in a temporal scale, e.g. in ± 7 days sliding time window, and some statistical parameter (e.g. 10 % percentile) is used to represent true FYI and MYI e_{si} 's for the T_B atmospheric correction.

2) Total SIC is estimated with the NT (or Bristol) algorithm, and for each AMSR2 swath dataset e_a 's at each channel are estimated for pixels with SIC > 95% (or some other high threshold). Next, all swath e_a datasets are stacked in a chosen temporal scale (e.g. ± 7 days sliding time window) and for pixels which have some minimum number of e_a estimates (e.g. 50 or 100) a statistical parameter (e.g. 10 % percentile) of e_a is calculated. This results in e_a maps over the Arctic, but these maps have holes due to missing data and ice edge areas do not have much data in general due to prevailing low SIC. Thus, spatial interpolation is needed. In addition, ice drift causes spatial averaging, i.e. loss of details, in the e_a maps.

We use here only the method 1) for the statistical FYI and MYI e_a derivation. In the following calculation of T_{eff} with two different methods is first presented (Mathew et al., 2009; Kilic et al., 2019). Next, FYI and MYI e_a 's based on these two T_{eff} estimates are derived.

6.1 Sea ice effective temperature from air temperature

T_{eff} in (26) can be calculated as in the OSI SAF 450 and 408 products, see (19) and Table 1. Mathew et al. (2009) found that T_{eff} of FYI and MYI at each AMSR-E frequency are linearly related to the lowest level air temperature (T_{al}) (i.e. snow surface temperature, in the Celsius scale), e.g. at 18.7 and 36.5 GHz:

$$T_{eff36FY} = 0.30 \cdot T_{al} - 4.9, T_{eff18FY} = 0.29 \cdot T_{al} - 5.0. \quad (27a)$$

$$T_{eff36MY} = 0.45 \cdot T_{al} - 8.9, T_{eff18MY} = 0.42 \cdot T_{al} - 9.5. \quad (27b)$$

These equations are for winter months from Dec to Mar. The equations for spring (Apr-May) and late summer to freeze-up (Aug to Nov) are slightly different. For June and July relationships were not presented. Here, we approximate T_{al} with the ERA-Interim 2-m T_a . These relationships were based on year-round observations of sea ice temperature profiles at the Surface Heat Budget of the Arctic Ocean (SHEBA) ice camp in the Beaufort Sea in 1997-98. The physical temperature at the penetration depth of each AMSR-E frequency was assumed to be representative of T_{eff} (Mathew et al., 2009). Figure 9 shows T_{eff} 's from these two different estimation methods. The OSI SAF T_{eff} 's increase faster with increasing T_a than the Mathew et al. (2009) ones, and thus, the differences are

not constant. The differences between 18 and 36 GHz T_{eff} 's from (27a) and (27b) are very small. The MYI T_{eff} is always smaller than all OSI SAF T_{eff} 's, except at 36 GHz V-pol when $T_a < 255$ K. The OSI SAF T_{eff} 's are always larger when $T_a > 266$ K. The use of (27a) and (27b) requires some method (e.g. the NT SIC) for the FYI and MYI classification.

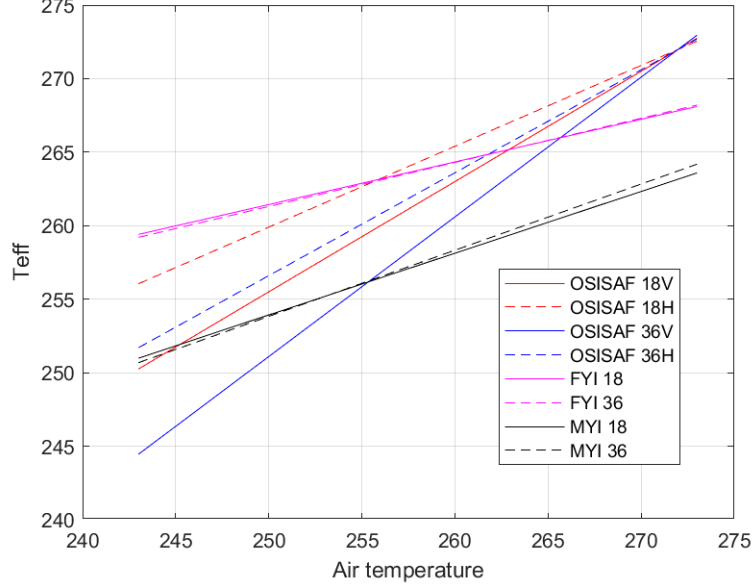


Figure 9. Sea ice effective temperatures with the OSI SAF relationships (19) and for FYI and MYI by Mathew et al. (2009).

6.2 Sea ice effective temperature from radiometer data

Recently, Kilic et al. (2019) presented T_{eff} estimation based on the snow-ice interface temperature (T_{si}) estimated either from T_{B6V} or T_{B610V} . T_{si} itself is a function of snow thickness (h_s) which is estimated from the T_{B6V} , T_{B18V} and T_{B36V} data. Linear relationships between T_{eff} and T_{si} were derived from MEMLS simulations, and when empirical T_{si} from the radiometer data is used then a bias between empirical and simulated T_{si} must be taken into account. This T_{eff} estimation method cannot be applied in the OSI-450 algorithm due to lack of T_{B6V} and T_{B10V} channels in the SSM/I and SSMIS radiometers, but it can be applied to the AMSR-E and AMSR2 data (OSI-408 product). Equations for the T_{eff} estimation are (Kilic et al., 2019):

$$h_s = 1.7701 + 0.0175 \cdot T_{B6V} - 0.0280 \cdot T_{B18V} + 0.0041 \cdot T_{B36V} \quad (28)$$

$$T_{si6V} = 1.086 \cdot T_{B6V} + 3.98 \cdot \ln(h_s) - 10.70 \quad (29a)$$

$$T_{si10V} = 1.078 \cdot T_{B10V} + 5.67 \cdot \ln(h_s) - 5.13 \quad (29b)$$

$$T_{eff18V}(T_{si10V}) = 0.920 \cdot (T_{si10V} - 3.97) + 21.5 \quad (30a)$$

$$T_{eff36V}(T_{si10V}) = 0.960 \cdot (T_{si10V} - 3.97) + 10.9 \quad (30b)$$

$$T_{eff18V}(T_{si6V}) = 0.920 \cdot (T_{si6V} - 4.01) + 21.5 \quad (30c)$$

$$T_{eff36V}(T_{si6V}) = 0.960 \cdot (T_{si6V} - 4.01) + 10.9 \quad (30d)$$

The T_{si} retrieval was tested only for MYI by Kilic et al. (2019), but they assumed it to be valid also for FYI as T_{B6V} and T_{B10V} have limited sensitivity to the ice type. T_{eff} equations were given only for the V-polarization, as T_B measurements are noisier at the H-polarization due to the variability of e_{si} . We assume that the T_{eff} estimates can be also applied at the H-polarization. T_{eff} 's for FYI and

MYI in (27a) and (27b) also do not have polarization dependence. The results by Kilic et al. (2019) do not clearly indicate whether T_{B6V} or T_{B10V} is better for the T_{eff} estimation. We use here T_{B10V} as it has better spatial resolution than T_{B6V} . The MEMLS data based relationship between T_{eff} and T_{si} has also slightly smaller RMSE with the T_{B10V} channel (Kilic et al., 2019). Here both T_{B6V} and T_{B10V} are gridded to 50 km pixel size, but later in operational applications it is possible use T_{B10V} (and higher frequency channels) in a finer grid (e.g. 25 or 30 km).

The estimation of h_s , T_{si} and T_{eff} is valid only over 100% concentration sea ice (Kilic et al., 2019). As T_B of open water is low even a small fraction of it in a pixel decreases the measured T_B 's considerably, leading to under estimation of the aforementioned parameters.

T_{si} from (29) shows that it increases with increasing h_s , and as h_s is typically larger for MYI than FYI then T_{si} could be larger for MYI, depending on T_{B6V} or T_{B10V} . Larger T_{si} for MYI was observed by Kilic et al. (2019) in their data analyses; areas with large h_s showed larger T_{si} in cold conditions (T_a between -30 and -20 °C) due to the thermal insulation effect of the snow layer, and T_{si} showed a high positive correlation with SIC_{MYI} . Kilic et al. (2019) suggested that the influence of higher h_s on MYI outbalances that of higher ice thickness on T_{si} . Larger T_{si} leads to also larger T_{eff} in (30). On the contrary, T_{eff} 's for FYI and MYI by Mathew et al. (2009) show larger T_{eff} for FYI, see Figure 9.

6.3 FYI and MYI emissivities with T_{eff} from T_a

For the estimation of the daily FYI and MYI e_a 's a dataset is collected in the following way: a) first for each pixel of an AMSR2 gridded swath dataset concentrations of FYI and MYI are determined with the NT SIC algorithm using the AMSR2 fixed tie points in (Tonboe and Pedersen, 2017). b) Next, pixels which have the total unconstrained $SIC_t > 90\%$ and SIC_{FYI} or SIC_{MYI} over 75% are find out (extension of the 90% total SIC curve outside the NT algorithm triangle):

$$\text{FYI pixels: } SIC_{FYI} \geq 0.75 \ \& \ SIC_t \geq 0.90 \quad (31a)$$

$$\text{MYI pixels: } SIC_{MYI} \geq 0.75 \ \& \ SIC_t \geq 0.90 \quad (31b)$$

The data selection by (31) allows a lot variation of the FYI and MYI $PR18$ and $GR3618V$ signatures around the fixed tie points, including MYI signatures with large negative $GR3618V$ and FYI with very small $PR18$. The AMSR2 tie points may not always match real FYI and MYI with 100% SIC present in each swath dataset. The open water fraction can be at maximum 0.25. The uncorrected SIC_t may have a negative FYI or MYI SIC component. c) ERA-Interim T_a is linearly interpolated to the acquisition time of each AMSR2 swath dataset, and selected FYI and MYI pixels are accompanied with T_a and also with the AMSR2 swath acquisition time. d) T_{eff} 's at the 18.7 and 36.5 GHz channels are calculated for FYI and MYI pixels with (27), and then e_a 's are derived with (26). e) T_B data at 18 and 36 GHz are also collected from the selected FYI and MYI pixels for further analyses (e.g. for the thin ice identification over FYI with (23)). f) Above steps are conducted for all AMSR2 swaths from Oct 2017 to May 2018, and data are collected for further analyses. The landmask is here dilated with a 3x3 block to exclude coastal pixels in the dataset, also the Baltic Sea and some areas where sea ice do not ever exist are excluded, see Figure 4. In addition, all e_a samples from a pixel are rejected if even one e_a sample is over one ($T_{eff} < T_B$). In case of FYI on average only 0.7% of e_a samples in each L1R swath dataset were excluded, and for MYI this figure was 0.2%. Larger rejection percentages, over 5%, occurred only in Apr-May. Only 3.9% of FYI pixels were detected with (23) as thin ice, and all with $GR3618H$. The requirement for $SIC_t \geq 0.90$ also filters out thin ice as now $PR18$ is always < 0.05 (this depends on the choice of the NT tie points). The total number of samples for FYI is nearly 7.76e6 and 1.70e6 for MYI.

The collected T_B data in the form of $PR18$ vs. $GR3618V$ density plot and the NT algorithm triangle are shown in Figure 10. For MYI there are some large negative $GR3618V$ signatures, like due thick snow cover, low density snow-ice layer (large volume scattering) or some other surface effect. Very small FYI $PR18$ signatures could represent highly deformed ice. The peak of the FYI data is very close to the NT FYI tie point, but for MYI the peak has larger $GR3618V$ and slightly smaller $PR18$ than the NT tie point. This likely shows that the used MYI tie point does not represent 100% SIC_{MYI} in this AMSR2 dataset.

Using the ± 7 days sliding time window, starting on 8 Oct 2017 and ending on 24 May 2018, e_a is estimated for FYI and MYI over the whole Arctic; i.e. daily e_a tie points for FYI and MYI are derived. In this estimation the maximum allowed T_a is set to -5°C to include data only from cold winter conditions and to exclude cases when snow cover on sea ice could be moist. This same T_a limit was used in the AMSR2 based thin ice detection in (Mäkynen and Similä, 2019). First, using the SIC_{FYI} and SIC_{MYI} data for the ± 7 seven days period SIC histograms with 10% SIC bin width are calculated; the bin centre is moved with 5% step, starting from 75%, and the SIC_{FYI} and SIC_{MYI} bins with the maximum number of samples are found out. The e_a samples belonging to these maximum SIC bins are taken to represent FYI and MYI with close 100% SIC. Thus, it is assumed that the NT may give a biased SIC estimate for a pixel covered fully by FYI or MYI, and that over the Arctic FYI and MYI pixels with close to 100% SIC are the most common ones.

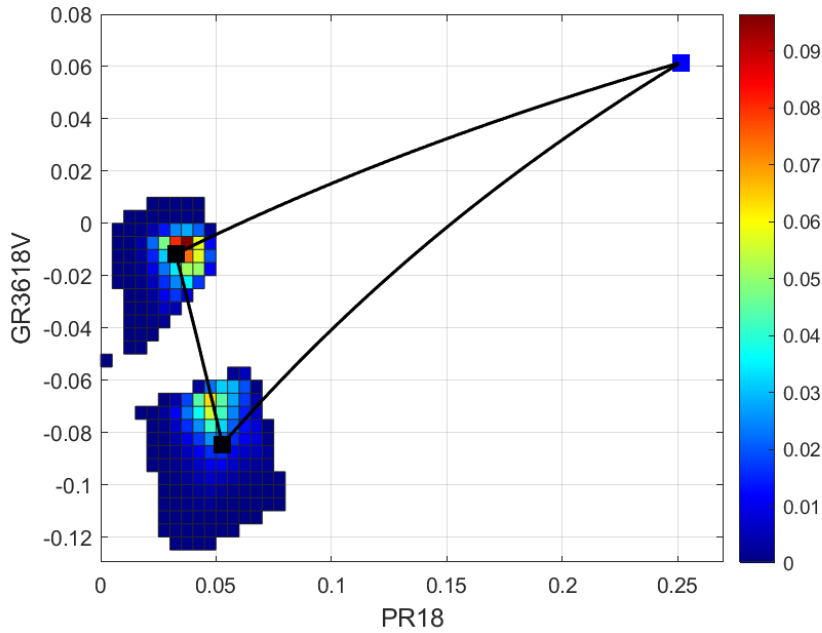


Figure 10. Collected FYI and MYI T_B data for the statistical apparent emissivity estimation in the NASA Team algorithm triangle. FYI and MYI 2-D density plots were calculated separately.

The number of e_a samples for FYI varies from $7.44\text{e}3$ to $2.26\text{e}5$, and the mean is $1.43\text{e}5$. For MYI these statistics are $5.82\text{e}3$, $6.20\text{e}4$, and $4.35\text{e}4$, respectively. The number of samples for FYI as a function of time up to end of Feb 2018 follows increase of the Arctic sea ice area, and after that it stays at rather constant level and before decreasing rapidly in May due to warming weather ($T_a > -5^\circ\text{C}$), see Figure 11. The number of samples for MYI shows increase during the freeze-up period (Oct-Nov), and then stays at a fixed level up to end of Apr. The number of MYI samples also decreases rapidly in May. For FYI the most common 10% wide SIC bins are those with the bin centres at 95% and 100%. For MYI the most common is the bin with the 80% centre SIC value.

The daily e_a tie point can be estimated as mean, modal or some percentile value from the selected e_a data. It is assumed that a small percentile, like 10%, represents case where the atmospheric influence is small on e_a , and thus, e_a is close to the true average e_{si} . This percentile is a best guess; a smaller one could include too much cases where e_a is mixture of open water and FYI or MYI. Similar approach was used by Miao et al. (2000) to estimate a surface signal contribution in the so-called R-factor $(\ln((T_{B37V} - T_{B37H})/(T_{B85V} - T_{B85H})))$ for studying cloud signatures over the Antarctic sea ice.

Daily FYI and MYI e_a 's estimated as the 10% percentile of the selected e_a data within ± 7 days window are shown in Figures 12 and 13 (e_a 's are with 0.01 resolution). The daily e_a 's at 18.7 and 36.5 GHz for FYI are quite close to the OSI SAF fixed emissivities, the maximum absolute difference is only 0.04, and the mean absolute differences are less than 0.013. However, the daily e_a show some temporal changes. Some of these changes are co-incident with the change of the SIC_{FYI} bin assumed to represent FYI with close 100% SIC, e.g. an e_a dip in March. The 18.7 and 36.5 GHz H-polarization e_a 's are mostly very close to each other. The OSI SAF emissivity difference between these channels is only 0.02. The daily MYI e_a at the 36.5 GHz are clearly smaller than the OSISAF tie point emissivities, the average difference is around 0.15. At the 18.7 GHz the difference is also noticeable, on average 0.05 at V-pol and 0.09 at H-pol. Compared to Mathew et al. (2009) average winter time MYI emissivities (25) the differences are very small at 18.7 GHz, and slightly larger at 36.5 GHz (max 0.04). The daily MYI e_a 's have only small temporal variation.

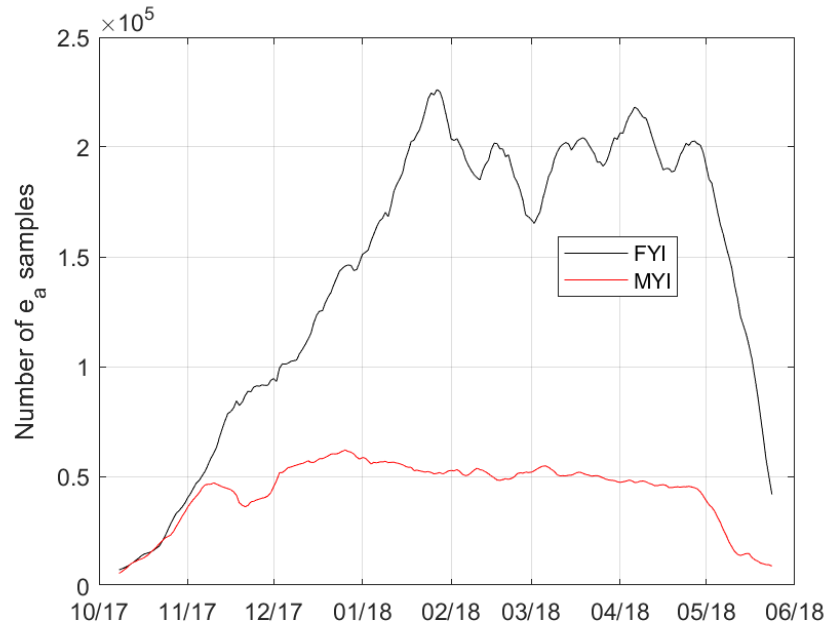


Figure 11. Number of apparent emissivity samples for FYI and MYI within ± 7 days sliding time window. Data collected over the Arctic area shown in Figure 4.

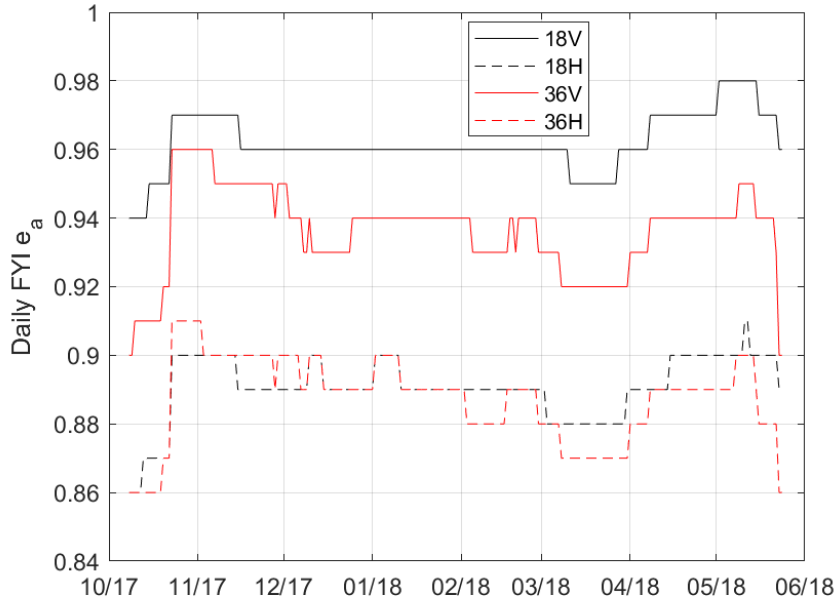


Figure 12. Estimated daily Arctic FYI apparent emissivities at 18.7 and 36.5 GHz for a time period from Oct 2017 to May 2018.

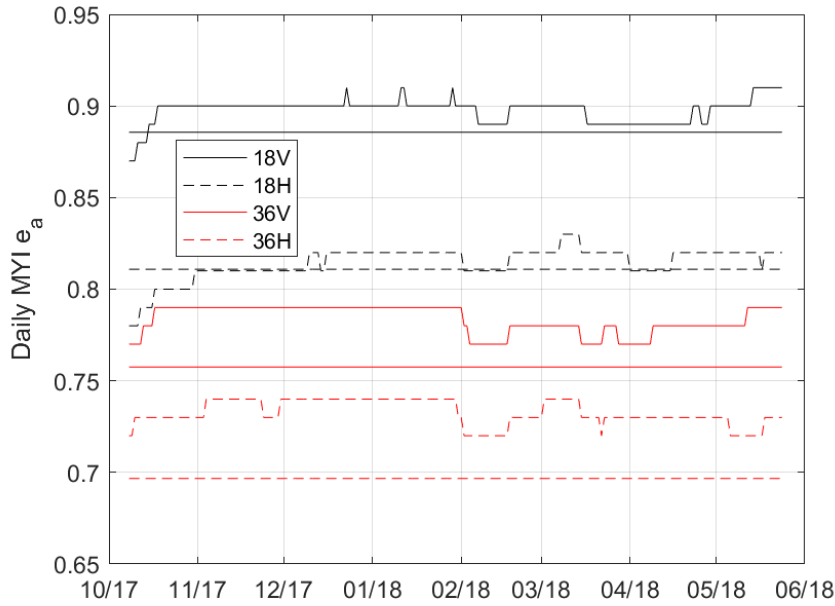


Figure 13. Estimated daily Arctic MYI apparent emissivities at 18.7 and 36.5 GHz for a time period from Oct 2017 to May 2018. The Mathew et al. (2009) winter time average MYI emissivities are also shown with straight lines.

6.3.1 Reference emissivities and T_{eff} 's for the winter season

In the above analysis daily e_a 's were determined within ± 7 days window. Next, we determine fixed reference e_a 's (e_{aref}) and T_{eff} 's (T_{effref}) for the winter season from Dec 2017 to Apr 2018. These are used in the calculation of T_{Bref} . e_{aref} 's are calculated as the daily e_a 's before, but using this time 5% SIC_{FYI} and SIC_{MYI} bins as much more e_a samples are now available. Next, T_{effref} is calculated as the mean value of T_{eff} when $e_a - 0.005 \leq e_{aref} \leq e_a + 0.005$ (0.01 wide bin). Also

reference air temperatures (T_{aref}) at each channel and for FYI and MYI are derived the same way. T_{aref} has effect on the upwelling and downwelling effective air temperatures (T_U and T_D) through a difference term $b_5\zeta(T_s - T_v)$, where T_s is approximated with T_a ; see equations (25) and (26) in (Wentz and Meissner, 2000). Table 3 lists e_{aref} , T_{effref} and T_{aref} for the 18.7 and 36.5 GHz channels. For FYI e_{aref} 's are very close to the OSI SAF emissivities in Table 1; differences are only 0.01.

Table 3. Reference emissivities and sea ice effective temperatures determined for the AMSR2 radiometer data acquired during the winter season from Dec 2017 to Apr 2018.

Parameter	Ice type	18.7V	18.7H	36.5V	36.5H
e_{aref}	FYI	0.96	0.89	0.94	0.89
T_{effref}		261	262	261	262
T_{aref}		250	252	251	251
e_{aref}	MYI	0.90	0.82	0.79	0.74
T_{effref}		255	255	255	255
T_{aref}		252	253	252	252

6.4 FYI and MYI emissivities with T_{eff} from the AMSR2 data

The T_{eff} 's in (30) by (Kilic et al., 2019) can be also used to calculate e_a 's with (26). For T_{Bnwp} daily e_a 's are again determined using the data from the ± 7 days sliding window and with the same method as above. However, calculation of the T_{eff} with (28)-(30) can yield erroneous data as in principle SIC have to be 100% for the equations to be valid. In case of the Arctic pack ice which is the target in the SIC noise reduction it is assumed that this 100% SIC condition is roughly fulfilled. For the whole Arctic Ocean we will investigate if high correlation exists between T_{eff} and T_a allowing T_{eff} estimation when $SIC_{FYI} < 100\%$ or $SIC_{MYI} < 100\%$.

This study is conducted with the AMSR2 L1R gridded to 50 km pixel size. For FYI pixels selected with (31a) thin ice was detected (again with only *GR3618H*) only for 0.5% of the pixels. This time there was on average 72% FYI e_a samples over one ($T_{eff} < T_B$) in each swath dataset. These samples were rejected. This shows that T_{eff} for FYI is typically underestimated with (28)-(30). If T_{eff} is estimated from T_{B6V} and T_{Si6V} then the average e_a sample rejection percentage is even higher, 82%. For MYI only 0.2% of the e_a samples were on average rejected in each swath. The total number of e_a samples for FYI is now nearly 5.46e5 and 4.22e5 for MYI.

The number of daily e_a samples for FYI (± 7 days window) in the most common 10% wide SIC bin varies from 1395 to 3.74e4, and the mean is 1.42e4. For MYI these statistics are 1334, 15780, and 10958, respectively. For FYI the number of samples in March 2018 is around two times larger than in Feb and in Apr which shows T_{eff} estimate being better in March (FYI extent does not change much within these months). For both FYI and MYI the most common 10% wide SIC bin is that with the bin centre at 80%. In the NT algorithm triangle the collected T_B data has a peak slightly below and right of the FYI tie point (not shown). It seems that a change from 25 km to 50 km gridded T_B data has an effect on the NT SIC estimation; the 50 km data has more spatial averaging which likely reduced the number of high SIC estimates.

Estimated daily FYI and MYI e_a 's are shown in Figures 14 and 15 (e_a 's are with 0.01 resolution). The e_a 's at 18.7 and 36.5 GHz for FYI are again close to the OSI SAF fixed emissivities, the

maximum absolute difference is only 0.03, and the mean absolute differences are less than 0.024. Compared to Figure 12 there are some differences, e.g. e_a at 18.7 GHz H-pol is now larger than at 36.5 GHz H-pol. The MYI e_a 's here are on average slightly larger (0.01 or 0.02) than those in Figure 13, and thus are also the differences to Mathew et al. (2009) average winter time MYI e_{si} 's (25). Difference to the OSISAF tie point e_{si} 's are again noticeable. The temporal variation of the MYI e_a 's is also here small.

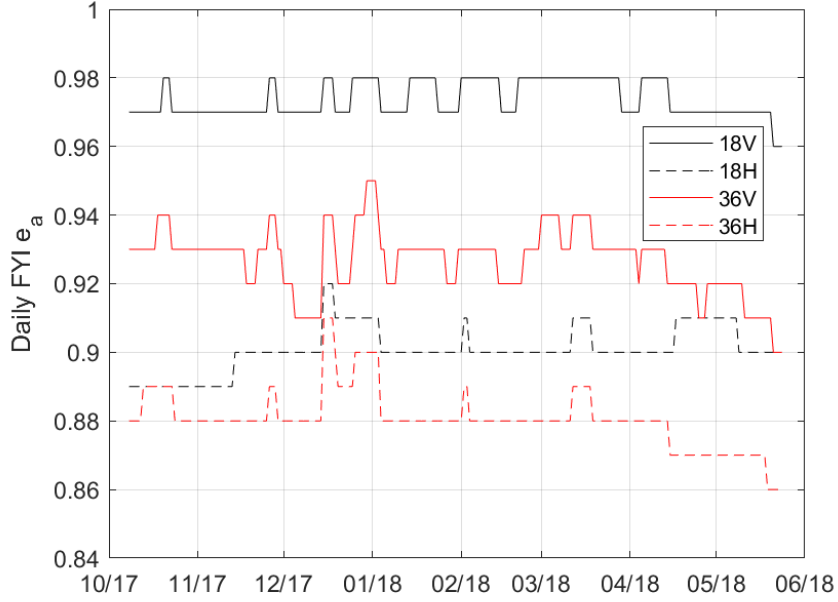


Figure 14. Estimated daily Arctic FYI apparent emissivities at 18.7 and 36.5 GHz for a time period from Oct 2017 to May 2018. T_{eff} was calculated from the T_B data (Kilic et al., 2019).

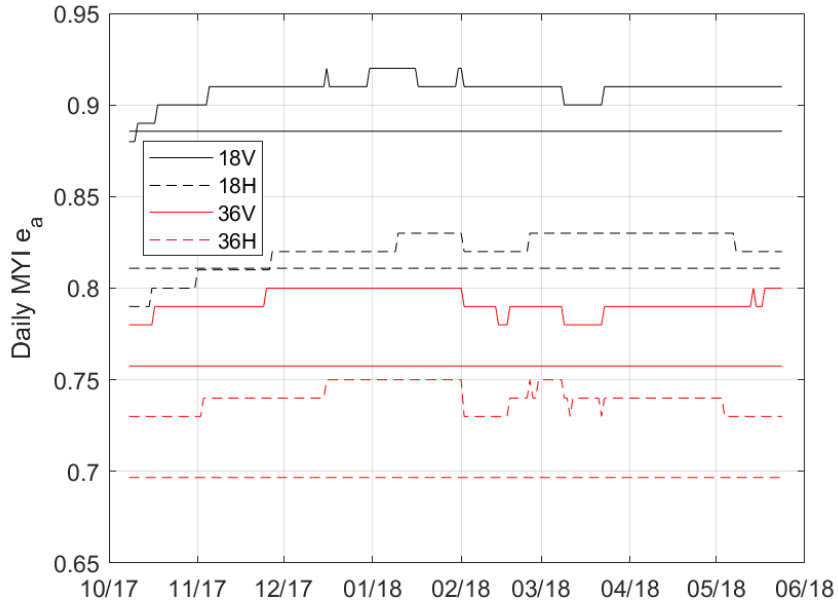


Figure 15. Estimated daily Arctic MYI apparent emissivities at 18.7 and 36.5 GHz for a time period from Oct 2017 to May 2018. Mathew et al. (2009) winter time average MYI emissivities are also shown with straight lines. T_{eff} was calculated from the T_B data (Kilic et al., 2019).

6.4.1 Reference emissivities and T_{eff} 's for the winter season

For the T_{Bref} term in the T_B correction e_{aref} 's and T_{effref} 's were derived as in Section 6.3.1. The results are in Table 4. e_{aref} 's are very close to those in Table 1, max absolute difference is only 0.02. A noticeable difference to Table 3 is smaller T_{effref} (6 or 8 K) for FYI here. Kilic et al. (2019) developed T_{si} and T_{eff} estimation using data for MYI, and it is possible that T_{eff} for FYI, at least for thin FYI (<0.5-1 m) is too cold. This would explain the rejection of large amount of FYI e_a samples ($e_a > 1$) in Section 6.4.

Table 4. Reference emissivities and sea ice effective temperatures determined for the AMSR2 radiometer data acquired during the winter season from Dec 2017 to Apr 2018. T_{eff} was calculated from the T_B data using equations by Kilic et al. (2019).

	Ice type	18.7V	18.7H	36.5V	36.5H
e_{aref}	FYI	0.97	0.90	0.92	0.87
T_{effref}		255	254	255	256
T_{aref}		252	253	252	253
e_{aref}	MYI	0.91	0.83	0.80	0.75
T_{effref}		251	254	252	252
T_{aref}		252	253	252	252

6.4.2 Correlation between T_{eff} and T_a

Estimation of T_{eff} with (28)-(30) is only valid for the Arctic MYI and FYI (thin ice excluded) with 100% SIC. Even a small fraction of open water decreases the measured T_B 's, and further T_{eff} . For pixels with $SIC_{FYI} < 100\%$ and/or $SIC_{MYI} < 100\%$ the sea ice contribution in the measured T_B could be estimated if the open water T_B is known through RTM modelling. This approach may not be plausible due to atmospheric effects and difficulties in modelling accurately ocean surface emissivity (ocean roughness due to wind). A practical approximate solution would be to use the ocean T_B tie points here, or to estimate T_{eff} from T_a , if they have strong correlation.

For FYI the correlation between T_{eff} at 18.7 or 36.5 GHz and T_a is quite high, 0.82. T_{eff} at these two frequencies are perfectly correlated as they both are linear functions of T_{si} . Unfortunately, the scatter between T_{eff} and T_a is large, and RMSD between T_{eff} from (28)-(30) and T_{eff} predicted from T_a through linear regression is 1.9 K. For MYI the T_{eff} vs. T_a correlation is only 0.43, and RMSD for the predicted T_{eff} is 2.7 K. It is concluded that estimation of T_{eff} (based on T_B 's) from only T_a is too inaccurate for the atmospheric correction, and therefore, T_{eff} with (28)-(30) is only valid for FYI and MYI with SIC very close to 100%.

7 Effect of New Sea Ice Emissivities and Effective Temperatures in the T_B Atmospheric Correction

In the new T_B atmospheric correction e_{si} 's, T_{eff} 's, their reference values and T_{aref} for FYI and MYI are combined to common pixel-wise parameters as:

$$X = \frac{SIC_{FYI}}{SIC_{FYI} + SIC_{MYI}} X_{FYI} + \frac{SIC_{MYI}}{SIC_{FYI} + SIC_{MYI}} X_{MYI} \quad (32)$$

Both T_{Bnwp} and T_{Bref} are calculated with these combined parameters (reference values in T_{Bref}). In (32) SIC_{FYI} and SIC_{MYI} with the NT algorithm are constrained to 0% to 100% interval, but their sum can be over 100%. The total SIC (SIC_t) used in the calculation of T_{Bnwp} and T_{Bref} is also constrained from 0% to 100%. Open water filter in (13) is applied to all three SIC parameters. When SIC_t is very small, below 30%, then parameters for FYI are used directly. Significant SIC_{MYI} values are also observed over predominantly seasonal sea ice areas (like Kara Sea). These likely represent FYI with signatures resembling those of MYI due to thick snow cover, snow-ice layer on the ice surface, deformation, etc. Low values (<30%) of SIC_{FYI} and SIC_{MYI} are likely not very accurate due to the fixed tie points used. Unfortunately, the fixed tie points in the NT algorithm do not always yield good SIC estimates, e.g. in March 2018 in the Kara Sea SIC_{FYI} is too low (should be very close 100%). Figures 16 and 17 show examples 36.5 GHz V-pol e_a and T_{eff} maps for the T_{Bnwp} calculation. The T_{eff} maps have spatial variations due to T_a , SIC_{FYI} and SIC_{MYI} changes, but e_{si} maps only from SIC_{FYI} and SIC_{MYI} .

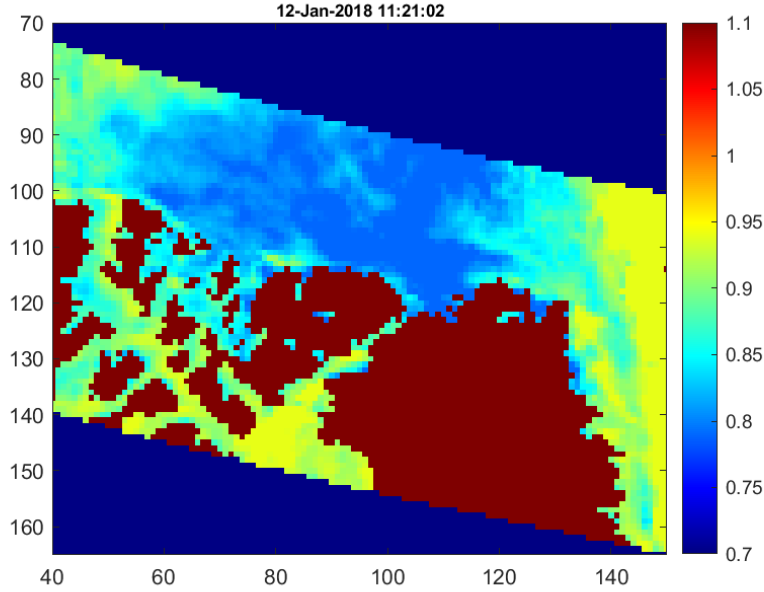


Figure 16. An example of apparent sea ice emissivity at 36.5 GHz V-polarization for the T_{Bnwp} term in the T_B atmospheric correction. Note that over open ocean FYI emissivity has been applied. T_{eff} for FYI and MYI was calculated with (27) (Mathew et al., 2009).

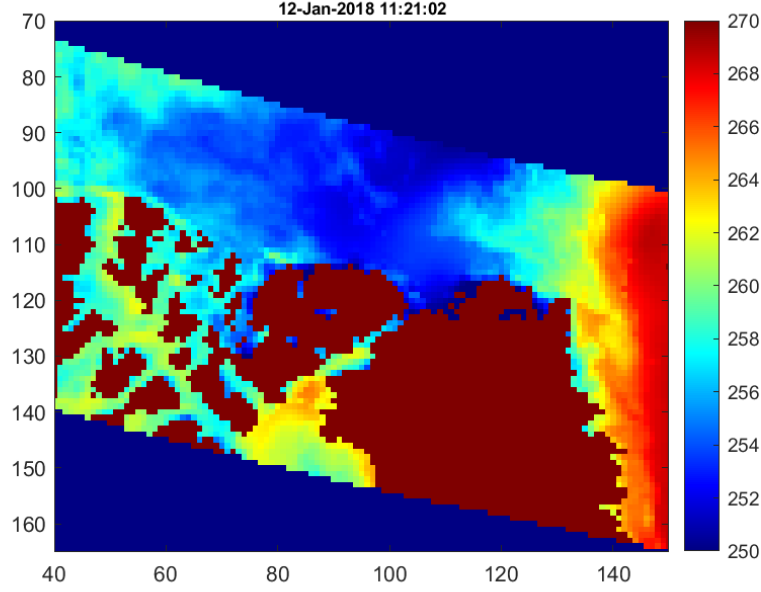


Figure 17. An example of sea ice effective temperature at 36.5 GHz for the T_{Bnwp} term in the T_B atmospheric correction. Note that over open ocean FYI T_{eff} has been applied. T_{eff} for FYI and MYI was calculated with (27) (Mathew et al., 2009).

The effects of the new e_{si} 's and T_{eff} 's, and their winter season reference values, to the T_B atmospheric correction is investigated by comparing statistics (mean and STD) of $\Delta T_{Bc} = (T_{Bnwp} - T_{Bref})$ over three test sites north of the Canadian Arctic and Greenland, see Figure 18. The size of the test sites is 15 by 15 pixels (25 km grid). Here ΔT_{Bc}^d (d=default) denotes ΔT_{Bc} with the OSI-450 method, and ΔT_{Bc}^n with the new parametrizations. The means and STDs are calculated only when a swath dataset covers fully a test site.

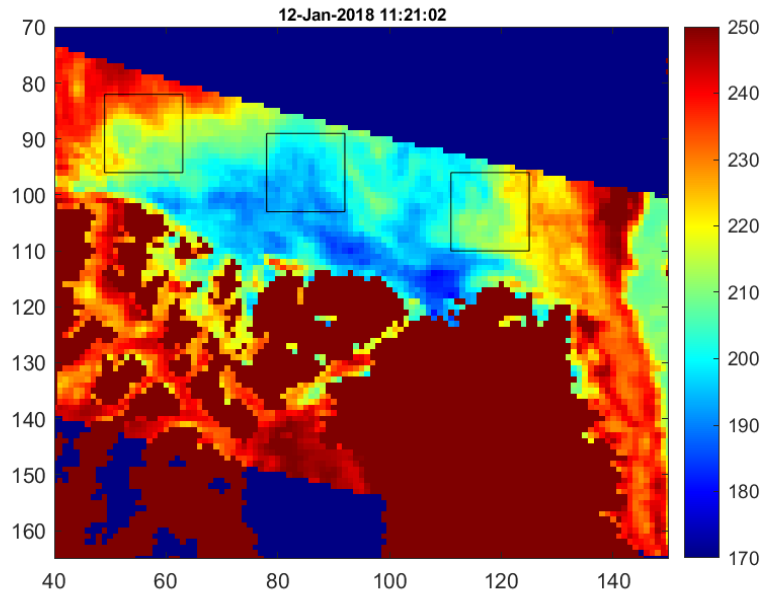


Figure 18. An AMSR2 36.5 GHz V-polarization T_B swath dataset after atmospheric correction with new sea ice emissivities and T_{eff} 's. Black rectangle areas are used in studying the effect of new formulations in the T_B atmospheric correction and SIC retrieval. Pixel size is 25 km.

7.1 FYI and MYI emissivities with T_{eff} from T_a

Figure 19 shows ΔT_{Bc}^d and ΔT_{Bc}^n at the 36.5 GHz H-pol and their difference as a function of time for the test site on the right (denoted as test site 1) in Figure 18. The absolute ΔT_{Bc}^n is typically larger (up to 5 K) than ΔT_{Bc}^d , and it also has much larger temporal variation. These differences come from the new e_a 's and T_{eff} definitions, and their reference values in ΔT_{Bc}^n . The correction for WV is the same in ΔT_{Bc}^d and ΔT_{Bc}^n . Mean ΔT_{Bc}^n has high correlation, 0.84, with the mean T_a , and their temporal variations match each other. This shows that ΔT_{Bc}^n is mainly determined by T_{eff} and T_{effref} . The channel-wise e_a 's maps for T_{Bnwp} and T_{Bref} are close to each other, e.g. at 36.5 GHz H-pol the max difference between e_a and e_{aref} is around 0.02. ΔT_{Bc}^n and ΔT_{Bc}^d for the test site 1 at all three SIC input channels are shown in Figure 20. ΔT_{Bc}^d is the largest for the 36.5 GHz H-pol, and the smallest for the 18.7 GHz V-pol. For ΔT_{Bc}^n no clear frequency dependence is present. ΔT_{Bc}^n can be negative (corrected T_B is larger than the original T_B); especially in cold conditions, but ΔT_{Bc}^d is always positive. Std of ΔT_{Bc}^n for the test site 1 shows more temporal variation than that of ΔT_{Bc}^d , and it is always larger (not shown). This is due to spatial variation between T_{eff} (or e_a) and T_{effref} (e_{aref}) which is not present in ΔT_{Bc}^d .

For the other two test sites similar behaviours between ΔT_{Bc}^d and ΔT_{Bc}^n are observed. The correlation between ΔT_{Bc}^n and T_a is the highest at 18.7 GHz V-pol, from 0.86 to 0.93, and the lowest at 36.5 GHz H-pol, from 0.68 to 0.84.

In summary, ΔT_{Bc}^n with the new FYI and MYI e_a 's and T_{eff} 's has typically much larger absolute value than the OSI-450 ΔT_{Bc}^d , and it also has larger temporal variation. ΔT_{Bc}^n may also be negative (i.e. correction increases T_B), but ΔT_{Bc}^d is always positive. ΔT_{Bc}^d corrects only for the total water vapour as T_{eff} and T_{effref} are equal; they are calculated from the same T_a data. Likewise also e_a and e_{aref} are equal. In the new correction scheme T_{eff} and T_{effref} are different, and thus, a change in T_{eff} is in principle corrected. Also is the e_a change related to winter season e_{aref} corrected. However, it is possible that estimation of T_{eff} and T_{effref} from T_a data has too large inaccuracies.

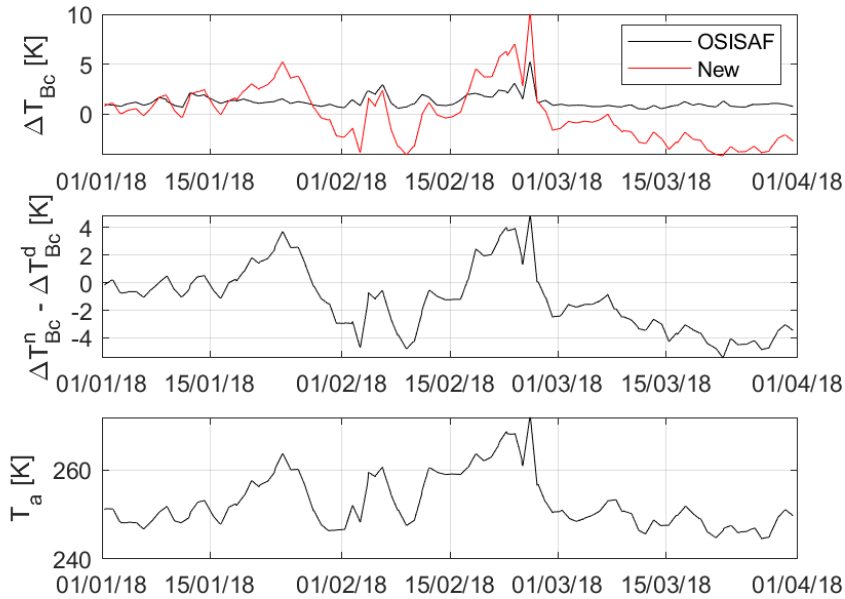


Figure 19. The mean T_B correction terms ($\Delta T_{Bc} = (T_{Bnwp} - T_{Bref})$) at the 36.5 GHz H-polarization for the rightmost test site in Figure 18 calculated with the OSI-450 method and with new definitions of sea ice emissivities and T_{eff} 's and their reference values.

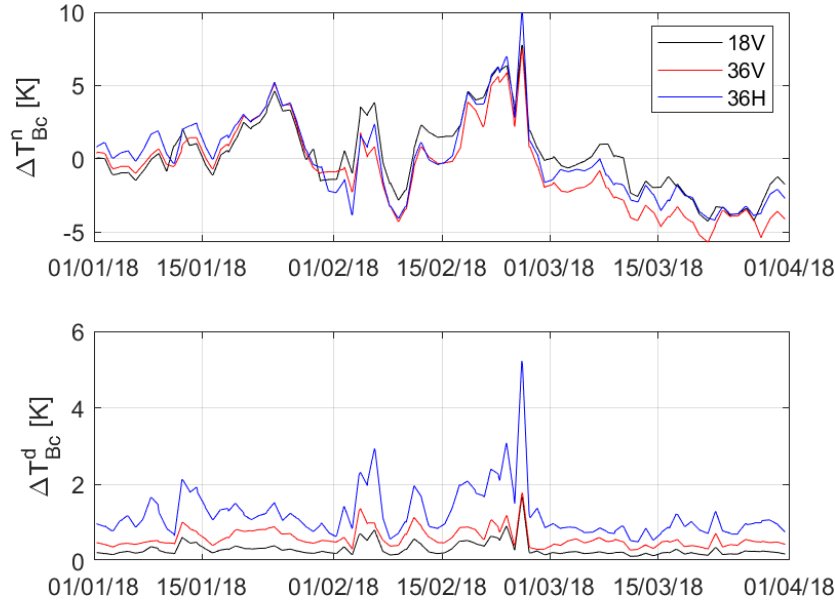


Figure 20. Mean ΔT_{Bc}^d and ΔT_{Bc}^n for the rightmost test site in Figure 18.

7.2 FYI and MYI emissivities with T_{eff} from the AMSR2 data

For comparison between ΔT_{Bc}^d and ΔT_{Bc}^n the same three test sites in Figure 18 are used, but now their size is 7 by 7 pixels (change from 25 to 50 km grid). T_{Bc}^n is now based on T_{eff} estimated from the T_B data with (28)-(30) (Kilic et al., 2019). Figure 21 shows ΔT_{Bc}^d and ΔT_{Bc}^n at the 36.5 GHz H-pol for the test site 1; compare to Figure 19. Also here the absolute value of ΔT_{Bc}^n is typically larger (up to 4 K) than ΔT_{Bc}^d , and it is also has much larger temporal variation. ΔT_{Bc}^n and ΔT_{Bc}^d for the test site 1 at all three SIC input channels are shown in Figure 22. Here the frequency dependence of ΔT_{Bc}^n is clearer than in Figure 20; ΔT_{Bc}^n mostly is the largest at 18.7 GHz V-pol. This is also observed for the two other test sites. The correlations between ΔT_{Bc}^n and T_a are here clearly smaller as T_{eff} was not derived from T_a . Now ΔT_{Bc}^n has spatial variation in pixel scale, whereas ΔT_{Bc}^n in Section 7.1 follows spatial variation of the ERA-Interim T_a .

In general, ΔT_{Bc}^n 's here and those in Section 7.1 are somewhat different. Their differences are not investigated here further as more interesting is too see differences in resulting SICs.

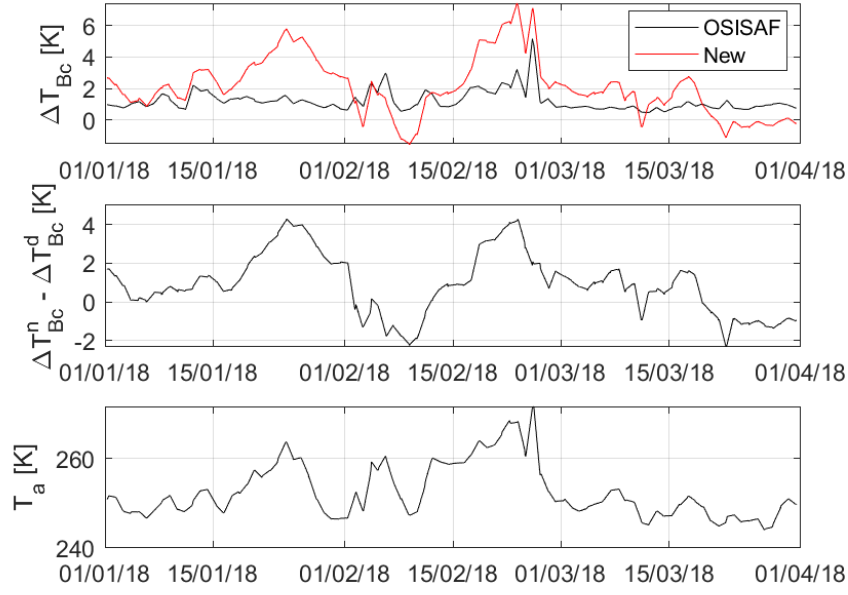


Figure 21. The mean T_B correction terms ($\Delta T_{Bc} = (T_{Bnwp} - T_{Bref})$) at the 36.5 GHz H-polarization for the rightmost test site in Figure 18 calculated with the OSI-450 method and with new definitions of sea ice emissivities and T_{eff} 's and their reference values. T_{eff} was calculated from the T_B data (Kilic et al., 2019).

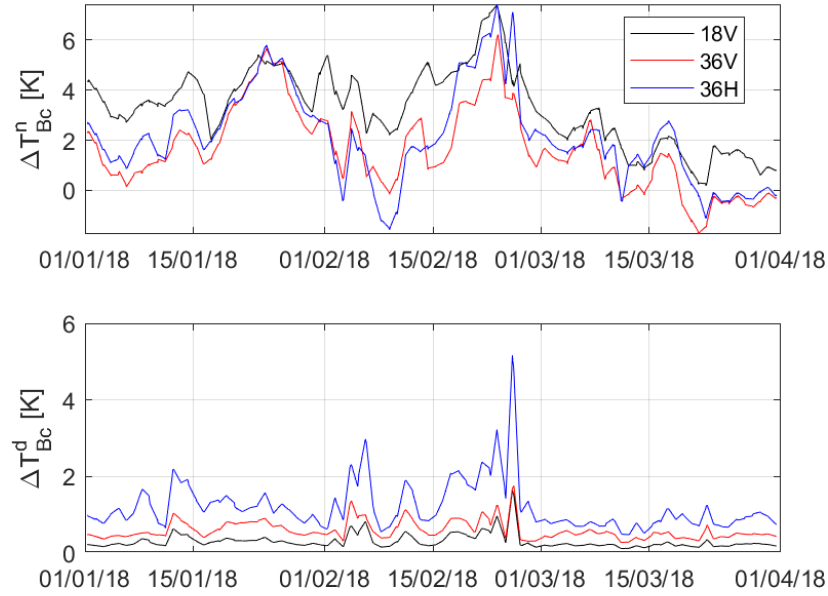


Figure 22. Mean ΔT_{Bc}^d and ΔT_{Bc}^n for the rightmost test site in Figure 18. T_{eff} was calculated from the T_B data (Kilic et al., 2019).

8 Dynamic Tuning of SIC Algorithms

The OSI-450 SIC algorithm was described in Section 4.2. It consists of two different SIC equations; B_{OW} which has the best accuracy for open water and B_{CI} having the best accuracy in high SIC conditions, and their combination for the final SIC (Lavergne et al., 2019a, 2019b), see (7) and (9). B_{OW} and B_{CI} are characterized with α and β parameters and the unit vector v , see (9). The v vector is perpendicular to the unit vector u at rotation angle θ . The u vector is along the so-called ‘ice line’ and it is in the direction of highest variance in the CI samples (determined with PCA). Large scale regional SIC biases observed in wintertime over high SIC areas with B_{CI} are compensated in the 2nd iteration (see Figure 5) using an empirical ‘curved’ ice line.

The dynamic tuning of the B_{OW} and B_{CI} algorithms for each day is conducted using CI and OW samples from ± 7 days sliding window (Lavergne et al., 2019b). This tuning of B_{OW} and B_{CI} is conducted two times; first with the original data and then with corrected T_B data, see Figure 5. The CI samples are collected from T_B swath datasets, and their locations (i.e. pixels) are determined with the NT SIC algorithm applied on the original T_B swath data; total SIC must be $>95\%$. Thus, same CI samples are used for the OSI-450 default SIC algorithms (25 km and 50 km grids) and for those with the new atmospheric correction. This is also the case for the OW samples. For the SIC algorithms with the new atmospheric correction thin ice samples were (partially) excluded from the CI sample set with (23). For the T_B data in 25 km grid on average only 1.5% of daily CI samples (± 7 days window) were detected as thin ice, but the daily percentage was sometimes over 10% in autumn and late winter (in May).

The four different OSI-450 SIC algorithms are denoted here as: SIC_{25}^d and SIC_{50}^d are the default algorithms in the 25 and 50 km grids, SIC_{25}^n (25 km grid) has new atmospheric correction (and new FYI and MYI emissivities) with T_{eff} calculated with (27) (Mathew et al., 2009), and SIC_{50}^n (50 km grid) has new atmospheric correction with T_{eff} calculated from the T_B data with (28)-(30) (Kilic et al., 2019). These algorithms are here compared to each other using two parameters: STD of SIC (σ_{SIC}), and uncertainty of a single B_{CI} observation which is B_{CI} sensitivity to small random-like T_B changes. σ_{SIC} ’s are calculated with the OW and CI sample datasets for which we assume true SIC to be close to 0% and 100%, respectively. The B_{CI} uncertainty is estimated with the propagation of error method on (9). For comparison σ_{SIC} with the CI dataset is also calculated for each algorithm without the curved ice line correction. The response of B_{CI} to mixtures of different sea ice types is also very important. In wintertime (dry snow, no melt ponds) B_{CI} should always give 100% SIC for these mixtures, but in reality SIC underestimation occurs over thin ice in various SIC algorithms, e.g. (Ivanova et al., 2015). Here an artificial mixture of thin ice and FYI is constructed using tie point signatures available from the combined MODIS – AMSR2 thin ice data, and SIC with the mixed T_B ’s is calculated. Finally, we also look into temporal behaviour of the rotation angle θ in the different SIC algorithms.

The time span in these comparisons in Sections 8.1 (25 km data) and 8.2 (50 km) is from 15 Oct 2017 to 17 May 2018 (corrected T_B data is 14 days longer). In Section 8.3 further SIC algorithm tuning experiments are conducted, especially using different 3-D combinations of 18 and 36 GHz T_B ’s and their sums and differences for the SIC retrieval. Later in Section 9, also SIC values and time series by different algorithms are compared.

8.1 SIC algorithms at 25 km grid

The number of daily CI samples (± 7 days window) in the 25 km pixel datasets followed temporal behaviour of the FYI e_a samples in Figure 11. The mean number of samples is $6.70e5$ for the CI dataset, and $9.20e4$ for the OW dataset. In the determination of the u vector with PCA the first principal component explained always over 97.9% the total variance.

Figure 23 shows an example of σ_{SIC} for B_{OW} and B_{CI} as a function of the rotation angle (θ) from -90° to $+90^\circ$. This figure can be compared to Figure 4(b) in (Lavergne et al., 2019b). The 0° reference for θ is the $T_{B18V} - T_{B36V}$ plane. For B_{CI} the change of σ_{SIC} is more gradual than for B_{OW} . It is also more gradual than in (Lavergne et al., 2019b). This is likely from different datasets used, but unfortunately the dynamic tuning process is not explained with all details by Lavergne et al. (2019b), and thus, the difference may also be due to some differences in the tuning.

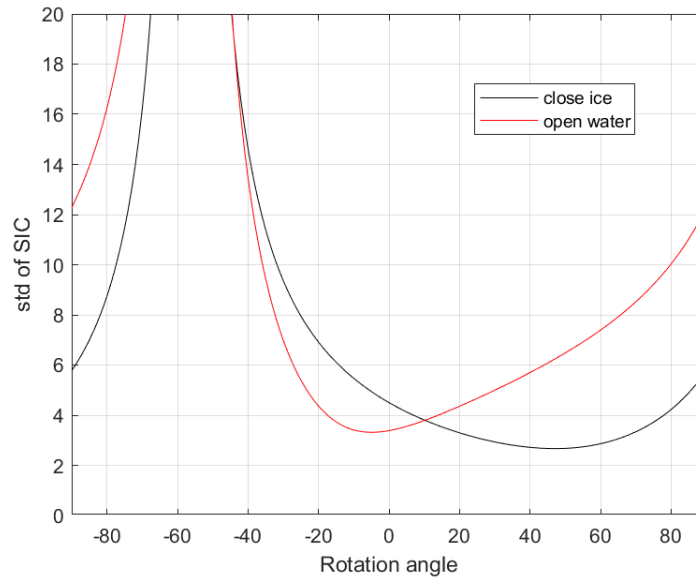


Figure 23. The standard of deviation of SIC in the dynamic tuning of B_{OW} and B_{CI} for SIC_{25}^d using daily CI and OW datasets for 12 Jan 2018. Here the minimum STD of SIC for B_{OW} and B_{CI} has the rotation angle of -5° and $+47^\circ$, respectively.

An example of the curved ice lines is shown in Figure 24. Here the scatter of B_{CI} values is quite large, from 85% to 110%, but the mean B_{CI} within 10 K wide DAL bins varies only from 99.0% to 102.8%. The fitted 4th degree polynomial follows nicely the mean B_{CI} curve. This was typically case at each day for all four SIC algorithms.

The σ_{SIC} 's with the CI dataset with and without the curved ice line correction for SIC_{25}^d are depicted in Figure 25. The curved ice line correction decreases σ_{SIC} slightly every day; max decrease is 0.25% and the mean is 0.11%. For SIC_{25}^n σ_{SIC} is also always smaller with the curved ice line (not shown); the mean improvement is 0.12%. The temporal variation of $\Delta\sigma_{SIC}$ is similar as for SIC_{25}^d .

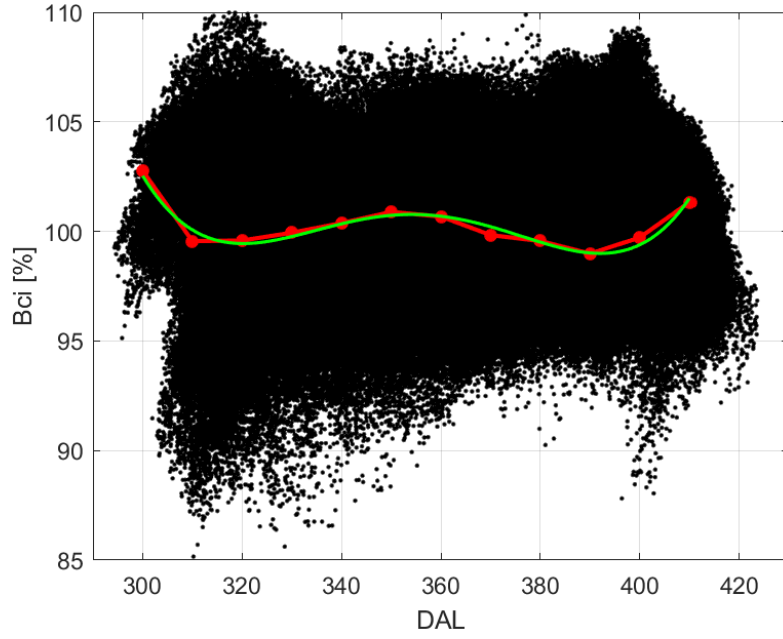


Figure 24. Scatterplot between DAL and B_{CI} in the CI dataset (T_B atmospheric correction applied) on 12 Apr 2018 for the default OSI-450 algorithm. Red curve shows the mean B_{CI} within 10 K wide DAL bins, and the green curve is the 4th degree fitted polynomial. The green curve is used in the correction of B_{CI} values.

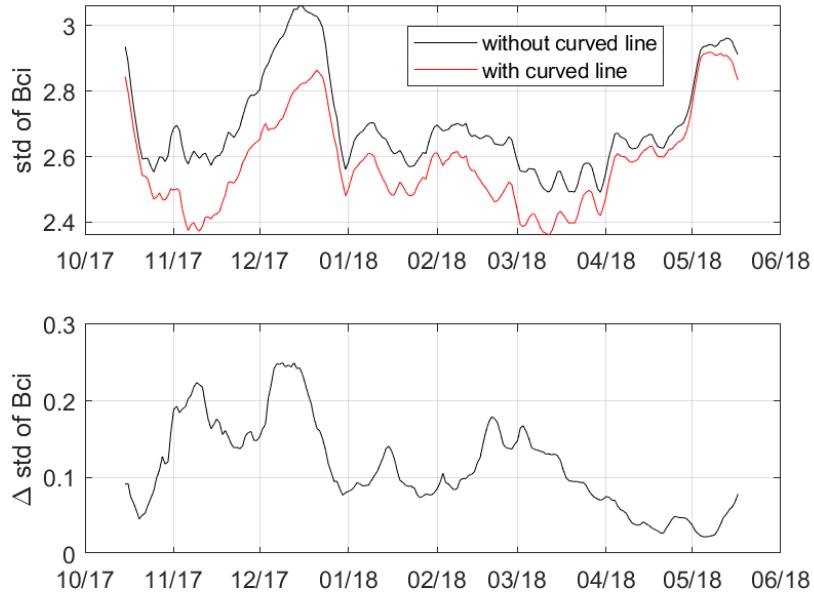


Figure 25. Daily standard deviation of SIC for SIC_{25}^d (default SIC) with the CI dataset when B_{CI} was calculated with and without the curved ice line correction.

The σ_{SIC} 's with the CI and OW samples for the SIC_{25}^d and SIC_{25}^n algorithms having the curved line correction are shown in Figure 26. σ_{SIC} with the CI sample is typically slightly larger for SIC_{25}^n (max difference around 0.4%, and max relative difference +14%), and thus, the new T_B atmospheric correction does not seem to increase the accuracy of SIC calculated with the CI dataset. For the OW case σ_{SIC} is also slightly larger for SIC_{25}^n (max around 0.2%), but the difference is now smaller. σ_{SIC} for the CI dataset is typically somewhat larger than for the OW dataset, but it has less temporal

variation. The average σ_{SIC} 's are the following: 2.6% and 2.3% for SIC_{25}^d with the CI and OW datasets, and 2.7% and 2.4% for SIC_{25}^n . Thus, the differences between these averages are very small.

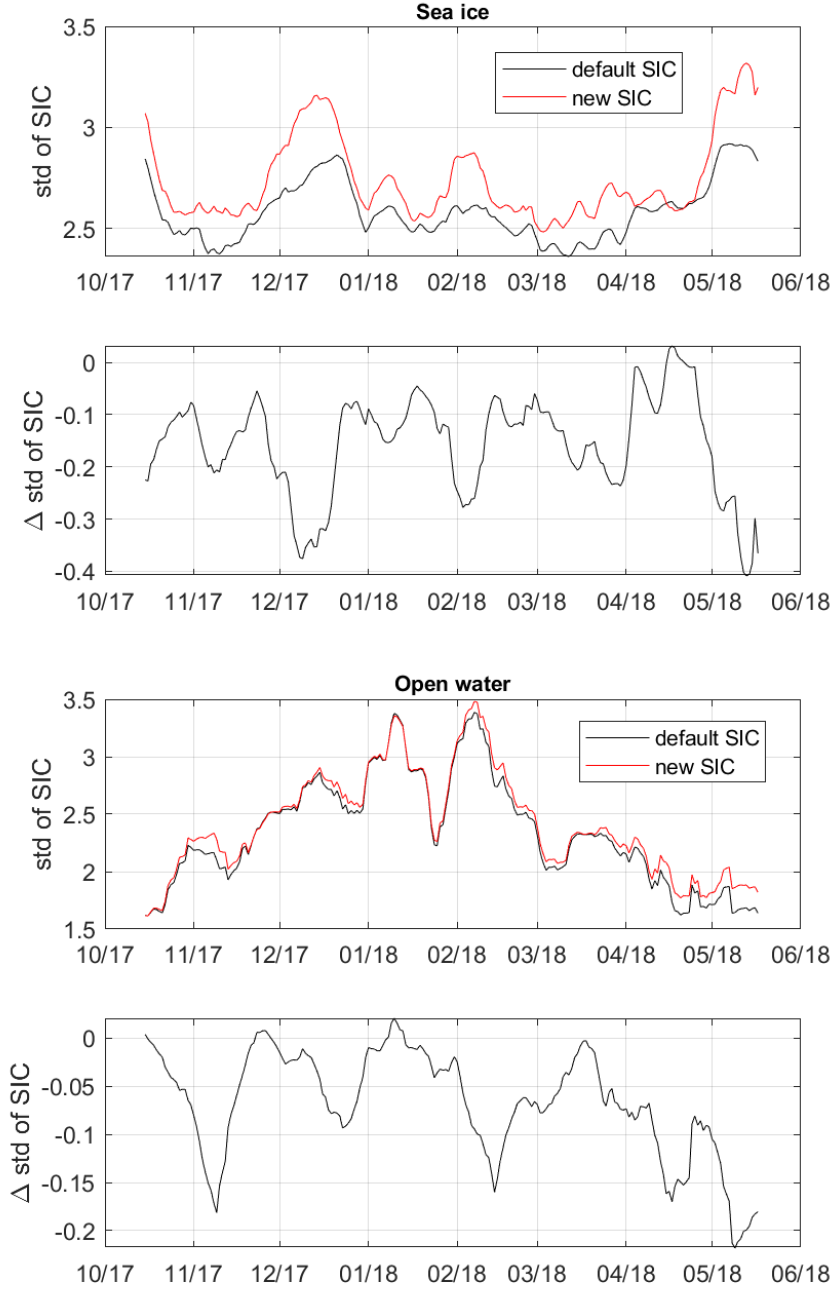


Figure 26. Daily standard deviation of SIC for the SIC_{25}^d (default SIC) and SIC_{25}^n (new SIC) algorithms tuned with the CI and OW datasets. The curved ice line correction was used for B_{CI} .

The rotation angles for B_{OW} and B_{CI} of SIC_{25}^d and SIC_{25}^n as a function time are shown in Figure 27. The angles for SIC_{25}^d and SIC_{25}^n are quite close to each other and show similar temporal behaviour. The angles for B_{OW} and B_{CI} are clearly different; the first one is between -10° and 0° , and the second between $+30^\circ$ and $+60^\circ$. The angle for B_{CI} has a decreasing trend as function of time. This is likely related to evolution of sea ice properties, but further studies would be needed here.

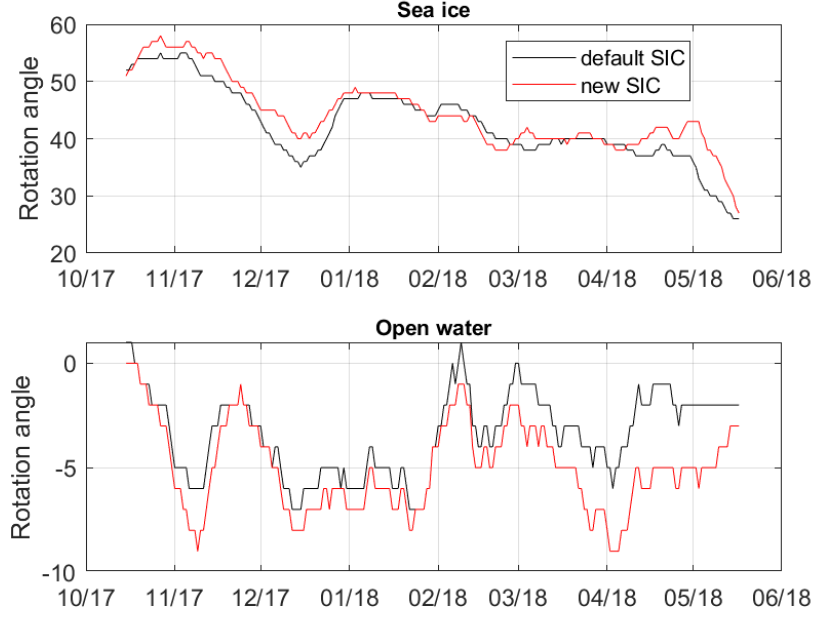


Figure 27. Daily rotation angles of B_{OW} and B_{CI} for the SIC_{25}^d (default SIC) and SIC_{25}^n (new SIC) algorithms tuned with the CI and OW sample datasets.

The sensitivity of B_{CI} to small changes of T_B 's (i.e. uncertainty) is estimated with the propagation of error method on (9). In the following equation channels T_{B18V} , T_{B36V} and T_{B36H} are denoted as 1, 2 and 3:

$$\Delta B_{CI} \approx |\alpha| \sqrt{(v_x \sigma_1)^2 + (v_y \sigma_2)^2 + (v_z \sigma_3)^2 + 2v_x v_y \sigma_{12} + 2v_x v_z \sigma_{13} + 2v_y v_z \sigma_{23}} \quad (32)$$

The covariance matrix is estimated from the daily CI dataset, and it is scaled with an estimated typical variance of T_{B36V} which represents typical variation due to radiometer sensor noise and small temporal and spatial changes of sea ice and snow cover properties. The reference T_B channel could be also other than T_{B36V} . The radiometric resolution of the AMSR2 18 and 36 GHz T_B is ≤ 0.7 K (Maeda et al., 2016). In the daily CI datasets the mean T_{B36V} varies from 227 to 245 K and STD from 14.5 to 21.8 K. The selected STD of T_{B36V} should be larger than the radiometric resolution, but well below the daily STD for the whole data including FYI and MYI types. If we assume random-like variation of T_{B36V} to follow normal pdf then STD of 3 K gives the 5-95 percentile range of around 10 K, i.e. ± 5 K variation around the mean. Compared to the daily T_{B36V} mean this variation is only little over 2%. As first approximation the covariance matrix in (32) is scaled to have variance of T_{B36V} as 9 K^2 . The curved ice line SIC bias correction does not have an effect on the ΔB_{CI} estimation.

The estimated daily ΔB_{CI} for SIC_{25}^d and SIC_{25}^n is shown in Figure 28. ΔB_{CI} for SIC_{25}^d varies roughly from 0.35 to 0.6% when the STD of T_{B36V} is 3 K. Its most prominent temporal trend is consistent increase from mid-Apr onwards. For SIC_{25}^n ΔB_{CI} is slightly larger, on average 0.05% and at maximum 0.1%. For both SIC_{25}^d and SIC_{25}^n ΔB_{CI} is generally very small. This is due to high correlation between T_{B18V} , T_{B36V} and T_{B36H} and the nature of the v -vector in (9); the absolute value of the v_y coefficient is always larger than those for v_x and v_z , and v_y is always positive and v_x and v_z are always negative, and thus, an increase in T_{B18V} , and further in T_{B36V} and T_{B36H} , results in a SIC which is not far from the original 100% value.

The sensitivity of B_{CI} to a fraction of thin ice within FYI is investigated using tie point signatures from the combined MODIS – AMSR2 thin ice data. Thin ice with maximum thickness of 10 cm has following mean T_B values (with atmospheric correction):

$$T_{B18V} = 247 \text{ K}, T_{B18H} = 202 \text{ K}, T_{B36V} = 249 \text{ K}, T_{B36H} = 214 \text{ K}, \quad (33)$$

and snow covered FYI has:

$$T_{B18V} = 257 \text{ K}, T_{B18H} = 239 \text{ K}, T_{B36V} = 250 \text{ K}, T_{B36H} = 236 \text{ K}. \quad (34)$$

A mixture of thin ice and FYI has T_B signatures as a linear combination of these tie points. This B_{CI} sensitivity study is conducted only for single date, selected to be 15 Jan. During winter months the mean T_B 's and the v -vector coefficients are very stable. The simulated SICs with B_{CI} of SIC_{25}^d and SIC_{25}^n as a function of thin ice fraction are shown in Figure 29. They are very close to each other and decrease linearly with increasing thin ice fraction. The drop in SIC is not large for very small fractions of thin ice (like leads within FYI), e.g. 3% when the thin ice fraction is 0.1, but it is noticeably for large fractions, half of thin ice and half of FYI gives SIC decreased to 87%.

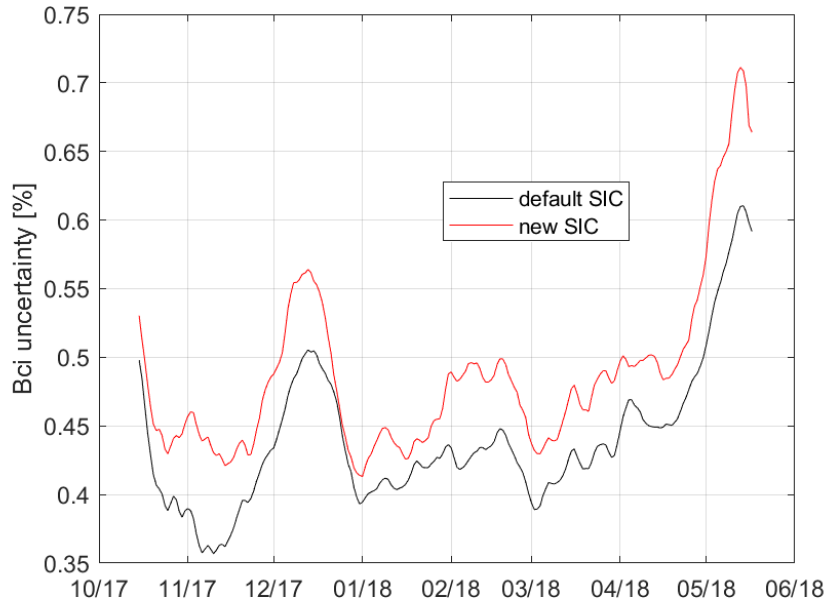


Figure 28. The B_{CI} uncertainty estimated with the propagation of error (32). The estimated daily covariance matrix between T_{B18V} , T_{B36V} and T_{B36H} was scaled to have STD of T_{B36V} of 3 K.

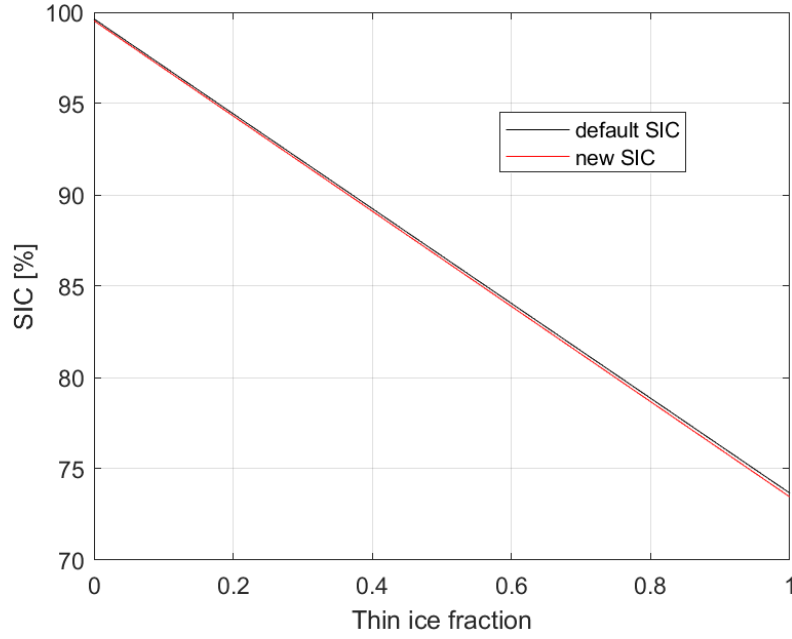


Figure 29. The B_{CI} sensitivity to fraction of thin ice with FYI. Thin ice (max thickness 10 cm) and FYI T_B tie points were derived from the combined MODIS-AMSR2 dataset. The curved ice line correction was not applied here.

8.2 SIC algorithms at 50 km grid

For the SIC_{50}^d and SIC_{50}^n algorithms the usage of the curved ice line also slightly improves σ_{SIC} (not shown); the mean σ_{SIC} decrease is 0.10% for SIC_{50}^d and 0.16% for SIC_{50}^n . σ_{SIC} 's with the CI dataset for the SIC_{50}^d and SIC_{50}^n algorithms are shown in Figure 30. Also here the new atmospheric correction (T_{eff} with (28)-(30) (Kilic et al., 2019)) does not improve the SIC data (B_{CI}) accuracy; the difference between σ_{SIC} 's is mostly very small. The difference is large only in early Oct and late May. Likely then T_{eff} estimation is hampered by moist snow and/or lower SIC. Very small difference in σ_{SIC} is also observed with the OW dataset (not shown). The rotation angles for SIC_{50}^d and SIC_{50}^n are more different than for SIC_{25}^d and SIC_{25}^n , but still the angle for B_{OW} of SIC_{50}^n is close to 0° and the angle for B_{CI} between $+25^\circ$ and $+50^\circ$. σ_{SIC} and θ are only weakly correlated ($|r| < 0.7$) in all SIC algorithms. The estimated daily ΔB_{CI} for SIC_{50}^d and SIC_{50}^n are close to each other and small, the average is around 0.4% and the maximum 0.62%, and follow Figure 28 in temporal behaviour. The B_{CI} sensitivity to the thin ice fraction is similar to Figure 29.

8.3 Further tuning experiments

First, it was investigated if there is any remnant dependence on the ERA-Interim air temperature (T_a) (T_{eff} is a function of T_a) in the CI datasets, which could be then compensated before determination of the 100% SIC ice line. In the thin detection with the AMSR2 data it was observed that $PR36$ and $GR8936H$ signatures for FYI (after the atmospheric correction) increase on average slightly as a function of T_a (Mäkynen and Similä, 2019), see Section 5.1 and (13). Figure 31 shows 2-D probability density function (pdf) plot between T_a and T_{B18V} using all daily CI datasets (25 km grid) with the original T_B data, and with the default and new atmospheric corrections. The T_a vs. T_{B18V} shows dependence with the original T_B and default correction, but not with the new atmospheric correction. The main area of FYI signatures in Figure 31 is marked with yellow and red pixels and MYI signatures are mainly below that. For T_{B36V} and T_{B36H} similar T_a behaviours

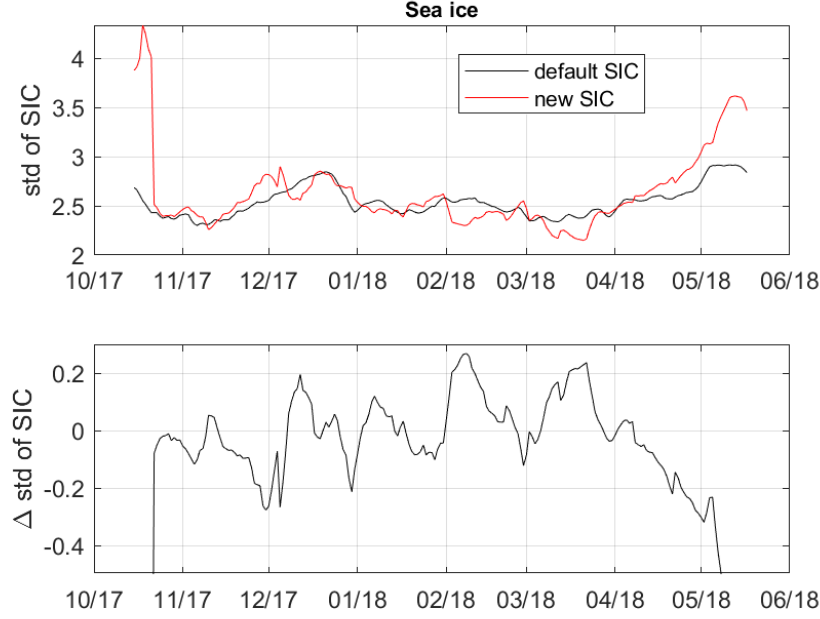


Figure 30. Daily standard deviation of SIC (i.e. uncertainty) for the SIC_{50}^d (default SIC) and SIC_{50}^n (new SIC) algorithms tuned with the CI sample dataset. The curved ice line correction was applied.

were observed. This suggests that compensation of the T_{eff} variation in the new atmospheric correction (T_{eff} estimated either with (Mathew et al., 2009)) works correctly. After the atmospheric correction with T_{eff} by (Kilic et al., 2019) T_B 's are only slightly dependent on T_a , but there are some erroneous T_B values due to inaccuracy of T_{eff} estimation in moist snow and/or lower SIC conditions.

Currently, the atmospheric correction is not possible using also the total column cloud liquid water (LW) as input, as discussed in Section 4.3. Nevertheless, we investigated if there is a relationship between LW and T_B 's in the CI data, and if thresholding LW (max allowed value) leads to decreased T_B scatter. LW in the CI data is generally very small, the mean is only 4.4 g/m^2 and 95th percentile is 20.7 g/m^2 . Figure 32 shows 2-D pdf between LW and T_{B18V} . The variation of T_{B18V} clearly decreases with increasing LW , but only very small fraction T_{B18V} values are significantly affected by LW . The tuning of SIC_{25}^n was tested by rejecting CI samples which have $LW > 20 \text{ g/m}^2$. The rejection percentage varied from 0.4 to 18.3% in the daily CI datasets, and the average was only 4.4%. Values over 10% occurred only in May. The LW thresholding did not have noticeable effect on the σ_{SIC} of B_{CI} (max difference around 0.05% in σ_{SIC}), regardless of using the curved ice line correction or not. The fraction of rejected samples is small and they do not form a separate cluster within the CI samples. It would good to check if this is the case also in summer when LW is generally higher than in winter.

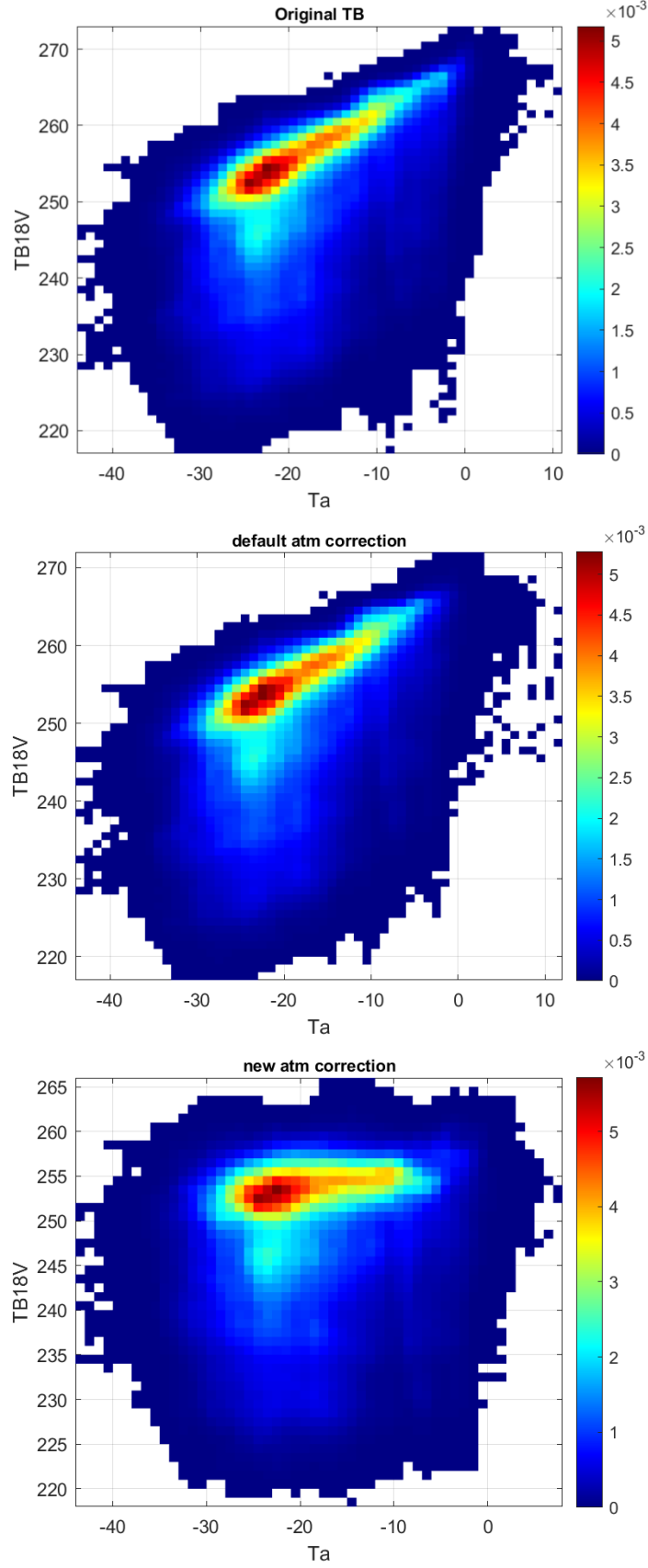


Figure 31. Probability density function between the ERA-Interim T_a and T_{B18V} using all daily CI datasets with the original T_B data, and with the default and new atmospheric corrections. Bin width is 1°C by 1 K.

The dynamic SIC tuning process presented in (Lavergne et al., 2019b) is limited to the 3-D T_B space. This is because the optimization of the projection plane is handled via a rotation angle along a 3-D axis, a geometrical concept that is difficult to upscale to more dimensions (Lavergne et al., 2019b). The generalization of this optimization to n-D space of T_B 's has not yet been developed. Now the 3-D space of T_{B18V} , T_{B36V} and T_{B36H} is used in the SIC retrieval. This space includes as 2-D projections Bootstrap polarization and frequency mode SIC algorithms. The three T_B channels are also used in the Bristol SIC algorithm. It is possible to use other T_B channels or their sums and differences for the dynamic SIC algorithm. The sums and differences of T_B 's at the same frequency are the first and second Stokes parameters in brightness temperature. The usage of polarization and gradient ratios is not possible as they are not linear functions of SIC. A three channel combination should be formed so that the CI dataset forms a highly elongated feature, i.e. its scatter or variance is mainly in one direction. This gives robust determination of the ice line with PCA, its direction has little variation if some daily CI data are excluded or more data are added.

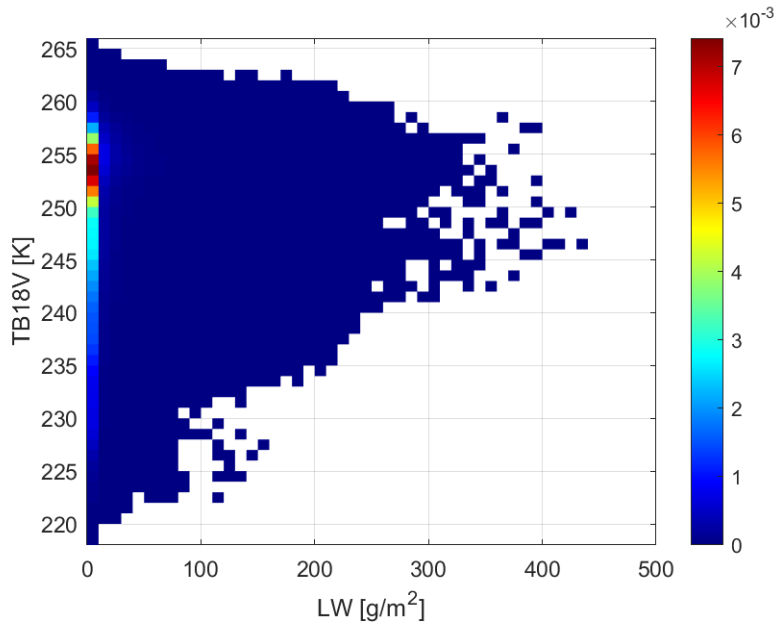


Figure 32. Probability density function between the ERA-Interim LW and T_{B18V} using all daily CI datasets with the atmospheric correction. Bin width is 10 g/m^2 by 1 K .

Within the four 18 and 36 GHz T_B channels there is four different choices for a three channel group, each have two V-pol or two H-pol channels. The usage of more V-pol channels is likely preferable as at 36 GHz layering in the dry snow cover strongly influences the H-pol T_B 's, but leaves the V-pol T_B 's largely unchanged due to the Brewster angle effect (Mätzler et al., 1984). T_B sums are only meaningful between V- and H-pol T_B 's at the same frequency, and thus, there is two possible choices: $T_{B18V} + T_{B18H}$ and $T_{B36V} + T_{B36H}$. Usable T_B differences includes those between V- and H-pol T_B 's at the same frequency, which are typically small for sea ice and large for open water, and also $T_{B36V} - T_{B18V}$ and $T_{B36H} - T_{B18H}$. The gradient ratio between T_{B36V} and T_{B18V} is used in the NT SIC algorithm (Cavalieri et al., 1984). $T_{B36V} - T_{B18V}$ and $T_{B36H} - T_{B18H}$ are large (positive) for open water, typically close to zero or slightly negative for FYI, and negative for MYI. The requirement for an elongated cluster of CI datapoints is assumed to limit to usage of only one T_B difference at a time.

Table 5 shows results of B_{CI} tuning (σ_{SIC} and ΔB_{CI}) for SIC_{25}^d (default atmospheric correction) with different combinations T_B 's and sums and differences of T_B 's at 18 and 36 GHz. Not all different channel combinations are shown in the table. The curved ice line correction was not applied here. For SIC_{25}^d the same tuning testing was conducted (results not shown here). Figure 33 shows daily

σ_{SIC} and ΔB_{CI} for SIC_{25}^d . For the ΔB_{CI} calculation covariance matrix between all 18 and 36 GHz channels was first derived and then it was scaled to have 3K STD for T_{B36V} . Daily ΔB_{CI} was estimated here with the Monte Carlo method instead of (32) as we wanted to have the same parameter, STD of T_{B36V} , as basis for ΔB_{CI} estimation in all different three channel combinations. ΔB_{CI} with the default channels is larger than in Section 8.1 because here the covariance matrix was calculated using all four 18 and 36 GHz channels, but earlier using only three.

The results for both SIC_{25}^d and SIC_{25}^n show that none of the new 3-D channel combinations are substantially better than the default $T_{B18V} - T_{B36V} - T_{B36H}$, but some are worse. In addition, the sensitivity of B_{CI} to fraction of thin ice within FYI is the second best with the default channels after the $(T_{B18V} + T_{B18H}) - (T_{B36V} + T_{B36H}) - (T_{B36V} - T_{B18V})$ combination, see Figure 34. In the figure SIC is not exactly 100% in the absence of thin ice because the FYI tie point from the AMSR2-MODIS data is not exactly on the 100% ice line.

Nevertheless, channel combinations which yielded equal σ_{SIC} and ΔB_{CI} to those with the default one will be investigated further in the next Section (SIC values and time series are compared). These are: $T_{B36V} - T_{B18V} - T_{B18H}$, $T_{B18H} - T_{B36V} - T_{B36H}$, $T_{B36V} - T_{B36H} - (T_{B36V} - T_{B18V})$ and $T_{B18V} - T_{B18H} - (T_{B36V} - T_{B18V})$.

Table 5. Tuning of B_{CI} for SIC_{25}^d with different three channel combinations of T_B 's, and sums and differences of T_B 's and using the daily OW and CI datasets. The tuning result is characterized with STD of B_{CI} and B_{CI} uncertainty (ΔB_{CI}) which was calculated by scaling the empirical daily covariance matrix between 18 and 38 GHz T_B 's to have 3K STD for T_{B36V} .

Parameters	STD of B_{CI} [%] ¹⁾		ΔB_{CI} ¹⁾ [%]		Comment
$T_{B18V}, T_{B36V}, T_{B36H}$	2.7	0.15	1.3	0.16	default choice
$T_{B36V}, T_{B18V}, T_{B18H}$	2.7	0.20	1.3	0.17	two V-pols, T_{B18H}
$T_{B36H}, T_{B18V}, T_{B18H}$	3.1	0.22	1.5	0.20	two H-pols, T_{B18V}
$T_{B18H}, T_{B36V}, T_{B36H}$	2.6	0.24	1.3	0.19	two H-pols, T_{B36V}
two T_B 's and one T_B difference					
$T_{B36V}, T_{B36H},$ $T_{B18V} - T_{B18H}$	3.7	0.27	1.8	0.28	$T_{B18V} - T_{B18H}$ instead T_{B18V}
$T_{B36V}, T_{B36H},$ $T_{B36V} - T_{B18V}$	2.7	0.14	1.3	0.15	$T_{B36V} - T_{B18V}$ instead T_{B18V}
$T_{B18V}, T_{B18H},$ $T_{B36V} - T_{B18V}$	2.7	0.20	1.3	0.17	
two T_B sums and one T_B difference					
$T_{B18V} + T_{B18H},$ $T_{B36V} + T_{B36H},$ $T_{B36V} - T_{B18V}$	3.3	0.28	1.6	0.13	

1) Mean and STD of daily $\sigma_{SIC}/\Delta B_{CI}$ values.

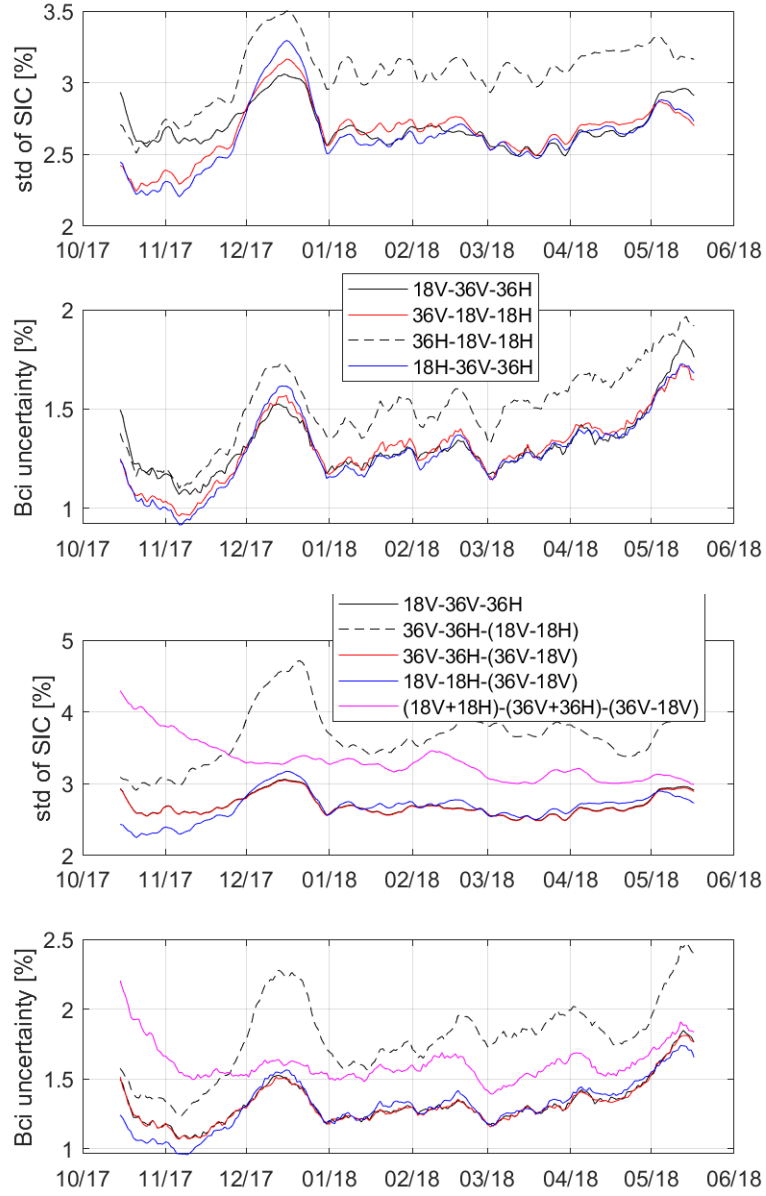


Figure 33. Daily standard deviation of B_{CI} and B_{CI} uncertainty (ΔB_{CI}) calculated with the CI dataset having the default T_B atmospheric correction for different three channel combinations of T_B 's, and sums and differences of T_B 's. The covariance matrix for ΔB_{CI} was scale to have 3K STD for T_{B36V} .

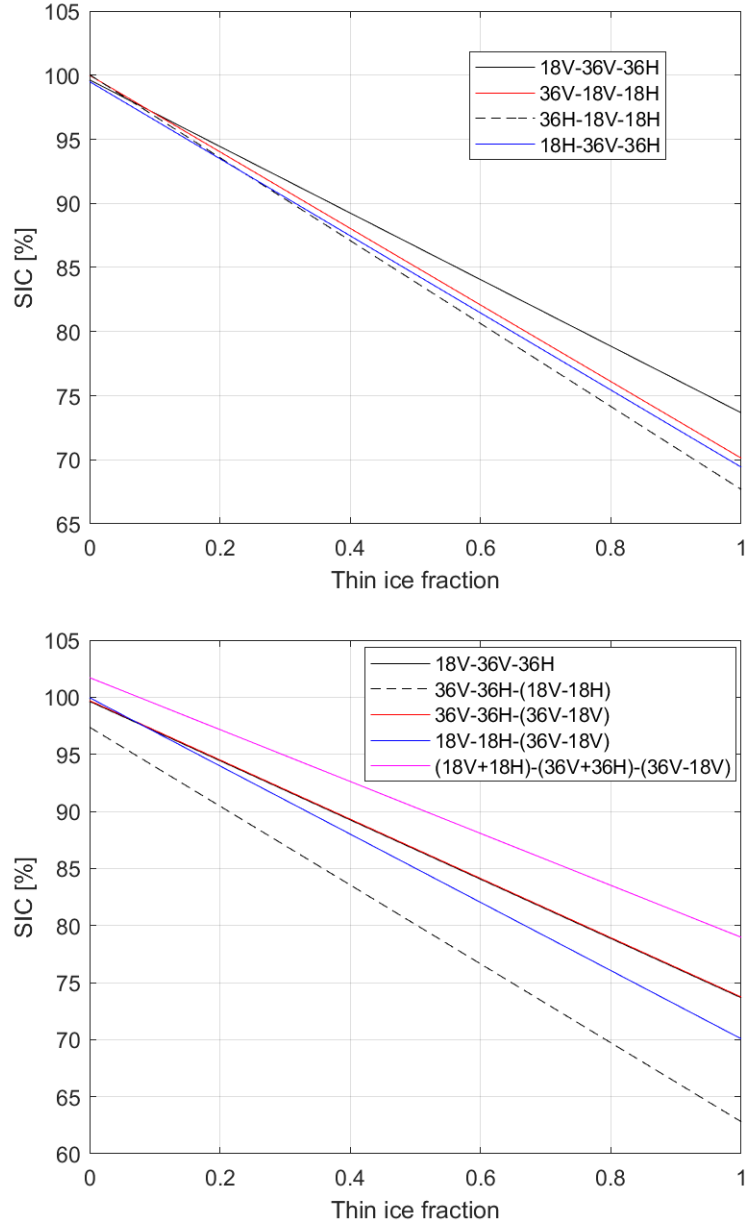


Figure 34. Sea ice concentration with B_{CI} for SIC_{25}^d as a function of thin ice fraction. Thin ice (max thickness 10 cm) and FYI T_B tie points were derived from the combined MODIS-AMSR2 dataset.

9 Comparison between Different SIC Datasets

Different SIC datasets at 25 and 50 km pixel sizes are here compared to each other. The first comparison is conducted between the SIC swath datasets and using pixels where the OSI-450 SIC with the default atmospheric correction (SIC_{25}^d or SIC_{50}^d) is over 90% (we are only interested about SIC values close to 100%). Next, mean SICs as a function of time from the three test sites shown in Figure 18 are compared. The time period for these comparisons is mid-winter, from Dec to Apr 2018, and the focus is on Arctic high SIC pack ice. Based on the results in Section 8.3 also following three channel combinations: $T_{B36V} - T_{B18V} - T_{B18H}$, $T_{B18H} - T_{B36V} - T_{B36H}$, $T_{B36V} - T_{B36H} - (T_{B36V} - T_{B18V})$ and $T_{B18V} - T_{B18H} - (T_{B36V} - T_{B18V})$, are used also to retrieve SIC at 25 km pixel size and compared with SIC by SIC_{25}^d and SIC_{25}^n . It was decided not to use the curved ice line correction in here in order to see better the effect of the new T_B atmospheric correction.

9.1 Comparison between pixel SIC values

Figure 35 shows probability density plot between SIC_{25}^d and SIC_{25}^n values in the swath SIC charts. The density plot shows concentration of SIC_{25}^d vs. SIC_{25}^n values along the one-to-one line, but SIC_{25}^n can be noticeably smaller or larger (up to 10%) than SIC_{25}^d . The correlation between SIC_{25}^d and SIC_{25}^n is very high, on average 0.97 in the swath charts. A density plot between SIC_{25}^d vs. $SIC_{25}^d - SIC_{25}^n$ (not shown) has 81% of values when $SIC_{25}^d \geq 95\%$ & $SIC_{25}^d \leq 105\%$ & $|SIC_{25}^d - SIC_{25}^n| \leq 3\%$, and it does not show any trends as a function of SIC_{25}^d . The pdf of the SIC difference in Figure 36 is very symmetrical around the 0% point; 50% of the differences have $SIC_{25}^d > SIC_{25}^n$ (variation from -7% to +18%), but within the single swaths there are sometimes cases with a large fraction of positive or negative differences. Figure 37 shows mean SIC_{25}^d vs. SIC_{25}^n from all pixels within a single swath with $SIC_{25}^d \geq 90\%$. Their correlation is 0.87 and the max absolute difference is only around 2.5%, and thus, these swath means are very close to each other.

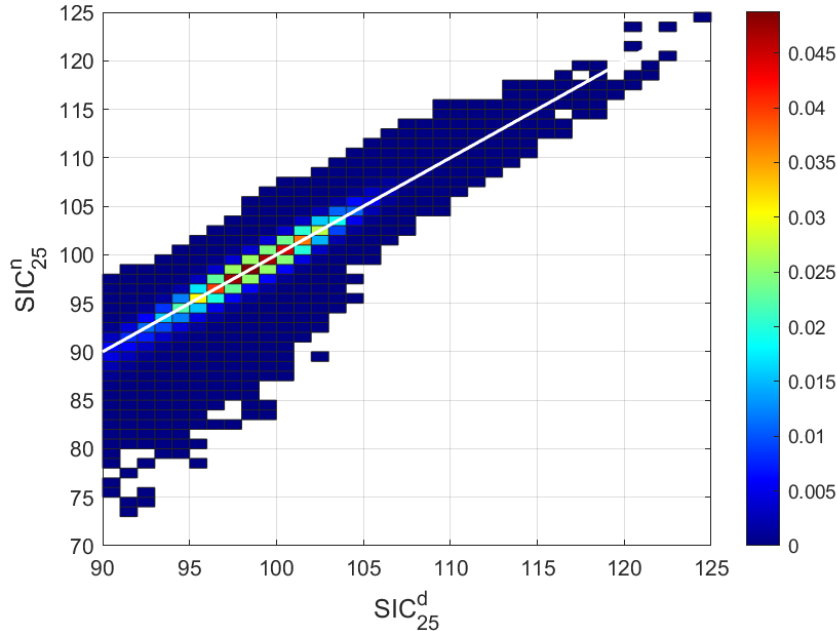


Figure 35. Probability density plot between SIC_{25}^d (OSI SAF default; 25 km pixel size) and SIC_{25}^n (FYI and MYI emissivities and T_{eff} from T_a) swath datasets when $SIC_{25}^d \geq 90\%$. Time period is Dec 2017 – Apr 2018. White line shows one-to-one correspondence. Bin widths are 1%.

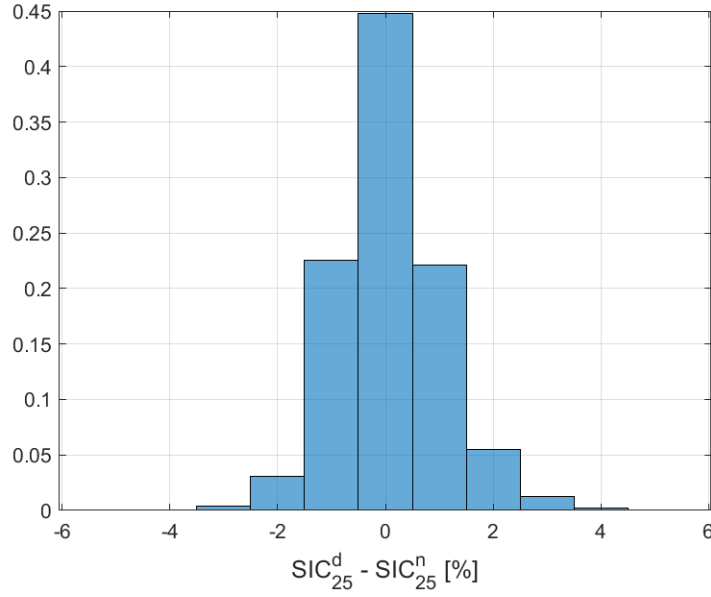


Figure 36. Probability density function for $SIC_{25}^d - SIC_{25}^n$. Bin width is 1%.

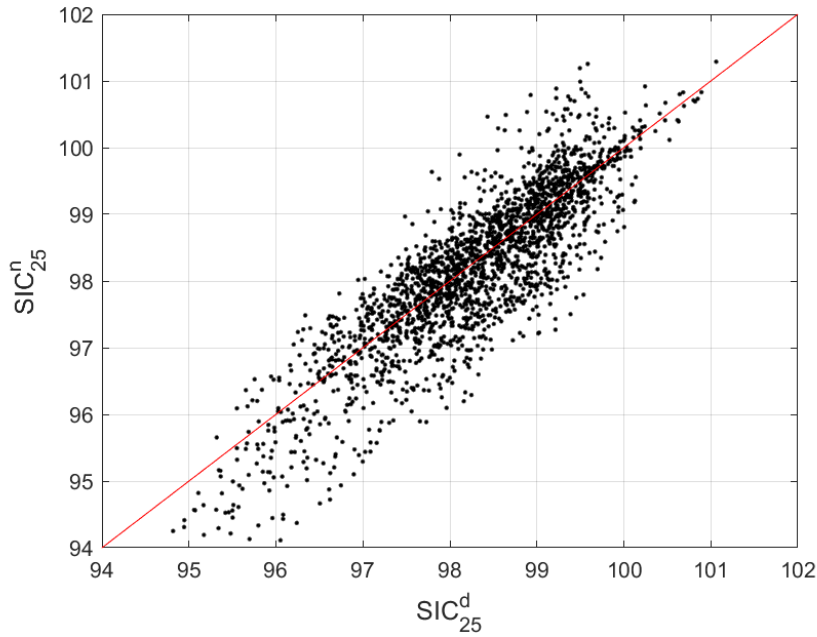


Figure 37. Mean SIC_{25}^d vs. mean SIC_{25}^n from all pixels from a single swath with $SIC_{25}^d \geq 90\%$.

In summary, SIC_{25}^d and SIC_{25}^n in the high end of SIC, when $SIC_{25}^d \geq 90\%$, are on average very close to each other. The swath based absolute means differ less than 2.5%. The difference between single SIC values ($SIC_{25}^d - SIC_{25}^n$) varies roughly from -7% to +18%, but it is mostly very small, see Figure 36. However, within single swaths there are sometimes cases with a large fraction of positive or negative SIC differences.

Next, the above analysis is conducted for the SIC_{50}^d and SIC_{50}^n (new FYI and MYI emissivities and T_{eff} derived from T_B by (Kilic et al., 2019)) datasets. The 2-D pdf plot in Figure 38 shows concentration of SIC values along the one-to-one line when $95 < SIC_{50}^d < 105\%$, but there are some SIC_{50}^n values that are much higher than SIC_{50}^d and which overestimate SIC badly ($SIC \gg 100\%$). The average correlation between SIC_{50}^d and SIC_{50}^n is 0.88, noticeable smaller than between SIC_{25}^d and

SIC_{25}^n (0.97). However, 80% of the data are within $SIC_{50}^d \geq 95\%$ & $SIC_{50}^d \leq 105\%$ & $|SIC_{50}^d - SIC_{50}^n| \leq 3\%$. The swath means of SIC_{50}^d and SIC_{50}^n from pixels with $SIC_{50}^d > 90\%$ are close to each other, see Figure 39; the correlation is not high (0.78), but the max absolute difference is only around 2.5%. In general, the results show that on average SIC_{50}^d and SIC_{50}^n are close to each other. However, as with the 25 km SIC data there are cases with a large fraction of positive or negative SIC differences between SIC swath datasets.

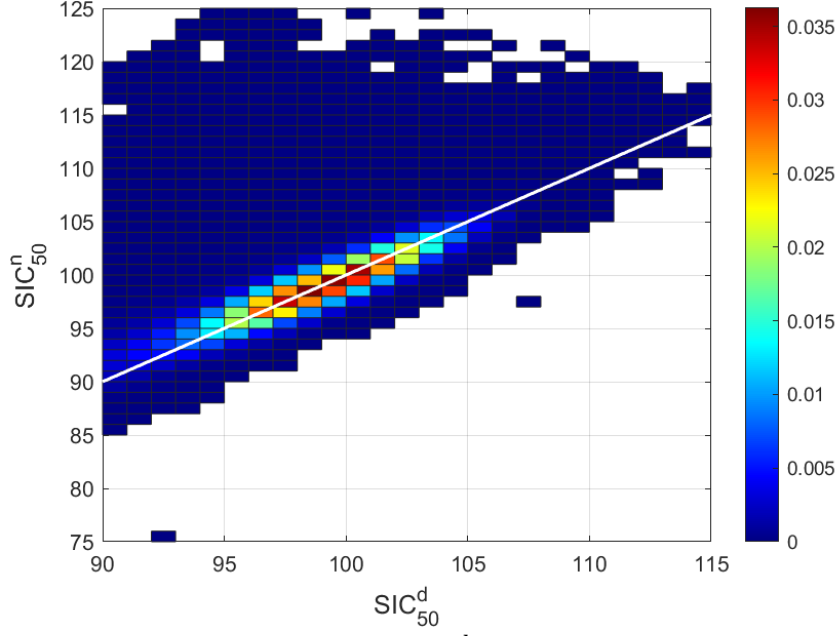


Figure 38. Probability density plot between SIC_{50}^d (OSI SAF default) and SIC_{50}^n (FYI and MYI emissivities and T_{eff} from T_B) swath datasets when $SIC_{50}^d \geq 90\%$. Time period is Dec 2017 – Apr 2018. White line shows one-to-one correspondence. Bin widths are 1%.

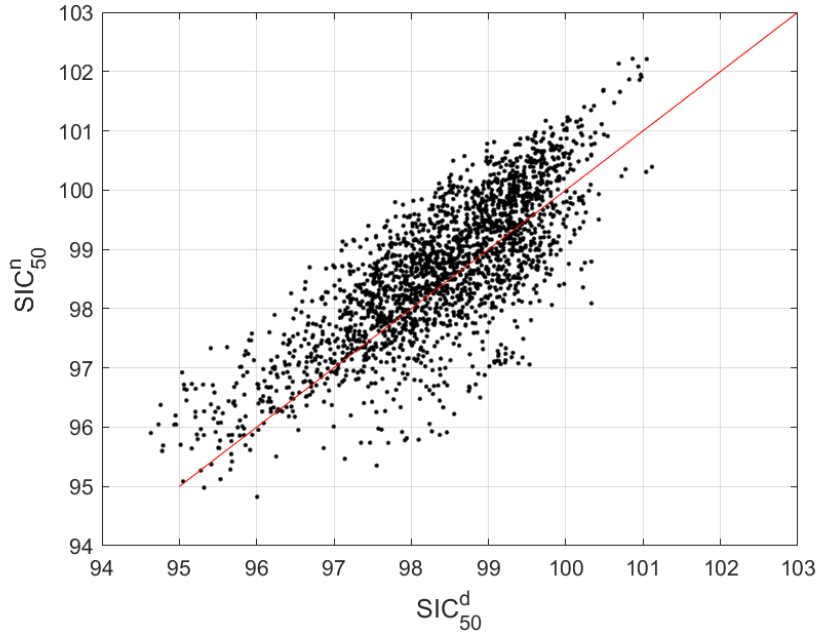


Figure 39. Mean SIC_{50}^d vs. mean SIC_{50}^n from all pixels from a single swath with $SIC_{50}^d \geq 90\%$.

9.1.1 Other three channels combinations

SIC values ($SIC_{25}^d \geq 90\%$) with four other chosen three channel combinations: $T_{B36V} - T_{B18V} - T_{B18H}$, $T_{B18H} - T_{B36V} - T_{B36H}$, $T_{B36V} - T_{B36H} - (T_{B36V} - T_{B18V})$ and $T_{B18V} - T_{B18H} - (T_{B36V} - T_{B18V})$, were here studied against high end SIC_{25}^d values ($\geq 90\%$). Here the default OSI-450 atmospheric correction was used. The $T_{B36V} - T_{B36H} - (T_{B36V} - T_{B18V})$ combination is very highly correlated (r is ~ 1) with the default one, and thus, the SIC differences are insignificant. The $T_{B36V} - T_{B18V} - T_{B18H}$ SIC has high correlation, 0.89, but the mean swath SIC is mostly slightly smaller (up to 2.5%) than that with the default channel combination, see Figure 40. 57% of single SIC values are smaller than SIC_{25}^d . For the $T_{B18H} - T_{B36V} - T_{B36H}$ combination (T_{B18H} instead of T_{B18V}) the correlation is also high, 0.90. It has also tendency for smaller SIC values; the mean SIC is up to 2% smaller and 63% of single SIC values are smaller than the default SIC. The $T_{B18V} - T_{B18H} - (T_{B36V} - T_{B18V})$ has equal correlation, 0.90, as the last two channel combinations discussed above, and it also more underestimates (58% of single SIC values) than overestimates SIC compared to SIC_{25}^d .

The results here show the $T_{B36V} - T_{B36H} - (T_{B36V} - T_{B18V})$ combination gives SIC values very close to those with SIC_{25}^d , and it can be dropped from further comparisons. The other three combinations give slightly more often smaller than larger SIC values compared to SIC_{25}^d . Comparison between SIC time series in Section 9.2 should give more insight to their differences.

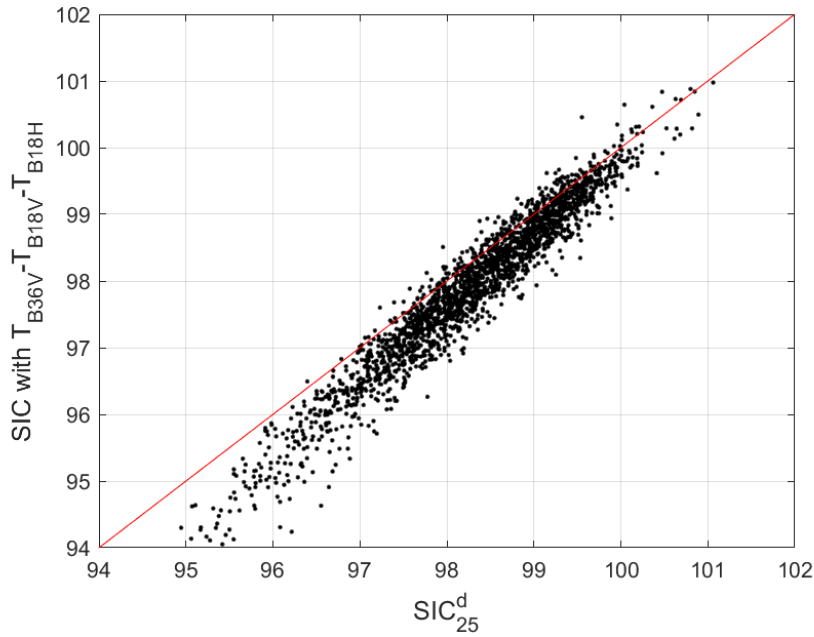


Figure 40. Mean SIC_{25}^d vs. mean SIC with the $T_{B36V} - T_{B18V} - T_{B18H}$ channel combination using all pixels from a single swath with $SIC_{25}^d \geq 90\%$.

9.2 Comparison between mean SICs as a function of time

Further comparison between the SIC datasets is conducted using the previous three test sites shown in Figure 18. Following statistics are used in the comparison: mean and STD of SIC over a test site, and mean pixel based bias to 100% SIC ($\text{mean}(SIC_i - 100\%)$). These statistics are calculated only when a swath dataset covers fully a test site. The size of the sites is 15 by 15 pixels. A SIC_{25}^d chart for the same AMSR2 swath dataset as in Figure 18 is shown in Figure 41. This chart illustrates SIC noise over MYI; areas with SIC noticeably over or under 100% when the true SIC is very likely close to 100%. Figure 42 shows the mean SIC_{25}^d and SIC_{25}^n and the their difference for the test site 1

(on the right in Figure 41). Here SIC_{25}^d is always below 100%, and thus, SIC is underestimated if the true SIC is close 100%. However, there are couple of SIC_{25}^d dips which likely represent true low SIC, i.e. large leads have formed. The mean SIC_{25}^n is not consistently smaller or larger than the mean SIC_{25}^d . The difference $SIC_{25}^d - SIC_{25}^n$ is only from around -2.5% to +2%. Std of SIC_{25}^n is typically slightly larger than STD of SIC_{25}^d (max difference 0.5%). This is due to spatial variation of between T_{eff} and T_{effref} which is not present in ΔT_{BC}^d . Likewise is the mean SIC anomaly mostly slightly larger for SIC_{25}^n (up to 3%). The mean SICs for the test site in the middle of Figure 41 (test site 2) are shown in Figure 43. For this test site the mean SIC_{25}^d is mostly over 100%. Also here the mean SIC_{25}^n is not systematically smaller or larger than the mean SIC_{25}^d . The temporal variation, characterized with STD, is somewhat larger for SIC_{25}^n in the both test sites. For the test site on the left in Figure 29 which also has SIC overestimation by SIC_{25}^d , the results are similar. Monthly averages of SIC_{25}^d and SIC_{25}^n for each test site are very close to each other, differences are less than 1%.

Next, this SIC comparison is repeated with SIC_{50}^d and SIC_{50}^n data. For the test site 1 SIC_{50}^d is also below 100%. SIC_{50}^d should be very close to SIC_{25}^d as they are both calculated with the same OSI-450 SIC algorithm, only difference is the T_B grid size. The mean SIC_{50}^n follows closely the mean SIC_{50}^d , difference varies quite randomly from -1% to +4%. Unlike with the 25 km data, STD of SIC_{50}^n is mostly slightly smaller (typically $\sim 0.5\%$) than STD of SIC_{50}^d . For the two other test sites SIC_{50}^d usually overestimates SIC, see an example in Figure 44, but SIC_{50}^n does not correct this.

It seems that the new atmospheric T_B corrections for the 25 and 50 km data (new FYI and MYI emissivities and with T_{eff} from T_a or T_B) do not decrease SIC noise and SIC under- or overestimation compared to the OSI-450 default correction.

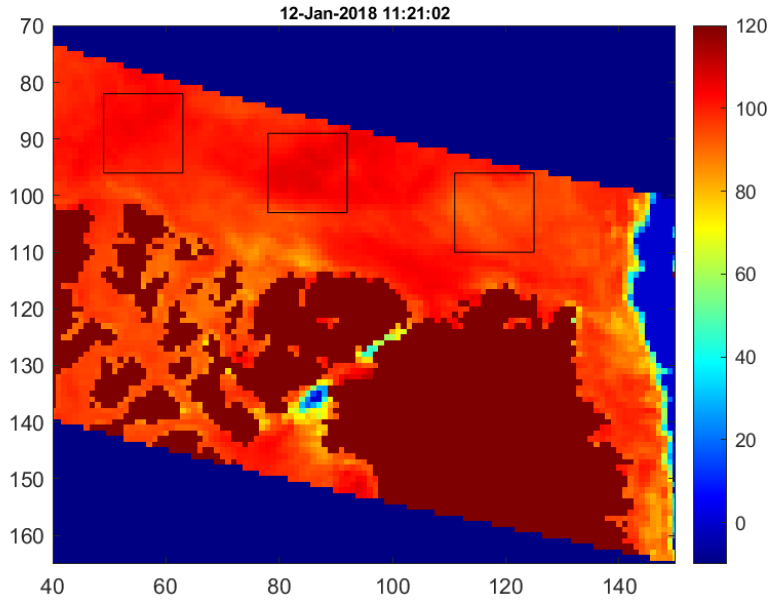


Figure 41. Sea ice concentration swath chart using the T_B data with the OSI SAF default atmospheric correction. Pixel size is 25 km. The curved ice line correction was not used here. Black rectangle areas are used in the comparison of different SIC datasets.

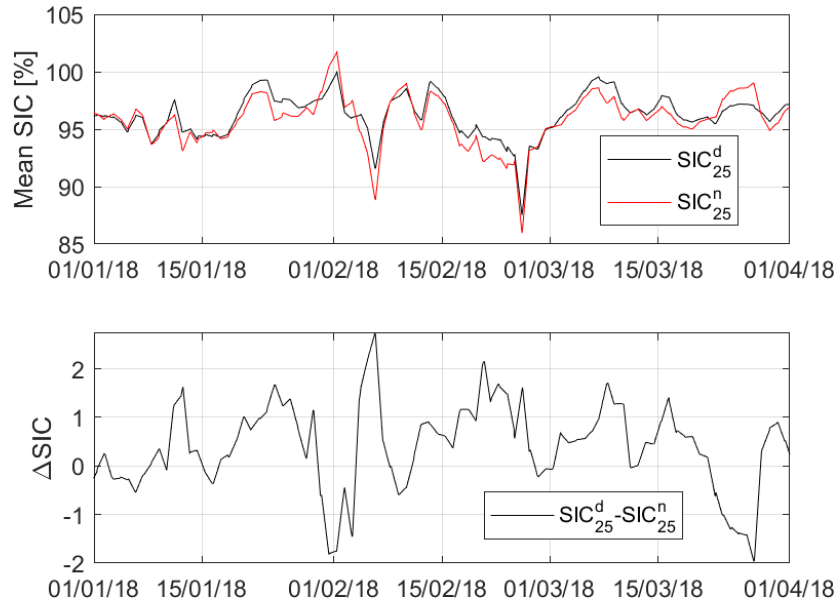


Figure 42. Mean sea ice concentration for the rightmost test site in Figure 41 with SIC_{25}^d and SIC_{25}^n .

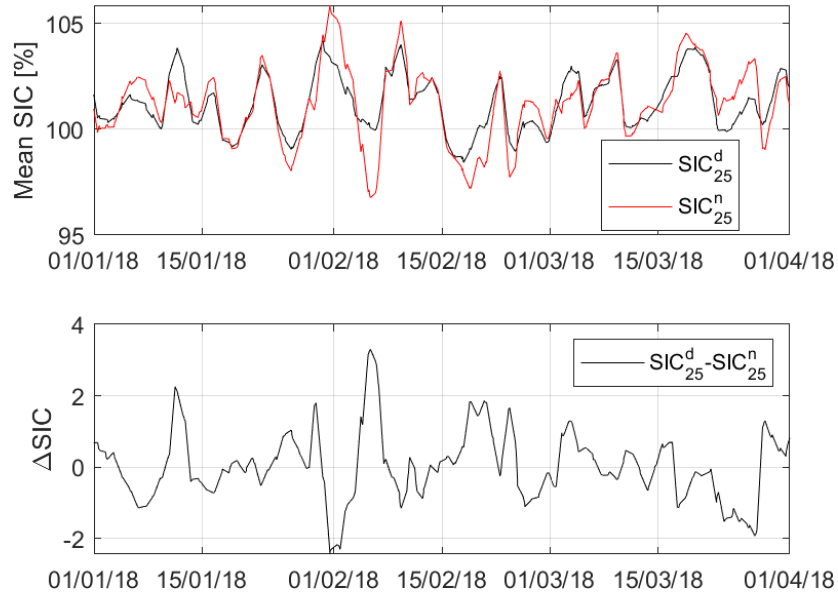


Figure 43. Mean sea ice concentrations for the middle test site in Figure 41 with SIC_{25}^d and SIC_{25}^n .

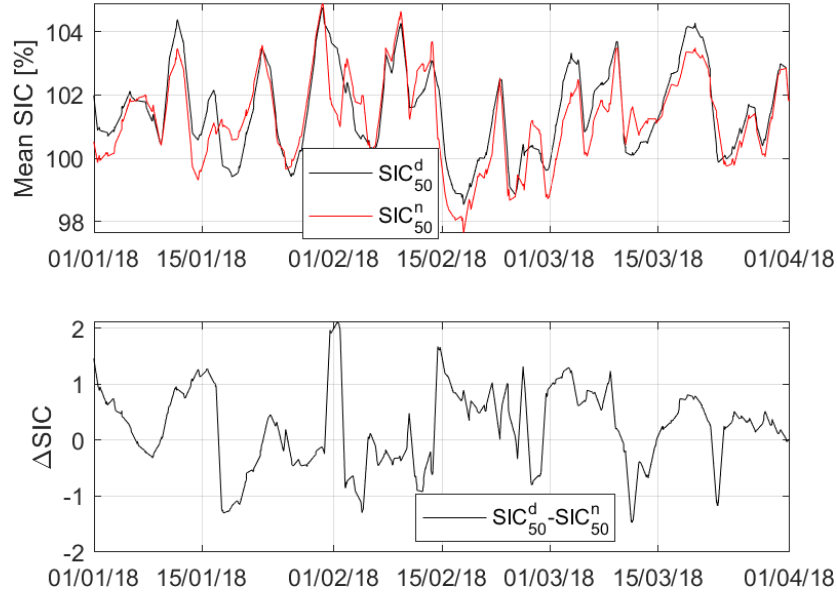


Figure 44. Mean sea ice concentrations for the middle test site in Figure 41 with SIC_{50}^d and SIC_{50}^n .

9.2.1 Other three channels combinations

Previously, it was found that the $T_{B36V} - T_{B36H} - (T_{B36V} - T_{B18V})$ combination gives SIC values very close to those with SIC_{25}^d . This is also the case for the mean SIC time series. The combinations $T_{B36V} - T_{B18V} - T_{B18H}$, $T_{B18H} - T_{B36V} - T_{B36H}$ and $T_{B18V} - T_{B18H} - (T_{B36V} - T_{B18V})$ give mean SICs for the test site 1 which are somewhat smaller (roughly 1% to 4%) than that with SIC_{25}^d . For the other two test sites the mean SICs are also smaller than with SIC_{25}^d which overestimates SIC. Therefore, there is more a constant bias compared to SIC_{25}^d , instead of consist move towards 100% SIC. This is also shown in the monthly mean SICs. These other three channel combinations do not seem to yield better quality SIC data than the default combination in SIC_{25}^d .

10 Conclusions and Recommendations

We have investigated here various methods for the SIC noise reduction and data quality improvement in wintertime in the OSI-450 SIC algorithm. The new T_B atmospheric correction with temporally (daily) changing FYI and MYI tie point emissivities (e_a 's) and FYI and FYI T_{eff} 's by Mathew et al. (2009) for T_{Bnwp} , and fixed reference e_a 's and T_{eff} 's for T_{Bref} did not improve quality of the SIC data; e.g. there was no significant reductions in SIC under- or overestimation and temporal variation of mean SIC over selected test sites within the Arctic high SIC pack ice. Further, for swath data pixels with $SIC_{25}^d \geq 90\%$ the pixel-wise difference $SIC_{25}^d - SIC_{25}^n$ has a narrow distribution with 0% mean and 1.0% STD (see Figure 36), and also the swath means are very close to each other (max difference is 2.5%) and have high correlation (0.87). However, within the single swaths there are sometimes cases with a large fraction of positive or negative $SIC_{25}^d - SIC_{25}^n$ differences, and thus, the difference is not just random, but sometimes reflecting (likely) different atmospheric corrections.

For the OSI-450 default algorithms (here 25 and 50 km grids) σ_{SIC} 's are already very small, below 3%, with or without the curved ice line correction. Lavergne et al. (2019b) gives the inherent accuracy of the OSI-450 algorithm (σ_{algo}^2) less than 3% (see Figure 7 in there). Uncertainty ΔB_{CI} (sensitivity to small random-like T_B changes) for the default algorithms varies roughly from 0.35 to 0.6% when the STD of T_{B36V} is 3 K. It is likely that any improvement requires better closed ice sampling to include only FYI and MYI samples with SIC very close 100%, reduction of the effects from variable sea ice and snow properties, or further modification the ice line in addition to the now used curved ice line.

For both the default OSI-450 SIC data and that with the new T_B atmospheric correction the curved ice line correction slightly decreased σ_{SIC} 's (max around 0.3%), which justifies its usage. In future a further correction of the T_B data based on physical relationships between sea ice (and snow) properties and measured T_B 's should be investigated. This requires in-situ sea ice datasets and emissivity modelling. It is noted that we are not sure if the curved ice line correction used here is the same as in the operational OSI-450 algorithm, because it is not fully documented in any publication. Unfortunately, we did not find any better method than the curved ice line correction to improve the SIC data quality.

The OSI SAF atmospheric correction scheme corrects only for the total water vapour as T_{eff} and T_{effref} are equal, they are calculated from the same instantaneous T_a data. In the new correction scheme T_{eff} and T_{effref} are different, and thus, a change in T_{eff} is in principle corrected. However, it is possible that estimation of T_{eff} and T_{effref} from the T_a data is too inaccurate.

We also tested T_{eff} estimation from the T_B data (Kilic et al., 2019) for the atmospheric correction. This is only valid for sea ice with 100% SIC. The resulting SIC_{50}^n dataset also does not show clear improvements compared to the OSI SAF default SIC data (SIC_{50}^d). For applying T_{eff} estimation from T_B for $SIC < 100\%$ the sea ice/ocean contribution in the measured T_B should be estimated. This is possible with RTM modelling or open water tie points, but the accuracy of the resulting sea ice T_B data may not be high enough. An empirical relationship between T_{eff} and T_a was found to be too inaccurate for the atmospheric correction. Likely the T_{eff} estimation from the T_B data is not an accurate enough solution for the OSI SAF SIC algorithms.

It seems that only the new atmospheric correction (T_{eff} with (Mathew et al., 2009)) does not leave any remnant dependence between T_a and T_B 's, see Figure 31. This is a major observation speaking in favour to use the new correction. Using the correction with T_{eff} by (Kilic et al., 2019) T_B 's are only

slightly dependent on T_a , but there are erroneous T_B values due to the inaccuracy of the T_{eff} estimation in moist snow and/or lower SIC conditions.

Rejecting T_B data in the CI dataset by thresholding total cloud liquid water content did not decrease the scatter (i.e. σ_{SIC}) around the ice line. In winter conditions LW is typically very small, and the rejected samples did not form a separate cluster within the CI samples. It would be good to check if this is the case also in summer when LW is generally higher than in winter.

The 3-D tuning process of the B_{CI} algorithm was also applied to different combinations of T_B 's and sums and differences of T_B 's at 18 and 36 GHz, see Table 5, and σ_{SIC} and ΔB_{CI} were calculated. The sensitivity of different combinations to the thin ice fraction was also investigated. The curved ice line correction was not applied in here. The results with the default and new atmospheric correction show that none of the new 3-D channel combinations are substantially better than the default $T_{B18V} - T_{B36V} - T_{B36H}$, but some are worse. In addition, the insensitivity of B_{CI} to the fraction of thin ice within FYI is the second best with the default channels, see Figure 34.

Main recommendations from this study can be summarized as:

- We think it would be worthwhile to test new parametrisations in the T_B atmospheric correction within the OSI-450 SIC software by metno.
- T_{eff} estimation from the T_B data (Kilic et al., 2019) for the T_B atmospheric correction does not seem to be a viable solution as in principle the T_{eff} estimates are valid only for 100% SIC.
- Simple thin ice detection method developed here can be used to exclude thin ice pixels (but not all) from the determination of the 100% ice line.

11 References

- Andersen, S.: Monthly Arctic sea ice signatures for use in passive microwave algorithms, DMI, Copenhagen, DK., 1998.
- Andersen, S., Tonboe, R., Kern, S. and Schyberg, H.: Improved retrieval of sea ice total concentration from spaceborne passive microwave observations using numerical weather prediction model fields: An intercomparison of nine algorithms, *Remote Sens. Environ.*, 104(4), 374–392, doi:10.1016/j.rse.2006.05.013, 2006.
- Andersen, S., Tonboe, R., Kaleschke, L., Heygster, G. and Pedersen, L. T.: Intercomparison of passive microwave sea ice concentration retrievals over the high-concentration Arctic sea ice, *J. Geophys. Res.*, 112(C8), C08004, doi:10.1029/2006JC003543, 2007.
- Cavalieri, D. J.: A microwave technique for mapping thin sea ice, *J. Geophys. Res.*, 99(C6), 12561–12572, doi:10.1029/94JC00707, 1994.
- Cavalieri, D. J., Gloersen, P. and Campbell, W. J.: Determination of sea ice parameters with the NIMBUS 7 SMMR, *J. Geophys. Res.*, 89(D4), 5355–5369, doi:10.1029/JD089iD04p05355, 1984.
- Cavalieri, D. J., Crawford, J. P., Drinkwater, M. R., Eppler, D. T., Farmer, L. D., Jentz, R. R. and Wackerman, C. C.: Aircraft active and passive microwave validation of sea ice concentration from the Defense Meteorological Satellite Program special sensor microwave imager, *J. Geophys. Res.*, 96(C12), 21989, doi:10.1029/91JC02335, 1991.
- Cavalieri, D. J., St. Germain, K. M. and Swift, C. T.: Reduction of weather effects in the calculation of sea-ice concentration with the DMSP SSM/I, *J. Glaciol.*, 41(139), 455–464, doi:10.3189/S0022143000034791, 1995.
- Cho, K., Sato, Y. and Naoki, K.: Thin ice area extraction in the sea of Okhotsk from GCOM-W1/AMSR2 data, *Int. Arch. Photogramm. Remote Sens. Spatial Inf. Sci.*, XLI-B8, 463–468, doi:10.5194/isprsarchives-XLI-B8-463-2016, 2016.
- Cho, K., Miyao, K. and Naoki, K.: Thin ice area extraction in the seasonal sea ice zones of the northern hemisphere using AMSR2 data, *Int. Arch. Photogramm. Remote Sens. Spatial Inf. Sci.*, XLII-3/W7, 5–9, doi:10.5194/isprs-archives-XLII-3-W7-5-2019, 2019.
- Comiso, J. C.: Characteristics of Arctic winter sea ice from satellite multispectral microwave observations, *J. Geophys. Res.*, 91(C1), 975, doi:10.1029/JC091iC01p00975, 1986a.
- Comiso, J. C.: Characteristics of Arctic winter sea ice from satellite multispectral microwave observations, *J. Geophys. Res.*, 91(C1), 975, doi:10.1029/JC091iC01p00975, 1986b.
- Comiso, J. C. and Cho, K.: “Description of GCOM-W1 AMSR2 sea ice concentration algorithm,” in “Descriptions of GCOM-W1 AMSR2 Level 1R and Level 2 algorithms,” Japan Aerospace Exploration Agency, Earth Observation Research Center., 2013.
- Comiso, J. C., Cavalieri, D. J., Parkinson, C. L. and Gloersen, P.: Passive microwave algorithms for sea ice concentration: A comparison of two techniques, *Remote Sens. Environ.*, 60(3), 357–384, doi:10.1016/S0034-4257(96)00220-9, 1997.
- Dee, D. P., Uppala, S. M., Simmons, A. J., Berrisford, P., Poli, P., Kobayashi, S., Andrae, U., Balmaseda, M. A., Balsamo, G., Bauer, P., Bechtold, P., Beljaars, A. C. M., van de Berg, L., Bidlot, J., Bormann, N., Delsol, C., Dragani, R., Fuentes, M., Geer, A. J., Haimberger, L., Healy, S. B., Hersbach, H., Hólm, E. V., Isaksen, I., Kållberg, P., Köhler, M., Matricardi, M., McNally, A. P., Monge-Sanz, B. M., Morcrette, J.-J., Park, B.-K., Peubey, C., de Rosnay, P., Tavolato, C., Thépaut, J.-N. and Vitart, F.: The ERA-Interim reanalysis: configuration and performance of the data assimilation system, *Quart. J. Roy. Meteorological Soc.*, 137(656), 553–597, doi:10.1002/qj.828, 2011.

- Hastie, T., Tibshirani, R. and Friedman, J. H.: The elements of statistical learning: data mining, inference, and prediction, 2nd ed., Springer, New York, NY., 2009.
- Hwang, B. J., Ehn, J. K., Barber, D. G., Galley, R. and Grenfell, T. C.: Investigations of newly formed sea ice in the Cape Bathurst polynya: 2. Microwave emission, *J. Geophys. Res. Oceans*, 112(C5), C05003, doi:10.1029/2006JC003703, 2007.
- Ivanova, N., Pedersen, L. T. and Tonboe, R.: D2.5 Product Validation & Algorithm Selection Report (PVASR), Sea Ice Concentration, SICCI Phase I, ESA., 2013.
- Ivanova, N., Pedersen, L. T., Tonboe, R. T., Kern, S., Heygster, G., Lavergne, T., Sørensen, A., Saldo, R., Dybkjær, G., Brucker, L. and Shokr, M.: Inter-comparison and evaluation of sea ice algorithms: towards further identification of challenges and optimal approach using passive microwave observations, *The Cryosphere*, 9(5), 1797–1817, doi:10.5194/tc-9-1797-2015, 2015.
- Iwamoto, K., Ohshima, K. I. and Tamura, T.: Improved mapping of sea ice production in the Arctic Ocean using AMSR-E thin ice thickness algorithm, *J. Geophys. Res. Oceans*, 119(6), 3574–3594, doi:10.1002/2013JC009749, 2014.
- JCOMM Expert Team on Sea Ice: Sea-Ice Nomenclature: snapshot of the WMO Sea Ice Nomenclature WMO No. 259, World Meteorological Organization, Geneva, Switzerland., 2014.
- Kern, S., Lavergne, T., Notz, D., Pedersen, L. T., Tonboe, R. T., Saldo, R. and Sørensen, A. M.: Satellite passive microwave sea-ice concentration data set intercomparison: closed ice and ship-based observations, *The Cryosphere*, 13(12), 3261–3307, doi:10.5194/tc-13-3261-2019, 2019.
- Kilic, L., Tonboe, R. T., Prigent, C. and Heygster, G.: Estimating the snow depth, the snow–ice interface temperature, and the effective temperature of Arctic sea ice using Advanced Microwave Scanning Radiometer 2 and ice mass balance buoy data, *The Cryosphere*, 13(4), 1283–1296, doi:10.5194/tc-13-1283-2019, 2019.
- Kimura, N. and Wakatsuchi, M.: Processes controlling the advance and retreat of sea ice in the Sea of Okhotsk, *J. Geophys. Res.*, 104(C5), 11137–11150, doi:10.1029/1999JC900004, 1999.
- Lavelle, J., Tonboe, R., Tian, T., Pfeiffer, R.-H. and Howe, E.: Product User Manual for the OSI SAF AMSR-2 Global Sea Ice Concentration, Product OSI-408, EUMETSAT OSI SAF., 2016.
- Lavergne, T., Tonboe, R., Lavelle, J. and Eastwood, S.: Algorithm Theoretical Basis Document for the OSI SAF Global Sea Ice Concentration Climate Data Record, OSI-450, OSI-430-b, EUMETSAT OSI SAF., 2019a.
- Lavergne, T., Sørensen, A. M., Kern, S., Tonboe, R., Notz, D., Aaboe, S., Bell, L., Dybkjær, G., Eastwood, S., Gabarro, C., Heygster, G., Killie, M. A., Brandt Kreiner, M., Lavelle, J., Saldo, R., Sandven, S. and Pedersen, L. T.: Version 2 of the EUMETSAT OSI SAF and ESA CCI sea-ice concentration climate data records, *The Cryosphere*, 13(1), 49–78, doi:10.5194/tc-13-49-2019, 2019b.
- Maeda, T., Taniguchi, Y. and Imaoka, K.: GCOM-W1 AMSR2 Level 1R product: dataset of brightness temperature modified using the antenna pattern matching technique, *IEEE Trans. Geosci. Remote Sens.*, 54(2), 770–782, doi:10.1109/TGRS.2015.2465170, 2016.
- Mäkynen, M. and Karvonen, J.: MODIS sea ice thickness and open water–sea ice charts over the Barents and Kara Seas for development and validation of sea ice products from microwave sensor data, *Remote Sens.*, 9(12), 1324, doi:10.3390/rs9121324, 2017.
- Mäkynen, M. and Similä, M.: Thin ice detection in the Barents and Kara Seas with AMSR-E and SSMIS radiometer data, *IEEE Trans. Geosci. Remote Sens.*, 53(9), 5036–5053, doi:10.1109/TGRS.2015.2416393, 2015.
- Mäkynen, M. and Similä, M.: Thin Ice Detection in the Barents and Kara Seas Using AMSR2 High-Frequency Radiometer Data, *IEEE Trans. Geosci. Remote Sens.*, 57(10), 7418–7437, doi:10.1109/TGRS.2019.2913283, 2019.

- Mäkynen, M., Cheng, B. and Similä, M.: On the accuracy of thin-ice thickness retrieval using MODIS thermal imagery over Arctic first-year ice, *Ann. Glaciol.*, 54(62), 87–96, doi:10.3189/2013AoG62A166, 2013.
- Mathew, N., Heygster, G. and Melsheimer, C.: Surface Emissivity of the Arctic Sea Ice at AMSR-E Frequencies, *IEEE Trans. Geosci. Remote Sens.*, 47(12), 4115–4124, doi:10.1109/TGRS.2009.2023667, 2009.
- Mätzler, C., Ramseier, R. and Svendsen, E.: Polarization effects in seaice signatures, *IEEE J. Oceanic Eng.*, 9(5), 333–338, doi:10.1109/JOE.1984.1145646, 1984.
- Miao, J., Johnsen, K.-P., Kern, S., Heygster, G. and Kunzi, K.: Signature of clouds over Antarctic sea ice detected by the Special Sensor Microwave/Imager, *IEEE Trans. Geosci. Remote Sens.*, 38(5), 2333–2344, doi:10.1109/36.868890, 2000.
- Nakata, K., Ohshima, K. I. and Nihashi, S.: Estimation of thin-ice thickness and discrimination of ice type From AMSR-E passive microwave data, *IEEE Trans. Geosci. Remote Sens.*, 57(1), 263–276, doi:10.1109/TGRS.2018.2853590, 2019.
- Nihashi, S., Ohshima, K. I., Tamura, T., Fukamachi, Y. and Saitoh, S.: Thickness and production of sea ice in the Okhotsk Sea coastal polynyas from AMSR-E, *J. Geophys. Res. Oceans*, 114(C10), C10025, doi:10.1029/2008JC005222, 2009.
- Ohshima, K. I., Nihashi, S. and Iwamoto, K.: Global view of sea-ice production in polynyas and its linkage to dense/bottom water formation, *Geosci. Lett.*, 3(1), 13, doi:10.1186/s40562-016-0045-4, 2016.
- Shokr, M. and Kaleschke, L.: Impact of surface conditions on thin sea ice concentration estimate from passive microwave observations, *Remote Sens. Environ.*, 121, 36–50, doi:10.1016/j.rse.2012.01.005, 2012.
- Shokr, M., Asmus, K. and Agnew, T. A.: Microwave emission observations from artificial thin sea ice: the ice-tank experiment, *IEEE Trans. Geosci. Remote Sens.*, 47(1), 325–338, doi:10.1109/TGRS.2008.2005585, 2009.
- Smith, D. M.: Extraction of winter total sea-ice concentration in the Greenland and Barents Seas from SSM/I data, *Int. J. Remote Sens.*, 17(13), 2625–2646, doi:10.1080/01431169608949096, 1996.
- Smith, D. M. and Barrett, E. C.: Satellite mapping and monitoring of sea ice, University of Bristol, Bristol, UK., 1993.
- Svendsen, E., Kloster, K., Farrelly, B., Johannessen, O. M., Johannessen, J. A., Campbell, W. J., Gloersen, P., Cavalieri, D. and Mätzler, C.: Norwegian Remote Sensing Experiment: Evaluation of the Nimbus 7 scanning multichannel microwave radiometer for sea ice research, *J. Geophys. Res.*, 88(C5), 2781, doi:10.1029/JC088iC05p02781, 1983.
- Tian, T., Tonboe, R. and Lavelle, J.: The EUMETSAT OSI SAF AMSR-2 Sea Ice Concentration Algorithm, Algorithm Theoretical Basis Document, Product OSI 408, EUMETSAT OSI SAF., 2015.
- Tonboe, R. and Pedersen, L. T.: D2.1 Sea Ice Concentration Algorithm Theoretical Basis Document (ATBD), SICCI Phase II, ESA., 2017.
- Tonboe, R. T., Schyberg, H., Nielsen, E., Rune Larsen, K. and Tveter, F. T.: The EUMETSAT OSI SAF near 50 GHz sea ice emissivity model, *Tellus A*, 65(1), 18380, doi:10.3402/tellusa.v65i0.18380, 2013.
- Tonboe, R. T., Eastwood, S., Lavergne, T., Sørensen, A. M., Rathmann, N., Dybkjær, G., Pedersen, L. T., Høyer, J. L. and Kern, S.: The EUMETSAT sea ice concentration climate data record, *The Cryosphere*, 10(5), 2275–2290, doi:10.5194/tc-10-2275-2016, 2016.
- Wentz, F. J.: A well-calibrated ocean algorithm for Special Sensor Microwave / Imager, *J. Geophys. Res. Oceans*, 102(C4), 8703–8718, doi:10.1029/96JC01751, 1997.
- Wentz, F. J. and Meissner, T.: AMSR ocean algorithm, Algorithm Theoretical Basis Document (ATBD), Remote Sensing Systems, Santa Rosa, California., 2000.

Yu, Y. and Rothrock, D. A.: Thin ice thickness from satellite thermal imagery, J. Geophys. Res. Oceans, 101(C11), 25753–25766, doi:10.1029/96JC02242, 1996.

A Appendix – Matlab Programs

In the following is the list and short descriptions of the Matlab programs coded during work. The programs are too lengthy to be shown in here. In addition, also the Matlab datafiles are available.

OSI-450 SIC with 25 or 50 km pixel size

osi450_tiepoint_data1.m; osi450_tiepoint_data1_50.m

Collect ow and sea ice TB data for the determination of the Bow and Bci algorithms in OSI-450. NASA Team SIC for the ice line data collection. Original TB data as input, no atm correction.

osi450_tb_atmcor.m

Atmospheric correction of the AMSR2 TB data or the OSI-450 SIC algorithm. Sea ice surface temperature is the same as air temperature. Same T_a (and also T_s and T_{eff}) in TBref and TBnwp as in OSI SAF. Fixed OSI SAF emissivities in the TB atmospheric correction.

osi450_tiepoint_data2.m; osi450_tiepoint_data2_50.m

Collect ow and sea ice TB data for the determination of the Bow and Bci algorithms for the 2nd time. Location of the pixels determined previously with the NT SIC for original TB data. Atm corrected TB data as input.

osi450_sic.m; osi450_sic50.m

SIC estimation following the OSI450 product: SIC is combination of Bci and Bow SIC estimates. Atm corrected TB data. Two Bci versions: default Bci and one with the Bci SIC bias correction based on the curved ice line. sic1=default BCI, sic2=Bci with the curved ice line correction.

NASA Team SIC algorithm

nasateam_sic.m

NASA Team SIC algorithm. Arctic tie points, winter time SICCI Phase 2: D2.1 Sea Ice Concentration Algorithm Theoretical Basis Document (ATBD), Sep 2017 Tables 5-X: Tie-points for Northern Hemisphere used with nonatmospheric corrected TBs. Same as in Ivanova et al. 2015.

OSI-450 SIC with the new atmospheric correction, 25 km pixel size

emissivity_proxy_data.m

Collect data for sea ice emissivity studies. Apparent emissivity as $e_{app}=TB/T_{eff}$. Collect e_{app} data for MYI and FYI. Their concentrations in a pixel with NT; ice type SIC must be larger than a threshold. TBs and T_a from pixels are also collected.

emissivity_fyi_myi.m

Analysis of the collected FYI and MYI e_{app} data. Finding temporal e_{app} tie points.

tiepoint_data1.m

Collect ow and sea ice TB data for the determination of the Bow and Bci algorithms. Location of the pixels determined previously with the NT SIC for original TB data. Original TB data as input. Thin ice detection; samples rejected.

tb_atmcor_new.m

Atmospheric correction of the AMSR2 TB data with new method for sea ice. Sea ice surface temperature is the same as air temperature. Daily FYI and MYI emissivities in the TB atmospheric correction. FYI and MYI T_{eff} 's from Mathew et al. (2009). Fixed e_{aref} 's, T_{effref} 's and T_{aref} 's from

Dec-April data. For pixel-based esi's and Teff's FYI, MYI and total SICs with the NASA Team algorithm. Total OSI-450 SIC for the atm correction.

tiepoint_data2.m

Collect ow and sea ice TB data for the determination of the Bow and Bci algorithms. Location of the pixels determined previously with the NT SIC for original TB data. New atm corrected TB data as input.

sic_new.m

SIC estimation following the OSI450 product: SIC is combination of Bci and Bow SIC estimates. TB data has atmospheric correction with the new method. Two Bci versions: default Bci and one with the Bci SIC bias correction based on the curved ice line. sic1=default BCI, sic2=Bci with the curved ice line correction

OSI-450 SIC with the new atmospheric correction, 50 km pixel size

emissivity_proxy_data50.m; emissivity_fyi_myi.m; tiepoint_data1_50.m; tb50_atmcor_new.m; tiepoint_data2_50.m; sic_new50.m

Determination of dynamic tie points in all SIC algorithms

osi450_tiepoints.m

Determining daily dynamic Bow and Bci algorithms: tie points and optimal plane rotation angles using the collected TB data with the NASA Team SIC and open water areas outside maximum climatological SIE. Curved ice line bias correction for Bci. The ow sample does not enter a PCA, but is simply averaged to find the mean ow point, that is the typical signature of open water conditions. This program is applied to all atm corrected TB tie point datasets.

Programs for comparison between the default atmospheric correction and the new one, and the default and new SIC datasets

atmcor_comp.m; atmcor_comp50.m

Comparison between the basic OSI SAF and new TB atmospheric corrections. Conducted over three test areas. Results for Section 7 in the work report.

osi450_comparison.m

Comparison of different OSI-450 SIC algorithms. Results for Sections 8.1 and 8.2.

sic_chart_comp.m; sic_chart_comp_50.m

Comparison between the basic OSI SAF SIC charts and new SIC charts with new TB atmospheric correction. Section 9 in the report.

test_3d.m

Testing different TB data combinations for the 3D SIC algorithm tuning. Results for Section 8.3.

test_3d_sic.m

SIC estimation following the OSI450 product: SIC is combination of Bci and Bow SIC estimates. No curved ice line correction. Test different three channels combinations. Two Bci versions: default Bci and one with the Bci SIC bias correction based on the curved ice line. sic1=default BCI, sic2=Bci with the curved ice line correction.

test_3d_results.m

Results for Section 8.3.